

Theory of Molecular-scale Transport in Graphene Nanojunctions



Qingqing Wu

This dissertation is submitted for the degree of Doctor of
Philosophy

June 2018

Department of Physics, Lancaster University, UK

STAY HUNGRY. STAY FOOLISH.

BE YOURSELF.

Declaration

This thesis has not been submitted in support of an application for another degree at this or any other university. This thesis documents work carried out between October 2015 and March 2018 at Lancaster University, UK, under the supervision of Prof. Colin J. Lambert and funded by a Faculty of Science and Technology Scholarship.

Qingqing Wu

May 15, 2018

Abstract

A molecular junction consists of a single molecule or self-assembled monolayer (SAM) placed between two electrodes. It has varieties of functionalities due to quantum interference in nanoscale. Although there exist issues, advantages could still appeal to scientists who wish to investigate transport properties in many aspects such as electronics, thermoelectronics, spintronics, and optotronics.

Recent studies of single-molecule thermoelectricity have identified families of high-performance molecules. However, controlled scalability might be used to boost electrical and thermoelectric performance over the current single-junction paradigm. In order to translate this discovery into practical thin-film energy-harvesting devices, there is a need for an understanding of the fundamental issues arising when such junctions are placed in parallel. As a first step in this direction, we investigate here the properties of two C_{60} molecules placed in parallel and sandwiched between top and bottom graphene electrodes. It is found that increasing the number of parallel junctions from one to two can cause the electrical conductance to increase by more than a factor of 2 and furthermore, the Seebeck coefficient is sensitive to the number of parallel molecules sandwiched between the electrodes, whereas classically it should be unchanged. This non-classical behaviour of the electrical conductance and Seebeck coefficient are due to inter-junction quantum interference, mediated by the electrodes, which leads to an enhanced response in these vertical molecular devices.

Except the study of thermoelectricity, on the other hand, stable, single-molecule switches with high on-off ratios are an essential component for future molecular-scale circuitry. Unfortunately, devices using gold electrodes are neither complementary metal-oxide-semiconductor (CMOS) compatible nor stable at room temperature. To overcome these limitations, several groups are developing electroburnt graphene electrodes for single molecule electronics. Here, in anticipation of these developments, we examine how the electrical switching properties of a series of porphyrin molecules with pendant dipoles can be tuned by systematically increasing the number of spacer units between the porphyrin core and graphene electrodes. The porphyrin is sandwiched between a graphene source and drain and gated by a third electrode. The associated rotation of porphyrin referred to graphene plane leads to the breaking of conjugation and a decrease in electrical conductances. As the number of spacers is increased, the conductance ratio can increase from 100 with one spacer to 200 with four spacers, and further enhanced by decreasing the temperature, reaching approximately 2200 at 100K. This design for a molecular switch using graphene electrodes could be extended to other aromatic systems.

As mentioned in the design of C_{60} -based thermoelectric vertical junction with graphene layers as electrodes and porphyrin-based switch in graphene nanogap, graphene provides a two-dimensional platform for contacting individual molecules, which enables transport spectroscopy of molecular orbital, spin, and vibrational states. Next, we report single-electron tunnelling through a molecule that has been anchored to two graphene leads. It is found that quantum interference within the graphene leads gives rise to an energy-dependent

transmission and fluctuations in the sequential tunnelling. The lead states are electrostatically tuned by a global back-gate due to the weak screening effect compared to the metal electrodes, resulting in a distinct pattern of varying intensity in the measured conductance maps. This pattern could potentially obscure transport features that are intrinsic to the molecule under investigation. Finally, using ensemble averaged magneto-conductance measurements, lead and molecule states are disentangled, enabling spectroscopic investigation of the single molecule.

As the above describes, there are varieties of research on the charge transport properties of molecular devices. It is noticed that noise exists in all electronic devices, and the investigation on noise could help us understand more fundamental information of the device, i.e. the imperfections and configurational changes in the system, the correlation of the transmission conduction channels or even exploit the noise characteristics for biosensing. In electroburnt graphene nanogaps, our collaborators observe that $1/f$ noise and random telegraph noise at room temperature and 77K respectively. Here, I employ a simple one-dimensional tight binding model to gauge the effect of two-level fluctuations in the electrostatic environment in the tunnel junctions. Two types of models are investigated. Model I describes the case that the environmental traps drive the tunnel barrier locally and differently. Model II is the case that the collective effect of all the environmental traps drives the tunnel barrier synchronously. It is concluded that the 77 K data is best described by a single environmental fluctuator influencing the transmission through the tunnel barrier. This may either occur via a local perturbation of the barrier potential, or via an overall modulation of the barrier

height. A $1/f$ signal emerges as more fluctuators with different lifetime τ are added to the environment, corresponding to the thermal activation of multiple random telegraph noises (RTNs) at room temperature.

Acknowledgements

I would like to thank my supervisor, Professor Colin J. Lambert who is always energetic and has an inclusive and encouraging heart. I am so grateful for him to provide me the chance to join his group in October, 2015. The lectures and tutorials he delivered provide me a deep understanding of molecular electronics which would be really helpful for my future study and research. The discussions with him on projects provide me a broader horizon to the physics.

Then I would thank my husband and colleague, Songjun Hou who gives me the largest support for everything. I am really grateful for his patience, tolerance. I really enjoy discussing research with him. I would like to thank Dr. Hatef Sadeghi who gave me a lot of help on my work who is doing brilliant research. I would like to thank my collaborators Prof. Jaime Ferrer and Dr. Victor M. García-Suárez for the discussion from Oviedo University on our joint paper. I also would like to thank the experimental collaborators from Oxford University i.e. Prof. G. Andrew D. Briggs, Prof. Harry L. Anderson, Dr. Jan A. Mol, Dr. Pascal Gehring, Pawel Puczkarski, Dr. Bart Limburg. I also want to thank my collaborators from Prof. Wenjing Hong's group in Xiamen University i.e. Dr. Yangyang, Jiuchan Pi, ZhangDan, Zhibing Chen. I am also so grateful for discussions with Dr. Steven Bailey and Iain Grace, and help from Ali, Sara, Marjan, Michael, Norah and many others in my group. I would like to thank the Faculty of Science and Technology for the studentship which funds my PhD study in Lancaster University. And finally, I would thank my beloved parents who support me all the way to pursue my dream. I am really grateful for their love and understanding.

List of publications

- [1] “Thermoelectricity in vertical graphene-C60-graphene architectures,” Q. Wu, H. Sadeghi, V. M. García-Suárez, J. Ferrer, and C. J. Lambert, *Sci. Rep.* 7, 1180, 2017.
- [2] “A single-molecule porphyrin-based switch for graphene nano-gaps,” Q. Wu, S. Hou, H. Sadeghi, C. J. Lambert, *Nanoscale*, 10, 6524, 2018.
- [3] “Distinguishing Lead and Molecule States in Graphene-Based Single-Electron Transistors,” P. Gehring, J. Sowa, J. K. Cremers, Q. Wu, H. Sadeghi, Y. Sheng, J. H. Warner, C. J. Lambert, A. D. Briggs, *J. A. Mol, ACS Nano*, vol. 11, no. 6, pp. 5325–5331, 2017.
- [4] “MoS₂ nano flakes with self-adaptive contacts for efficient thermoelectric energy harvesting,” Q. Wu, H. Sadeghi, C. J. Lambert, *Nanoscale*, 10, 7575-7580, 2018.
- [5] “Quantum transport through vertical interfaces of single molecular van der Waals heterojunctions,” J. Pi⁺, Q. Wu⁺, J. Liu, J. Zheng, H. Sadeghi, J. Wei, S. Zhao, R. Li, S. Hou, Y. Yang, J. Shi, Z. Chen, Z. Xiao, C. Lambert, W. Hong, Submitted. (2018)
- [6] “Charge Transport through Single-Fullerene Junctions using Graphene Nanoelectrodes: Towards Full-Carbon Electronic”, Z. Dan⁺, Z. Tan⁺, H. Tian⁺, Q. Wu⁺, J. Pi, S. Hou, H. Sadeghi, Z. Tang, Y. Yang, Y. Tan, Z. Xiao, Z. Chen, J. Shi, C. Lambert, S. Xie, W. Hong, submitted. (2018)

[7] “Low frequency noise in graphene tunnel junction,” P. Puczkarski, Q. Wu, H. Sadeghi, S. Hou, A. Karimi, Y. Sheng, J. H. Warner, C. J. Lambert, A. D. Briggs, J. A. Mol. Submitted to ACS Nano (2018)

Contents

1 INTRODUCTION	1
1.1 Molecular electronics	1
1.2 Thesis outline	5
2 DENSITY FUNCTIONAL THEORY AND TRANSPORT THEORY	8
2.1 Density functional theory	8
2.1.1 <i>Many-body system</i>	9
2.1.2 <i>Hohenberg-Kohn theorems</i>	10
2.1.3 <i>Kohn-Sham formulation</i>	12
2.2 Transport theory.....	15
2.2.1 <i>Landauer formula</i>	16
2.2.2 <i>Bond current and Scattering matrix</i>	18
2.2.3 <i>Green's function</i>	24
2.2.4 <i>Transmission function</i>	27
2.2.5 <i>Breit-Wigner resonance</i>	34
2.3 Fundamental properties	37
2.3.1 <i>Thermoelectricity</i>	37
2.3.2 <i>Coulomb blockade</i>	46
2.3.3 <i>Applying a vector field</i>	48
2.3.4 <i>Noise spectroscopy</i>	49
3 THERMOELECTRICITY IN VERTICAL GRAPHENE-C₆₀-GRAPHENE ARCHITECTURES.....	51
3.1 Introduction.....	51

3.2 Results and discussion.....	54
3.3 Conclusion	65
4 A SINGLE-MOLECULE PORPHYRIN-BASED SWITCH FOR GRAPHENE NANOGAPS	66
4.1 Introduction.....	66
4.2 Results and discussion.....	69
4.3 Conclusions	85
5 DISTINGUISHING LEAD AND MOLECULE STATES	87
5.1 Introduction.....	87
5.2 Results and discussion.....	89
<i>5.2.1 The observation and simulation of Coulomb blockade</i>	<i>89</i>
<i>5.2.2 Applying magnetic field to distinguish the DOS in leads and molecule</i>	<i>107</i>
5.3 Conclusion	111
6 LOW FREQUENCY NOISE IN GRAPHENE TUNNEL JUNCTIONS.....	113
6.1 Introduction.....	113
6.2 Results and discussion.....	115
6.3 Conclusions	135
7 CONCLUSIONS.....	138
8 APPENDICES.....	141

1 Introduction

1.1 Molecular electronics

The research field of molecular electronics aims to investigate the electronic and thermal transport properties of the molecular circuits which consist of a single molecule or self-assembled molecular monolayers (SAMs) and nanoscale electrodes made from metals, such as [1][2] (Au, Ag, Cu, Fe, Co, Ni), semiconductors such as Si[3], or carbon (carbon nanotube[4][5], graphene monolayer[6][7][8] or graphite). To describe the flow of electricity and heat through such structures combined knowledge from traditional disciplines like physics, chemistry, material science, electrical engineering is needed [9]. Molecular electronics has become widely investigated both theoretically and experimentally, because of the following advantages compared to traditional complementary metal oxide semiconductor (CMOS) technology. The first advantage is its nanoscale size which is appropriate to improve circuit-integration and lead to energy-saving and faster performance. Second, it provides a variety of

novelty functionalities due to quantum interference, i.e. switching [10][11][12][13][14][15][16], negative differential resistance[17][18][19], thermoelectronics[20][21][22][7][23], Coulomb blockades[24][25][26][6], Kondo resonances[27], spintronics[28][29], and optoelectronics[30][31][2]. Third, intermolecular interactions could also be utilised in nanoscale self-assembly technology, potentially resulting in low-cost manufacturing. All the above show that molecular electronics has the potential to complement conventional silicon-based electronics.

The origin of molecular electronics dates back 40-50 years. In the 1970s, Kuhn, Mann[32], polymeropoulos, and Sagiv [33][34] first developed effective techniques of self-assembly monolayers used as tunnelling barriers to prepare metal/insulator/metal junctions using organic molecules. Various techniques have been introduced for single-molecule studies in the following years based on metal electrode (scanning tunnelling microscopy (STM)[35] (see Fig. 1.1) and atomic force microscopy (AFM), mechanically controllable break junction[36], electro-migration breakdown[37], electrochemical depositions[38]), single-walled carbon nanotube (SWNT) electrode fabricated by electrical breakdown[39] or lithography-defined oxidative cutting [5]and graphene or graphite based nanoelectrodes (feedback-controlled electrburning[26][25][6] (see Fig. 1.2), dash-line lithography[40]). The figures below illustrate two of these approaches.

1. Mechanically controlled break junction(MCBJ)

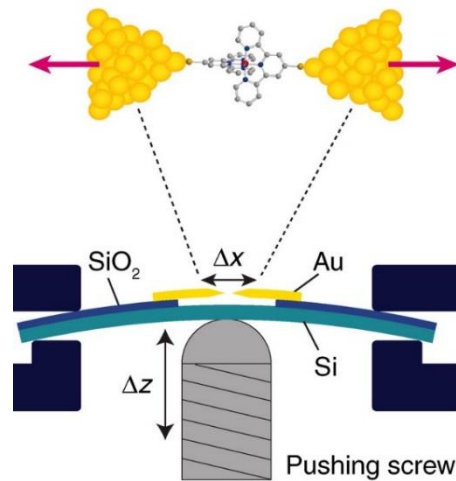


Fig. 1.1 Schematic of Mechanically controllable break junction. The panel above with two red opposite arrows shows the artistic view on the atomically sharp electrodes (formed after the break of the wire) with single molecule between. The panel below shows the relative displacement Δx , corresponding to the displacement Δz of pushing screw[41].

2. Feedback-controlled electroburning

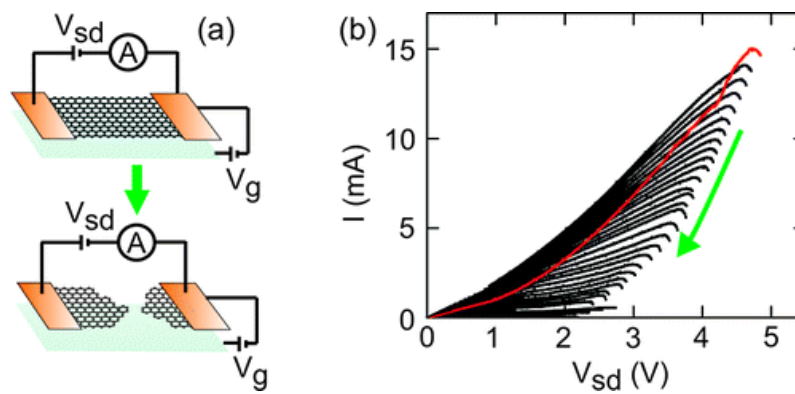


Fig. 1.2 (a) Schematic of the feedback-controlled electroburning process, before (the top) and after (the bottom) the formation of nanometre sized gaps in few-layer graphite flakes. (b) Current-voltage traces of the evolution (green arrow) of the feedback-controlled electroburning[26].

In the process shown in Fig. 1.2, slowly increase applied voltage while monitoring changes in current flowing through the constriction. Upon further increase in applied voltage, a decrease in current is observed, which corresponds to the narrowing of the constriction due to Joule heating. At this point a feedback loop quickly brings back applied voltage to 0 V. The entire cycle is repeated multiple times with conductance decreasing after each iteration shown in (b). At the end of each cycle the resistance value is checked, and the electroburning procedure is terminated upon reaching the threshold value of junction resistance, which means the formation of tunneling junction. The edges of the electroburnt graphene nanogap in ambient is estimated to be terminated with -H, -OH, -COOH, etc. The length of the gap could be 1~2nm.

In parallel with the above experimental developments, simulations based on first principles emerged as an indispensable theoretical tool allowing researchers to construct a quantitative picture of transport mechanisms and form predictions to guide further experimental studies. Combining density functional theory and Green's function method, the transport properties of molecular devices based on scattering theory are investigated theoretically.

The development of these experimental techniques and theoretical methods led to an explosion in the use of individual molecules or SAMs in molecular electronics. Although the development of molecular electronics has been significantly boosted and promoted, there are still some issues to solve and aspects to investigate, i.e., robustness, the effect of solvents, the noise in the electric system. So it is of significance and necessary to do more fundamental research on molecular

electronics before the final commercial applications can be realised at larger scales.

1.2 Thesis outline

This thesis consists of 6 chapters: An introduction to molecular electronics; an introduction to transport theory, three results chapters, a conclusion and suggestions for future work.

In chapter 1, a simple definition for molecular electronics is provided and the development of molecular electronics is summarized. In chapter 2, the development of density functional theory (DFT) is briefly discussed and the transport theory based on scattering theory and equilibrium Green's function method is presented. In addition, some fundamental scientific phenomena are briefly introduced in order to have a good understanding of the work shown in the following chapters.

Chapter 3 presents the thermoelectric properties of a vertical graphene/ C_{60} /graphene architecture. It is found that quantum interference between two C_{60} s placed in parallel enhances the conductance by more than two times that of the monomer C_{60} . Importantly, the Seebeck coefficient increases which is not expected classically. These results are considered as the starting point to understand the properties of SAMs sandwiched between two electrodes.

Chapter 4 shows a design of a single-molecule porphyrin-based switch for graphene nanogaps. Based on the development of feedback controlled electroburning, graphene nanogaps are utilised to propose a conjugation-dependent switch. It is found that the system has an on-off ratio ranging from 100 to 200 when increasing the spacers between the porphyrin and graphene. The switching ratio is further enhanced by decreasing the temperature, reaching approximate 2200 at 100K.

Chapter 5 is a collaboration with experimental colleagues. Observed conductance fluctuations in molecular junctions formed from electro-burnt graphene nanogaps are modeled. In the simulation, a tight binding chain is first introduced to prove that the fluctuations are due to the lead states and are not an intrinsic feature of the molecule. Stripes in Coulomb diamonds happen when the molecular level matches a density of states peak in a lead and their slope could be tuned by the coupling between the lead and backgate. Furthermore, the magnetic field is introduced to distinguish the two kinds of states through ensemble average. Correspondingly, the ring is introduced into the tight binding model to allow a flux to be applied. In agreement with experiments, this confirms that fluctuations can be reduced by application of a magnetic field.

Chapter 6 presents a study of $1/f$ noise and random telegraph noise, which are observed in graphene nanogap at room temperature and 77K respectively. I investigate two types of tight binding models to obtain further insight into the noise characteristics. I conclude that 77 K experimental data is best described by a single environmental fluctuator influencing the transmission through the tunnel

barrier. This may either occur via a local perturbation of the barrier potential, or via an overall modulation of the barrier height. A $1/f$ signal emerges as more fluctuators sampled in a large dwell time range are activated by the thermal energy at room temperature.

The final chapter, I present the conclusions of my thesis and suggestions for future work.

2 Density functional theory and transport theory

Simulations based on density functional theory (DFT) have emerged as an indispensable theoretical tool, which allows researchers to construct a quantitative picture of transport mechanisms and form predictions to guide further experimental studies. DFT and Green's function methods provide a powerful electron transport theory of non-periodic and open molecular devices based on scattering theory. In this chapter, section 2.1 presents the basic principles and methodology for DFT. Section 2.2 illustrates the generic features of this transport theory by examining some simple tight binding models.

2.1 Density functional theory

Electronic structure of small and simple systems (i.e. H_2 , H_e molecules) could be analysed through the wavefunctions solved by Schrödinger equation. However, when the system is a large organic molecule or condensed matter system, Schrödinger's wave equation becomes too complicated to solve, due to the large

number of interacting atoms. An alternative method to the analysis of electronic structure in 3-dimensional system is density functional theory (DFT) which chooses the system's charge density $n(r)$ as a basic parameter instead of the many-body wavefunctions. The following section simply illustrates the main basic theory of DFT. It starts with the Schrödinger equation of a many-body system in real three-dimensional space which is too complicated to solve (section 2.1.1) due to large numbers of variables. Then section 2.1.2, describes the Hohenberg-Kohn formulation, which demonstrates that the ground-state charge density $n(r)$ implicitly determines all the properties of the system derivable from the Hamiltonian. In addition, the Hohenberg-Kohn variational principle of total energy functional is combined with Hartree's self-consistent single-particle equations by Kohn and Sham (section 2.1.3) which has become a powerful and reliable approach to describing ground state properties of a quantum system.

2.1.1 Many-body system

The Hamiltonian of the many-body system with electrons and nuclei is shown below,[42]

$$\hat{H} = -\frac{\hbar^2}{2m_i} \sum_i \nabla_i^2 - \sum_{i,I} \frac{Z_I e^2}{|r_i - R_I|} + \frac{1}{2} \sum_{i \neq j} \frac{e^2}{|r_i - r_j|} - \frac{\hbar^2}{2M_I} \sum_I \nabla_I^2 + \frac{1}{2} \sum_{I \neq J} \frac{Z_I Z_J e^2}{|R_I - R_J|} \quad 2.1$$

Where the lowercase subscripts i, j, r_i, r_j denote the quantities of electrons while the upper cases I, J, R_I, R_J represent the counterparts of nuclei. In terms of the

right part of the expression, the operators correspond to the kinetic energy, the interactions between nuclei and electrons, the electron-electron Coulomb interactions, the kinetic energy of nuclei and nucleus-nucleus coulomb interactions from the first term to the final one. Due to the large nuclear masses, the nuclear kinetic energy could be omitted, to yield the Born-Oppenheimer or adiabatic approximation[43]. The Born-Oppenheimer approximation is the assumption that the motion of atomic nuclei and electrons in a system can be separated due to the huge difference of the masses[42]. This allows the wave function of the system to be broken to electronic and nuclear parts. The final term is the classical interactions of nuclei, which makes no germane contribution to the description for electronic structures. Then Eq. 2.1 goes to Schrödinger equation for the many-electron wave function Ψ .

$$\left\{ -\frac{\hbar^2}{2m_i} \sum_i \nabla_i^2 - \sum_{i,l} V_{ext}(r_i) + \frac{1}{2} \sum_{i \neq j} \frac{e^2}{|r_i - r_j|} \right\} \Psi_n = E_n \Psi_n \quad 2.2$$

Where $V_{ext}(r_i)$ includes the effect of nuclei and the external electric/magnetic field on electrons.

2.1.2 Hohenberg-Kohn theorems

As for the electronic structure of large molecules and condensed matter systems, Schrödinger equation for these many-electron systems encounter an ‘exponential wall’ in terms of the very large number of parameters in three-dimensional real space [44]. Therefore the electron density distribution $n(r)$ is adopted in density

functional theory (DFT). The starting point is the Hohenberg-Kohn formulation which starts from the following total Hamiltonian. In principle it is an exact theory of many-electron system[42].

$$\hat{H} = -\frac{\hbar^2}{2m_i} \sum_i \nabla_i^2 - \sum_i V_{ext}(r_i) + \frac{1}{2} \sum_{i \neq j} \frac{e^2}{|r_i - r_j|} \quad 2.3$$

Where $V_{ext}(r)$ represents the external potential including the part due to nuclei-electron interaction. The total energy functional is written as follows,

$$E_{HK}[n] = F_{HK}[n] + \int dr V_{ext}(r)n(r) \quad 2.4$$

where $F_{HK}[n] = T[n] + E_{int}[n]$ includes all internal energies, kinetic and potential of the interacting electron system.

Two basic lemmas provided by the HK theorem are presented as follows. [42][44]

Lemma 1 shows the ground-state density $n(r)$ corresponds to the only one external potential $V_{ext}(r)$. That is, there is no existence of the second external potential $V_{ext2}(r) \neq V_{ext1}(r) + constant$ which gives rise to the same ground-state density distribution with that of external potential $V_{ext1}(r)$.

Lemma 2: Hohenberg-Kohn variational principle

For any external potential $V_{ext}(r)$, the global minimum of the total energy functional (Eq. 2.4) is the exact ground-state energy and the corresponding density $n(r)$ minimizing the functional (Eq. 2.4) is the exact ground-state density.

2.1.3 Kohn-Sham formulation

It is proposed that using independent-particle equations for non-interacting electrons system to help to solve the original many-body problem by Kohn and Sham in 1965. As a self-consistent method, the Kohn-Sham approach assumes that the ground state density of the original interacting-electron system is equal to that of the chosen auxiliary non-interacting system where the many-body terms are included into an exchange-correlation functional of the density. The following shows the origin of Kohn-Sham equations, the ground-state energy and the corresponding ground-state electron density.

Based on Hohenberg-Kohn functional variational principle, the expression for the ground-state energy functional of the interacting-electron real physical system is presented,[44]

$$E_V[n(r)] = \int V_{ext}(r)n(r)dr + T[n(r)] \quad 2.5$$

$$+ \frac{1}{2} \int drdr' \frac{n(r)n(r')}{|r - r'|}$$

Now rewriting Eq. 2.5,

$$E_V[n(r)] = \int V_{ext}(r)n(r)dr + T_s[n(r)] \quad 2.6$$

$$+ \frac{1}{2} \int drdr' \frac{n(r)n(r')}{|r - r'|} + E_{xc}[n(r)] \geq E$$

This variational expression is for an auxiliary non-interacting-electron system which has the same ground-state energy and density $n(r)$ as the interacting-electron system. The next step is to apply Euler-Lagrange rules,

$$\delta E_V[n(r)] = \int \delta n(r) \left\{ V_{eff}(r) + \frac{\delta T_s[n(r)]}{\delta n(r)} - \varepsilon \right\} dr = 0 \quad 2.7$$

Here $V_{eff} = V_{ext}(r) + \int dr' \frac{n(r')}{|r-r'|} + V_{xc}(r)$ where $V_{xc} = \frac{\delta E_{xc}[n(r)]}{\delta n(r)}$. Now Eq. 2.7 goes to single-particle equation which gives rise to the same ground-state density $n(r)$ as Eq.2.7.

$$\left(-\frac{\hbar}{2m_e} \nabla^2 + V_{eff} - \varepsilon_m \right) \psi_m^\sigma(r) = 0 \quad 2.8$$

Where $V_{eff} = V_{ext}(r) + \int dr' \frac{n(r')}{|r-r'|} + V_{xc}(r)$ and $V_{xc} = \frac{\delta E_{xc}[n(r)]}{\delta n(r)}$. $N = N^\uparrow + N^\downarrow$ is the number of electrons, the charge density $n(r)$ is given by the sums of squares of the eigenstates $\psi_i^\sigma(r)$ for each spin

$$n(r) = \sum_\sigma n(r, \sigma) = \sum_\sigma \sum_{m=1}^{N^\sigma} |\psi_m^\sigma(r)|^2 \quad 2.9$$

Now equations 2.8, 2.9 is the so-called Kohn-Sham equations.

The ground state energy[44] of the full interacting many-body system is

$$E_{KS} = \sum_m \varepsilon_m - \frac{1}{2} \int dr dr' \frac{n(r)n(r')}{|r-r'|} - \int dr V_{XC}(r)n(r) \quad 2.10$$

$$+ E_{XC}[n(r)]$$

Here $\varepsilon_m, \psi_m^\sigma$ are the eigenvalue and eigenstate of Eq. 2.8. When the last two terms correlated to the exchange and correlation interaction of electrons in real many-body system are not taken into consideration, Eq.2.10 degrades to Hartree's self-consistent single-particle ground-state energy. Exchange-correlation functionals (E_{XC}) in DFT approximations have generated good results where the local density approximation (LDA)[45], generalized gradient approximations (GGA) [46], and hybrid functionals [47] are included. In order to incorporate long-range van der Waals interactions and improve the self-interaction, further progress in deriving more accurate exchange-correlation functionals has led to the development of several available approximations, such as non-local functionals for van-der-Waals interactions [48], or range-separated hybrids [49].

The eigenstates $\psi_m^\sigma(r)$ and eigenvalues ε_m of the Kohn-Sham equations don't have any physical meaning, except for the correlation between $\psi_m^\sigma(r)$ and the true, physical density $n(r)$ shown in Eq. 2.9 and the fact that the ionization energy of this system is equal to the magnitude of the highest occupied eigenvalue (HOMO) referring to the vacuum. [44]. However, DFT is widely accepted in physics and chemistry which provides a relatively accurate approach to the science of quantum systems including large molecules compared to experiment, although discrepancies by orders of magnitude could be observed which originate from the underestimation of HOMO-LUMO gap due to the limitation inherent to DFT and

approximated exchange-correlation functionals[50][51][52]. Except the magnitude discrepancy, DFT could still provide quantitatively accurate trend for the comparison research of series of molecules[53] or the connectivity research[54]. It utilises the charge density which determines implicitly all the electronic properties derivable from the Hamiltonian. Based on the electronic structure DFT provides, transport properties of the functional molecular devices discussed in the following sections.

2.2 Transport theory

As for molecular devices consisting of a single molecule or monolayer connected to two electrodes, understanding their electronic properties is fundamental to the investigation of phenomena such as thermoelectricity[7][23] or functionalities such as molecular-scale switching[16]. Transport is considered to be phase coherent provided $l \leq \lambda$ where l is the length of the device and λ is the electron mean free path or scattering length. In this case, the energy of an electron passing through a device is conserved and the electric current flowing through the nanoscale device could be described by Landauer formula which is presented in section 2.2.1. In the current or conductance calculation, the most significant factor is the transmission function (the derivation is shown in section 2.2.4), which can be computed using scattering theory (section 2.2.2) and Green's functions (section 2.2.3). In what follows, the basic principles and methods are introduced, which allow the transmission function to be calculated. Final section in this chapter presents the useful Breit-Wigner formula to describe the transmission properties,

especially the on-resonance transmission where the lowest order perturbation theory becomes invalid. To illustrate generic features in an accessible manner, all the transmission function formulae are derived based on simple tight binding model system connected to one dimensional electrodes or to electrodes containing several conduction channels.

2.2.1 Landauer formula

In a molecular device, the electrodes are connected to reservoirs which feed electrons of energy E . Landauer formula gives the net current passing from the left electrode L to the right electrode R.

$$I = \frac{2e}{h} \int_{-\infty}^{+\infty} dE T(E) [f_L(E) - f_R(E)] \quad 2.11$$

Where $e = -|e|$ is the electronic charge, h is Plank's constant, $T(E)$ is the transmission spectrum for the electron passing from one lead to the other via the molecule and $f_{L(R)}(E) = \frac{1}{e^{\frac{E-\mu_{L(R)}}{k_B T}} + 1}$ is the Fermi-Dirac distribution function where

$\mu_{L(R)}$ is the chemical potential of the left (right) reservoir and T is the temperature.

If the bias V_b is applied on the left and right reservoirs symmetrically, then $\mu_L = E_F + \frac{eV_b}{2}$ and $\mu_R = E_F - \frac{eV_b}{2}$. Clearly, $I = 0$ when $f_L(E) = f_R(E)$ because only differences in the distributions contribute to the net current.

The following shows two cases in zero temperature or zero bias limits[55].

On one hand, with zero temperature approximation, but finite voltage, the current could be written by

$$I = \frac{2e}{h} \int_{E_F - eV_b/2}^{E_F + eV_b/2} dET(E) \quad 2.12$$

Consequently, the conductance $G = I/V$ is obtained by averaging $T(E)$ over an energy window of width eV centred on the Fermi energy.

On the other hand, if $T(E)$ does not vary significantly over an energy range of order eV , then the Fermi functions can be Taylor expanded at $\mu = E_F$. Continuously, substitute μ_L, μ_R in Eq. 2.15 and Eq. 2.16 respectively and neglect the high order terms if V_b is small enough,

$$f(\mu_L) = f(E_F) + \left. \frac{df}{d\mu} \right|_{\mu=E_F} (\mu_L - E_F) \quad 2.13$$

$$f(\mu_R) = f(E_F) + \left. \frac{df}{d\mu} \right|_{\mu=E_F} (\mu_R - E_F) \quad 2.14$$

Next, we have $f_L - f_R = \left. \frac{df}{d\mu} \right|_{\mu=E_F} (\mu_L - \mu_R) = - \left(\frac{df}{dE} \right)_{\mu=E_F} eV_b$.

The electrical conductance in the zero-voltage, finite temperature limit is,

$$G = \frac{I}{V} = G_0 \int_{-\infty}^{+\infty} dET(E) \left(- \frac{df(E)}{dE} \right)_{\mu=E_F} \quad 2.15$$

Where G_0 is the quantum of conductance, $G_0 = \frac{2e^2}{h}$. Since the quantity $-df(E)/dE$ is a normalised probability distribution of width approximately $k_B T$, the above integral represents a thermal average of the transmission function $T(E)$ over an energy window of width $k_B T$.

Finally, with the combination of the two limits (zero voltage and zero temperature), one obtains

$$G = G_0 T(E_F) \quad 2.16$$

In summary, from the perspective of Landauer formula and the calculation of conductance, transmission function $T(E_F)$ is of central significant. Therefore in what follows, I present derivations of transmission properties of a few model systems.

2.2.2 Bond current and Scattering matrix

This section starts with bond current and then goes to the scattering matrix. From the discussion of these two parts, I present that the current on every site of the one-dimensional chain is equal which further gives rise to the intrinsic characteristic of molecular devices based on scattering theory. That is, the transmission and reflection coefficients from one lead to the other lead are the same with the opposite injecting case.

2.2.2.1 The description of bond current

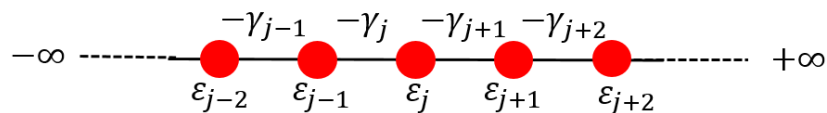


Fig. 2.1 Tight binding model for infinite chain. ε_j represents the on-site energy while γ_j stands for the hopping integral.

The time-independent Schrödinger equations for the system shown in Fig. 2.1 is as follows,

$$\begin{cases} \varepsilon_{j-1}\psi_{j-1} - \gamma_j\psi_j - \gamma_{j-1}\psi_{j-2} = E\psi_{j-1} \\ \varepsilon_j\psi_j - \gamma_{j+1}\psi_{j+1} - \gamma_j\psi_{j-1} = E\psi_j \\ \varepsilon_{j+1}\psi_{j+1} - \gamma_{j+2}\psi_{j+2} - \gamma_{j+1}\psi_j = E\psi_{j+1} \end{cases} \quad 2.17$$

Similarly, the time-dependent Schrödinger equation is

$$\frac{i\hbar\partial\psi_j}{\partial t} = \varepsilon_j\psi_j - \gamma_{j+1}\psi_{j+1} - \gamma_j\psi_{j-1} \quad 2.18$$

Multiplying Eq. 2.18 by ψ_j^* and multiplying the conjugation of Eq. 2.18 by ψ_j leads to the following results,

$$\begin{cases} \psi_j^* \frac{i\hbar\partial\psi_j}{\partial t} = \varepsilon_j\psi_j^*\psi_j - \gamma_{j+1}\psi_j^*\psi_{j+1} - \gamma_j\psi_j^*\psi_{j-1} \\ \psi_j \left(\frac{i\hbar\partial\psi_j}{\partial t} \right)^* = \varepsilon_j\psi_j\psi_j^* - \gamma_{j+1}\psi_j\psi_{j+1}^* - \gamma_j\psi_j\psi_{j-1}^* \end{cases} \quad 2.19$$

Then the following differential equation is obtained based on the above two equations,

$$\begin{aligned} \frac{d\psi_j\psi_j^*}{dt} &= \frac{d|\psi_j|^2}{dt} \\ &= \frac{\gamma_{j+1}(\psi_j\psi_{j+1}^* - \psi_j^*\psi_{j+1}) - \gamma_j(\psi_{j-1}\psi_j^* - \psi_{j-1}^*\psi_j)}{i\hbar} \end{aligned} \quad 2.20$$

As for the infinite chain, we have the following expression.

$$\frac{d|\psi_j|^2}{dt} = \frac{dn}{dt} = I_{j-1 \rightarrow j} - I_{j \rightarrow j+1} \quad 2.21$$

Comparing Eq. 2.20 and Eq. 2.21, yields the following expressions for the bond current from site j to site $j+1$.

$$I_{j \rightarrow j+1} = \frac{2\gamma_{j+1}}{\hbar} \text{Im}(\psi_j^* \psi_{j+1}) \quad 2.22$$

If ψ_j is an eigen state of H , then the bond current has the feature:

$$I_{j-1 \rightarrow j} = I_{j \rightarrow j+1} \quad 2.23$$

This is proved by noting that if

$$|\psi\rangle = A(t)|\phi_n\rangle \quad 2.24$$

Where $H|\phi_n\rangle = E_n|\phi_n\rangle$, then the solution $|\psi\rangle$ for time dependent Schrodinger

equation $\frac{i\hbar\partial|\psi\rangle}{\partial t} = H|\psi\rangle$ is $|\psi\rangle = ce^{-\frac{iE_n t}{\hbar}}|\phi_n\rangle$ is obtained. So we have $\psi_j(t) =$

$ce^{-\frac{iE_n t}{\hbar}}\phi_{n,j}$ and further $\psi_j\psi_j^* = |c|^2\phi_{n,j}\phi_{n,j}^*$ which does not depend on time.

According to formula. 2.21, $I_{j-1 \rightarrow j} - I_{j \rightarrow j+1} = 0$.

An example:

If $\psi_j = Ae^{ikj}$, the bond current is presented,

$$I = \frac{2\gamma}{\hbar} \text{Im}(\psi_j^* \psi_{j+1}) = \frac{2\gamma}{\hbar} A^2 \sin k = VA^2 \quad 2.25$$

Where V is the group velocity.

2.2.2.2 The derivation of the scattering matrix

If an incident current transmission I_{in} in a left lead produces an outgoing current I_t in a right lead, then the transmission coefficient T is defined by

$$T = \frac{I_t}{I_{in}} \quad 2.26$$

To relate T to the scattering matrix, note that the most general solution of the time independent Schrodinger equation for the left lead along with its corresponding current is

$$\psi_j = \frac{A}{\sqrt{V_l}} e^{ik_l j} + \frac{B}{\sqrt{V_l}} e^{-ik_l j} \quad 2.27$$

$$I_l = |A|^2 - |B|^2 \quad 2.28$$

Similarly for the right lead:

$$\psi_j = \frac{C}{\sqrt{V_r}} e^{ik_r j} + \frac{D}{\sqrt{V_r}} e^{-ik_r j} \quad 2.29$$

$$I_r = |C|^2 - |D|^2 \quad 2.30$$

Since bond currents satisfy $I_l = I_r$, there is the relationship below.

$$|A|^2 - |B|^2 = |C|^2 - |D|^2 \quad 2.31$$

Or the total incoming current I_{in} is equal to the total outgoing current I_{out} .

$$|A|^2 + |D|^2 = |B|^2 + |C|^2 \quad 2.32$$

Now imagine there is a matrix S to connect the four parameters as follows,

$$\begin{bmatrix} B \\ C \end{bmatrix} = \begin{bmatrix} S_{11} & S_{12} \\ S_{21} & S_{22} \end{bmatrix} \begin{bmatrix} A \\ D \end{bmatrix} \quad 2.33$$

That is $|out\rangle = S|in\rangle$. And then I could obtain $\langle out| = \langle in|S$. Finally, combine these two formulae to get $\langle out|out\rangle = |B|^2 + |C|^2 = \langle in|S^\dagger S|in\rangle$. Due to $\langle in|in\rangle = |A|^2 + |D|^2$, So S is a unitary matrix. Put in another words, $S^\dagger = S^{-1}$. Now two cases are considered in order to achieve further insight into the transmission properties.

Case one: $A=1; D=0$

The wavefunction for left and right leads:

$$\begin{cases} \psi_{jl} = \frac{e^{ik_{lj}}}{\sqrt{V_l}} + \frac{r}{\sqrt{V_l}} e^{-ik_{lj}} \\ \psi_{jr} = \frac{t}{\sqrt{V_r}} e^{ik_{rj}} \end{cases} \quad 2.34$$

And then, we have

$$\begin{bmatrix} r \\ t \end{bmatrix} = \begin{bmatrix} S_{11} & S_{12} \\ S_{21} & S_{22} \end{bmatrix} \begin{bmatrix} 1 \\ 0 \end{bmatrix} \quad 2.35$$

Finally, there is reflection coefficient $R = I_r/I_{in} = |r|^2 = |S_{11}|^2$, and transmission coefficient $T = I_t/I_{in} = |t|^2 = |S_{21}|^2$.

Case two: $A=0$; $D=1$

The wavefunction for left and right leads:

$$\begin{cases} \psi_{jl} = \frac{t'}{\sqrt{V_l}} e^{-ik_{lj}} \\ \psi_{jr} = \frac{r'}{\sqrt{V_r}} e^{ik_{rj}} + \frac{e^{-ik_{rj}}}{\sqrt{V_l}} \end{cases} \quad 2.36$$

And then,

$$\begin{bmatrix} t' \\ r' \end{bmatrix} = \begin{bmatrix} S_{11} & S_{12} \\ S_{21} & S_{22} \end{bmatrix} \begin{bmatrix} 0 \\ 1 \end{bmatrix} \quad 2.37$$

Finally, there is $R' = I_{r'}/I_{in'} = |r'|^2 = |S_{22}|^2$, $T' = I_{t'}/I_{in'} = |t'|^2 = |S_{12}|^2$.

In summary, the scattering matrix S is represented by transmission and reflection coefficients as follows.

$$S = \begin{bmatrix} S_{11} & S_{12} \\ S_{21} & S_{22} \end{bmatrix} = \begin{bmatrix} r & t' \\ t & r' \end{bmatrix} \quad 2.38$$

Since $S^\dagger S = I$, then there is

$$\begin{bmatrix} r^* & t^* \\ t'^* & r'^* \end{bmatrix} \begin{bmatrix} r & t' \\ t & r' \end{bmatrix} = \begin{bmatrix} 1 & 0 \\ 0 & 1 \end{bmatrix} \quad 2.39$$

Now I obtain the important transport properties in terms of scattering theory.

$$|r|^2 + |t|^2 = 1 \quad 2.40$$

$$|t|^2 = |t'|^2; |r|^2 = |r'|^2 \quad 2.41$$

In summary, the transport properties are intrinsic where the transmission and reflection coefficients from one lead to the other are the same with the opposite injecting case.

2.2.3 Green's function

In this section, the Green's functions of simple models are listed.

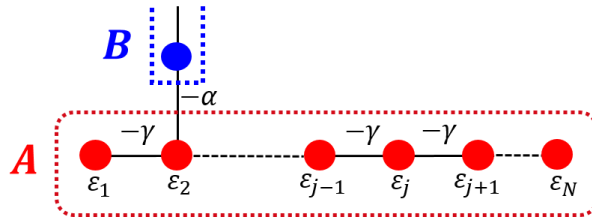


Fig. 2.2 System A with dangling source B. The hopping integral between A and source B is $-\alpha$. The connecting site can vary, for instance, site 2 is connected to the source.

The Green's function of system A in Fig. 2.2 satisfies,

$$\sum_{j=1}^N H_{ij} g_{jl} + \delta_{il} = E g_{il} \quad 2.42$$

The Schrödinger equation of the system $A + B$ shown in Fig. 2.2 is as follows,

$$\epsilon_j \psi_j - \gamma \psi_{j-1} - \gamma \psi_{j+1} - \alpha \phi \delta_{j2} = E \psi_j; 1 < j < N \quad 2.43$$

Now suppose that $-\alpha \phi$ is equal to -1, the equation goes to $\epsilon_j \psi_j - \gamma \psi_{j-1} - \gamma \psi_{j+1} + \delta_{j2} = E \psi_j$. Comparing this equation with Eq. 2.42, they are the same. Therefore, we can say the wavefunction of the whole system shown in Fig. 2.2 are the Green's function of system A in Fig. 2.2.

Next, the Green's function of an infinite chain is shown below.

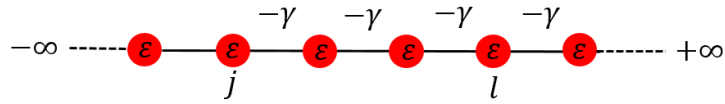


Fig. 2.3 Tight binding model for an infinite chain.

I now compute the Green's function of an infinite system (Fig. 2.3) with no boundaries, which satisfies

$$\varepsilon g_{jl} - \gamma g_{j+1,l} - \gamma g_{j-1,l} + \delta_{jl} = E g_{jl} \quad 2.44$$

Imagine we have the solution $g_{jl} = \begin{cases} A e^{ikj}; & (j \geq l) \\ B e^{-ikj}; & (j \leq l) \end{cases}$. When $j = l$, if $A = c e^{-ikl}$, $B = c e^{ikl}$, $g_{ll} = c$ is both obtained in terms of both sides. And from Eq. 2.44, we can get $\varepsilon g_{ll} - \gamma g_{l+1,l} - \gamma g_{l-1,l} + 1 = E g_{ll}$. Considering $E = \varepsilon - 2\gamma \cos k$, we have the following expression,

$$2\gamma \cos k g_{ll} - \gamma g_{l+1,l} - \gamma g_{l-1,l} = -1 \quad 2.45$$

we can have $\begin{cases} g_{l+1,l} = c e^{ik}; \\ g_{l-1,l} = c e^{-ik}; \end{cases}$ Then substitute $g_{l\pm 1,l}$ in Eq. 2.45, it is proved that $c =$

$\frac{1}{i\hbar V}$ where V is group velocity. Now the Green's function of infinite chain is written as follows which corresponds to the wavefunctions of the whole system shown in Fig. 2.4.

$$g_{jl} = \begin{cases} \frac{e^{ik(j-l)}}{i\hbar V}; & (j \geq l) \\ \frac{e^{-ik(j-l)}}{i\hbar V}; & (j \leq l) \end{cases} \quad \text{or} \quad g_{jl} = \frac{e^{ik|j-l|}}{i\hbar V} \quad 2.46$$

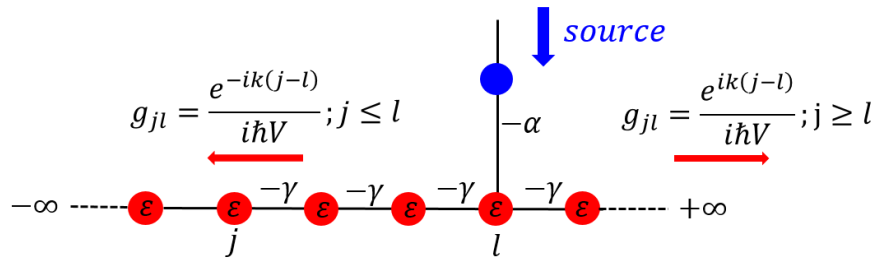


Fig. 2.4 Schematic for the wave functions of the whole system.

More generally, it is written as,

$$g_{jl} = \frac{e^{ik|j-l|}}{i\hbar V} + Ae^{ikj} + Be^{-ikj} \quad 2.47$$

2.2.4 Transmission function

A general transmission formula is derived and then a specific expression is further achieved in combination of Green's function method and Dyson's equation (see Appendix 1). Then the system extends from one-dimensional electrodes to the one with several electrodes. A generic expression of the transmission coefficients is obtained.

2.2.4.1 Junctions with two electrodes.

Firstly, I mainly take advantage of the property that the wavefunction of a system with source is the Green's function of the system without source. It is supposed that the wave function of the system is,

$$\begin{cases} \text{left lead: } \psi_{lj} = e^{ik_l j} + r e^{-ik_l j} \\ \text{right lead: } \psi_{rj} = \bar{t} e^{ik_r j} \end{cases} \quad 2.48$$

Next, I multiply the two formulae of Eq. 2.48 with $A = \frac{e^{-ik_l m}}{i\hbar V_l}$. Then new expressions are

$$\text{left lead: } \psi_{lj} = \frac{e^{ik_l(j-m)} + r e^{-ik_l(j-m)}}{i\hbar V_l} \quad 2.49$$

$$\text{right lead: } \psi_{rj} = \frac{\bar{t} e^{i(k_r j - k_l m)}}{i\hbar V_l} \quad 2.50$$

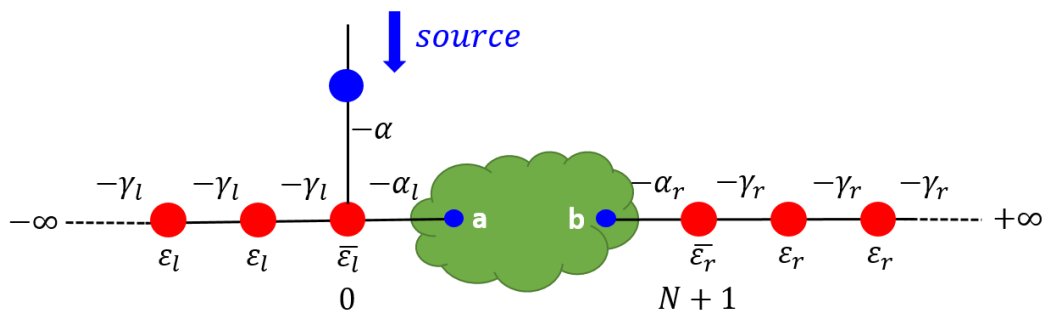


Fig. 2.5 Open system with a source and a backbone consisting of two semi-infinite electrodes and a scattering region.

The wave functions of the system shown in Fig. 2.5 have the same expressions with Eq. 2.49 and Eq. 2.50 for the left and right electrodes. Now I mark $\psi_{l,rj}$ as $g_{l,rjm}$.

$$\begin{cases} g_{ljm} = \frac{e^{ik_l(j-m)} + r e^{-ik_l(j-m)}}{i\hbar V_l} \\ g_{rjm} = \frac{\bar{t} e^{i(k_r j - k_l m)}}{i\hbar V_l} \\ m = 0 \text{ (arbitrary value)} \end{cases} \quad 2.51$$

$$\Rightarrow \begin{cases} r = i\hbar V_l g_{00} - 1 \\ t = \bar{t} \sqrt{\frac{V_r}{V_l}} = i\hbar \sqrt{V_r V_l} g_{N+1,0} e^{-ik_r(N+1)} \end{cases}$$

Now the transmission coefficient of the backbone without source could be achieved by the following formula.

$$T(E) = tt^* = \hbar V_l \hbar V_r |g_{N+1,0}|^2 \quad 2.52$$

Further derivation for more specific expression is presented below.

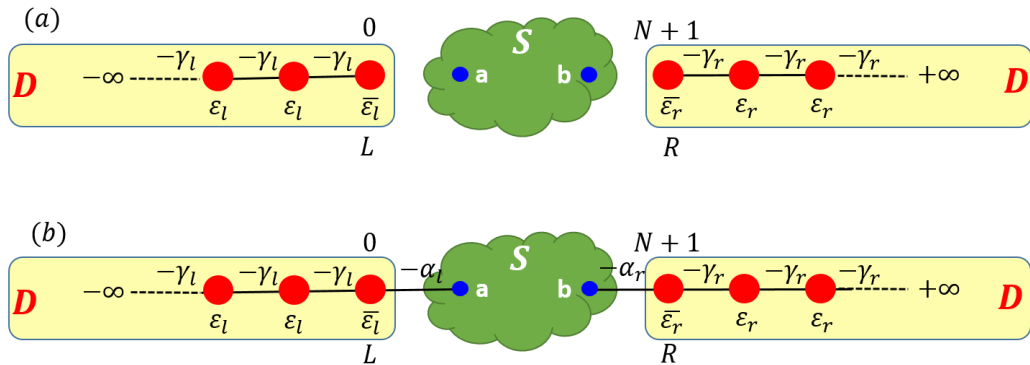


Fig. 2.6 (a) Isolated semi-infinite left, right electrodes (yellow regions) and scattering region with N sites (green region). 0 and $N+1$ represent the surfaces of

the electrodes which are also denoted as L and R. (b) Open and non-periodic system constituted by the isolated moieties in (a). The regions of electrodes are denoted as D while that of scattering region is denoted as S.

The Green's functions of the starting system shown in Fig. 2.6(a) are shown below.

$$\bar{g} = \begin{bmatrix} g_D & 0 \\ 0 & g_S \end{bmatrix}; g_D = \begin{bmatrix} g_L & 0 \\ 0 & g_R \end{bmatrix}; g_S = \begin{bmatrix} g_{aa} & 0 \\ 0 & g_{bb} \end{bmatrix} \quad 2.53$$

The difference between systems a and b is

$$h_1 = \begin{bmatrix} 0 & h_{DS} \\ h_{SD} & 0 \end{bmatrix}; h_{DS} = \begin{bmatrix} -\alpha_l & 0 \\ 0 & -\alpha_r \end{bmatrix} = h_{SD} \quad 2.54$$

Next we use Dyson equation: $\bar{G} = (\bar{g}^{-1} - \bar{H}_1)^{-1}$ to achieve the expressions for transport properties. Solve the equations to obtain:

$$G_{SD} = g_S h_{SD} G_{DD} \quad 2.55$$

$$G_{DD} = g_D + g_D h_{DS} G_{SS} h_{SD} g_D \quad 2.56$$

$$\Rightarrow \begin{bmatrix} \alpha_l^2 (G_{SS})_{aa} g_L g_L + g_L & g_L \alpha_l (G_{SS})_{ab} \alpha_r g_R \\ g_L \alpha_l (G_{SS})_{ba} \alpha_r g_R & \alpha_r^2 (G_{SS})_{bb} g_R g_R + g_R \end{bmatrix}$$

$$G_{SS} = (g_S^{-1} - h_{SD} g_D h_{DS})^{-1} \quad 2.57$$

$$\Rightarrow \frac{\delta}{\Delta} \begin{bmatrix} (g_{aa} - \delta \alpha_r^2 g_R) & g_{ab} \\ g_{ba} & (g_{bb} - \delta \alpha_l^2 g_L) \end{bmatrix}$$

Where $\delta = g_{aa} g_{bb} - g_{ab} g_{ba}$ and

$$d^{-1} = \frac{\delta}{\Delta} = (1 - g_{aa}\alpha_l^2 g_L - g_{bb}\alpha_r^2 g_R + \alpha_l^2 \alpha_r^2 g_L g_R \delta)^{-1} \quad 2.58$$

$$\begin{cases} (G_{DD})_{LL} = \alpha_l^2 (G_{SS})_{aa} g_L g_L + g_L \\ (G_{DD})_{RR} = \alpha_r^2 (G_{SS})_{bb} g_R g_R + g_R \end{cases} \quad 2.59$$

And

$$(G_{DD})_{RL} = g_L \alpha_l (G_{SS})_{ba} \alpha_r g_R \quad 2.60$$

And also

$$(G_{SS})_{ba} = \frac{\delta}{\Delta} g_{ba} \quad 2.61$$

Finally, according to the Eq. 2.51 and Eq. 2.52,

$$t = i\hbar\sqrt{V_l V_r} \alpha_l g_l g_{ba} \alpha_r g_r \frac{\delta}{\Delta} e^{-ik_r(N+1)} \quad 2.62$$

$$T(E) = tt^* = |t|^2 = \frac{\hbar V_l \hbar V_r \alpha_l^2 |g_l|^2 |g_{ba}|^2 \alpha_r^2 |g_r|^2}{|d|^2} \quad 2.63$$

2.2.4.2 A junction with N electrodes.

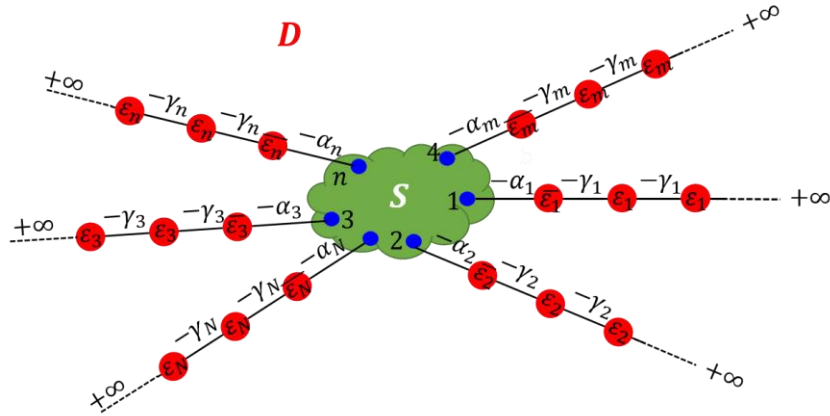


Fig. 2.7 A scattering problem with n electrodes. The green part denotes the scattering region. The blue circles in scattering region represent the contact sites with electrodes. $\bar{\epsilon}_n$ is on-site energy of the electrode surface which is slightly different from the sites inside the electrode due to the influence of the scattering region. D denotes the region of all the electrodes while S is for the scattering region.

As for the region D of n electrodes, the Green's function is marked as

$$g_D = \sum_{j=1}^N |j\rangle g_j \langle j| = \begin{bmatrix} g_1 & 0 & 0 & 0 \\ 0 & g_2 & 0 & 0 \\ 0 & 0 & \ddots & 0 \\ 0 & 0 & 0 & g_N \end{bmatrix}; |j\rangle = \begin{bmatrix} 0 \\ 1 \\ \vdots \\ 0 \end{bmatrix} \quad 2.64$$

There is $\langle n|g_D = g_n \langle n|$, and $g_D|m\rangle = |m\rangle g_D$. Based on Dyson equation and the expressions in section 2.56, we have

$$(G_{DD})_{nm} = \langle n|g_D|m\rangle + \langle n|g_D h_{DS} G_{SS} h_{SD} g_D|m\rangle \quad 2.65$$

When $m \neq n$, there is $\langle n|g_D|m\rangle = 0$, and then

$$(G_{DD})_{nm} = g_n \langle B_n | G_{SS} | B_m \rangle g_m \quad 2.66$$

Where $\langle n | h_{DS} = \langle B_n |, h_{DS} | m \rangle = | B_m \rangle$. Using this equation, there is

$$\begin{aligned} |(G_{DD})_{nm}|^2 &= |g_n|^2 \langle B_n | G_{SS} | B_m \rangle \langle B_m | G_{SS}^\dagger | B_n \rangle |g_m|^2 \quad 2.67 \\ &= Tr\{ [|B_n\rangle |g_n|^2 \langle B_n|] G_{SS} [|B_m\rangle |g_m|^2 \langle B_m|] G_{SS}^\dagger \} \end{aligned}$$

Due to $|B_n\rangle |g_n|^2 \langle B_n| = \frac{2\Gamma(n)}{\hbar v_n}$, finally we get

$$T_{nm} = 4Tr(\Gamma(n)G_{SS}\Gamma(m)G_{SS}^\dagger) \quad 2.68$$

As for G_{SS} , according to the Eq. 2.57, we have $G_{SS} = (g_{SS}^{-1} - \Sigma)^{-1}$.

$$\Sigma = \sigma - i\Gamma = h_{SD}g_D h_{DS} = \sum_{n=1}^N h_{SD}|n\rangle g_D \langle n|h_{DS} = \sum_{n=1}^N \Sigma(n) \quad 2.69$$

An example is as follows:

If only one site ε_s exists in the scattering region, then $G_{SS} = (E - \varepsilon_s - \Sigma)^{-1}$ and

$$T_{nm} = \frac{4\Gamma(n)\Gamma(m)}{(E - \varepsilon_s - \sigma)^2 + \Gamma^2} \text{ where } \Sigma = \sigma - i\Gamma = \sum_{n=1}^N \Sigma(n).$$

As shown in Fig. 2.7, when electrons are injected from more than one electrode (open conduction channels) simultaneously, and detected the total transmitted electrons from other left electrodes (open conduction channels). Then transmission function is

$$T(E) = \sum_j T_{nm}(E) \quad 2.70$$

Which demonstrate the transmission with several conduction channels in two electrodes.

2.2.5 Breit-Wigner resonance

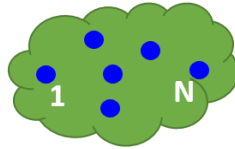


Fig. 2.8 An isolated system containing N sites.

The Schrödinger equation is $H|\psi_n\rangle = E_n|\psi_n\rangle$. The following shows important properties: $\langle\psi_n|\psi_m\rangle = \delta_{nm}$ and $\sum_{n=1}^N |\psi_n\rangle\langle\psi_n| = I$ in terms of normalised eigenstates.

Based on the above basic equations, the definition of Green's function, there is

$$g = (E - H)^{-1}I = \sum_{n=1}^N (E - H)^{-1}|\psi_n\rangle\langle\psi_n| = \sum_{n=1}^N \frac{|\psi_n\rangle\langle\psi_n|}{(E - E_n)} \quad 2.71$$

If $E \approx \lambda$ which is a nondegenerate eigenvalue of the Hamiltonian, then the Green's function is approximately

$$g \approx \frac{|\psi_\lambda\rangle\langle\psi_\lambda|}{E - \lambda} = \begin{bmatrix} g_{11} & g_{12} & \cdots & g_{1N} \\ g_{21} & g_{22} & \cdots & g_{2N} \\ \vdots & \vdots & \cdots & \vdots \\ g_{N1} & g_{N2} & \cdots & g_{NN} \end{bmatrix} \quad 2.72$$

Where $|\psi_\lambda\rangle$ is the corresponding eigen state,

$$|\psi_\lambda\rangle = \begin{bmatrix} \phi_1 \\ \phi_2 \\ \vdots \\ \phi_N \end{bmatrix} \quad 2.73$$

Then we can obtain the elements of Green's function below

$$g_{11} = \frac{|\phi_1|^2}{E - \lambda}; \quad g_{NN} = \frac{|\phi_N|^2}{E - \lambda} \quad 2.74$$

$$g_{1N} = \frac{\phi_1\phi_N^*}{E - \lambda}; \quad g_{N1} = \frac{\phi_N\phi_1^*}{E - \lambda}; \quad 2.75$$

So we have $g_{11}g_{NN} = g_{1N}g_{N1}$. Here, it is assumed that $\bar{\varepsilon}_{l(r)} = \varepsilon_{l(r)}$. Then $g_{l(r)} =$

$\frac{e^{ik_l(r)}}{-\gamma_{l(r)}}$. According to Eq.2.62, 2.63, there is

$$d = 1 - g_l\alpha_l^2g_{11} - g_r\alpha_r^2g_{NN} \quad 2.76$$

$$t = \frac{i\hbar\sqrt{V_lV_r}\alpha_l\alpha_re^{ik_l}e^{ik_r}}{\gamma_l\gamma_r} \left(\frac{\phi_N\phi_1^*}{E - \lambda - \Sigma_l - \Sigma_r} \right) \quad 2.77$$

Where self-energy $\Sigma_l = g_l\alpha_l^2|\phi_1|^2, \Sigma_r = g_r\alpha_r^2|\phi_N|^2$.

$$\begin{aligned}
 T = |t|^2 &= \frac{2\sin k_l 2\sin k_r \alpha_l^2 \alpha_r^2}{\gamma_l \gamma_r} \left(\frac{|\phi_N|^2 |\phi_1|^2}{(E - \lambda - \sigma)^2 + \Gamma^2} \right) & 2.78 \\
 &= \frac{4\bar{\Gamma}_l \bar{\Gamma}_r}{(E - \lambda - \bar{\sigma}_l - \bar{\sigma}_r)^2 + (\bar{\Gamma}_l + \bar{\Gamma}_r)^2}
 \end{aligned}$$

Where $\bar{\sigma}_l = \frac{|\phi_1|^2 \alpha_l^2 \cos k_l}{\gamma_l}$, $\bar{\sigma}_r = \frac{|\phi_N|^2 \alpha_r^2 \cos k_r}{\gamma_r}$, $\bar{\Gamma}_l = \frac{|\phi_1|^2 \alpha_l^2 \sin k_l}{\gamma_l}$, $\bar{\Gamma}_r = \frac{|\phi_N|^2 \alpha_r^2 \sin k_r}{\gamma_r}$. $\bar{\sigma}_{l(r)}$ and $\bar{\Gamma}_{l(r)}$ corresponds to the real and imaginary parts of self-energy $\Sigma_{l(r)}$.

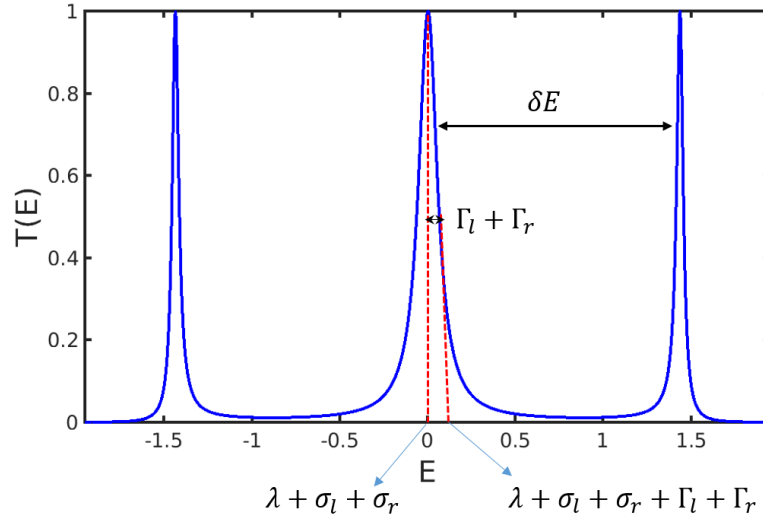


Fig. 2.9 Three Breit-Wigner peaks in one transmission spectra $T(E)$. The longer red dashed vertical line shows the on-resonance position $E = \lambda + \sigma_l + \sigma_r$ while the shorter one represents the position $E = \lambda + \sigma_l + \sigma_r + \Gamma_l + \Gamma_r$ at half maximum value. In consequence, the corresponding half width of half maximum value is $\Gamma_l + \Gamma_r$. δE shows the energy level which is much larger than the resonance width $\Gamma_l + \Gamma_r$ for all three peaks. Obviously, they are Breit-Wigner resonances.

Features:

1. The resonance corresponds to nondegenerate eigenstate

2. If $\Gamma = \Gamma_l + \Gamma_r$ is much less than the level spacing δE of the scattering region, then Breit-Wigner formula can be used.
3. When $\Gamma_l = \Gamma_r$, the on-resonance value is the maximum 1.
4. When $\Gamma_l \ll \Gamma_r$, transmission coefficient on resonance is approximately equal to $4\Gamma_l/\Gamma_r$.

2.3 Fundamental properties

In the study of molecular devices, experimentally and theoretically, properties or functionalities are discovered and understood which indicate their possible future prospect in integrated circuits. Here, I present the thermoelectric properties, the phenomenon of Coulomb blockade in single electron transistors, the observation of noise spectroscopy for the molecular devices which are closely correlated to my work in the following chapters.

2.3.1 Thermoelectricity

The Seebeck coefficient is defined as the voltage difference $\Delta V = V_1 - V_2$ generated due to a temperature difference $\Delta T = T_1 - T_2$ of the two electrodes which are connected to two hot and cold reservoirs respectively. In what follows, first, the sign of the Seebeck coefficient is discussed depending on which transmission peak (HOMO or LUMO) dominates the transmission. Next, the derivation for a series of thermoelectric equations is presented. Finally, the figure of merit ZT and two types of thermoelectric efficiency η (the efficiency at

maximum output power and the maximum efficient) are introduced to further characterise a thermoelectric generator.

2.3.1.1 The sign of Seebeck coefficient (S)

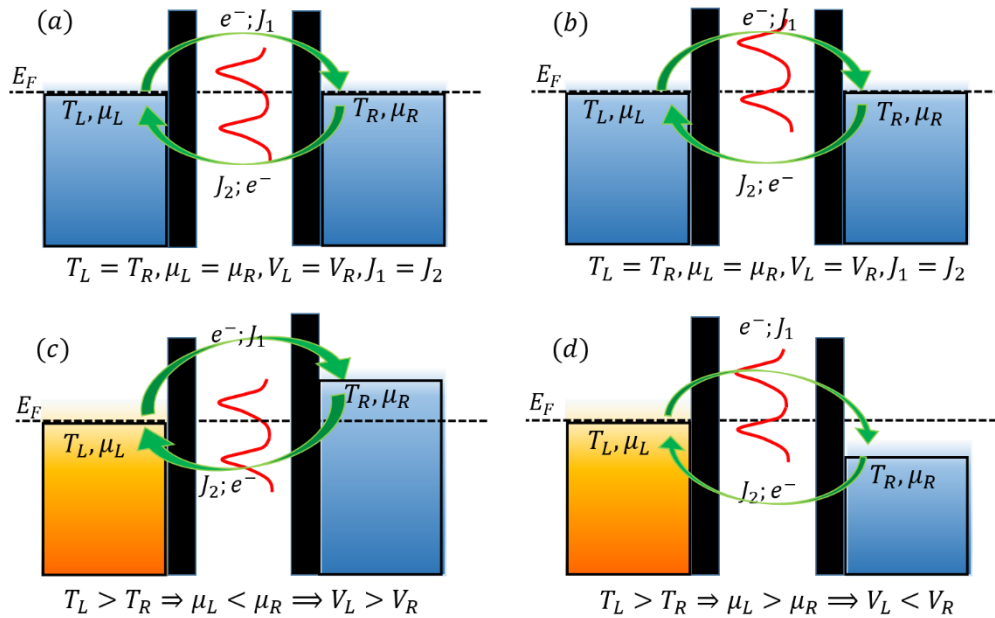


Fig. 2.10 Different signs for Seebeck coefficient when the system is HOMO-dominated (a, c) and LUMO-dominated (b, d) transport. LUMO-dominated transport corresponds to a negative Seebeck coefficient while HOMO-dominated gives a positive Seebeck coefficient.

Fig. 2.10 shows the energy level alignment for molecular devices consisting of two electrodes connected to two reservoirs labelled L, R and a single molecule. The voltages and temperatures of the reservoirs are denoted as V_L, T_L and V_R, T_R . Define $\Delta V = V_L - V_R$ and $\Delta T = T_L - T_R$. Chemical potentials are $\mu_L = E_F + eV_L, \mu_R = E_F + eV_R$, where $e = -|e|$ and their difference is $\Delta\mu = \mu_L - \mu_R = e\Delta V$. Define the steady-state particle current J_1 to be the number of electrons per unit time leaving reservoir L and entering reservoir R through the scattering region

and the steady-state particle current J_2 to be the number of electrons per unit time leaving reservoir R and entering reservoir L. The net particle current leaving reservoir L and entering reservoir R is $J = J_1 - J_2$ and the electrical current is $I = eJ$ where $e = -|e|$. In Fig. 2.10c and d, the Seebeck coefficient S is defined as $= -\left(\frac{\Delta V}{\Delta T}\right)_{I=0}$, where $\Delta V = V_L - V_R$ is the open circuit voltage difference produced by a temperature difference $\Delta T = T_L - T_R$.

To obtain the sign of S , start from the equilibrium condition $\Delta V = 0$, $\Delta T = 0$ (Fig. 2.10a) and consider what happens when the temperature T_L of the left reservoir is increased, such that the population of higher-energy electrons in reservoir L is higher than that of reservoir R. If these higher-energy electrons find it easier to pass from reservoir L to reservoir R than lower-energy electrons, then J_1 will increase where LUMO-dominated transport happens shown in Fig. 2.10c. To achieve steady state the steady-state condition $J = 0$, μ_R must increase, so that J_2 increases. This demonstrates that if $T_L > T_R$, $\mu_R > \mu_L$. Hence if $\Delta T > 0$, $\Delta\mu < 0$, $\Delta V > 0$ and $S < 0$. This above situation occurs when the Fermi energy is in the HOMO-LUMO gap of a single molecule and located closer to the LUMO, because in this case the electron transmission coefficient is an increasing function of electron energy. It also occurs when the Fermi energy is in the band gap of a semiconductor and closer to the conduction band.

Conversely, if the Fermi energy is located closer to the HOMO or to the valence band (Fig. 2.10b), higher-energy electrons find it more difficult to pass from reservoir L to reservoir R than lower-energy electrons, then if T_L is increased relative to T_R , J_1 will decrease and $S > 0$ (Fig. 2.10d).

2.3.1.2 Thermoelectrical expression

Based on the Landauer formula[56], there are expressions for electron current and heat current [57] due to electrons as follows:

$$I = \frac{2e}{h} \int_{-\infty}^{+\infty} dE T(E) [f_L(E) - f_R(E)] \quad 2.79$$

$$\dot{Q} = \frac{2}{h} \int_{-\infty}^{+\infty} dE (E - E_F) T(E) [f_L(E) - f_R(E)] \quad 2.80$$

Where $f_{L,R}(E) = \frac{1}{e^{-\frac{E-\mu_{L,R}}{k_B T}} + 1}$, $\mu_{L,R} = E_F \pm eV_b/2$. By Taylor expanding of $f_{L,R}(\mu, T)$ at point ($\mu = E_F, T = (T_L + T_R)/2$) and keeping the first order only when the temperature difference and bias are both small. And then substitute ($\mu_{L,R}, T_{L,R}$) in $f(\mu, T)$. Consequently,

$$\begin{aligned} f(\mu_L, T_L) &= f(E_F, T) + \frac{\partial f(E_F, T)}{\partial \mu} (\mu_L - E_F) \\ &\quad + \frac{\partial f(E_F, T)}{\partial T} (T_L - T) \end{aligned} \quad 2.81$$

$$\begin{aligned} f(\mu_R, T_R) &= f(E_F, T) + \frac{\partial f(E_F, T)}{\partial \mu} (\mu_R - E_F) \\ &\quad + \frac{\partial f(E_F, T)}{\partial T} (T_R - T) \end{aligned} \quad 2.82$$

Then we have

$$\begin{aligned}
 f_L - f_R &= \frac{\partial f(E_F, T)}{\partial \mu} (\mu_L - \mu_R) + \frac{\partial f(E_F, T)}{\partial T} (T_L - T_R) \\
 &= - \left. \frac{df(E)}{dE} \right|_{\mu=E_F, T} (e\Delta V) - \left. \frac{df(E)}{dE} \right|_{\mu=E_F, T} \frac{E - E_F}{T_0} (\Delta T)
 \end{aligned} \tag{2.83}$$

where $e = -|e|$. Then combining Eq.s 2.79 ~ 2.83, we obtain the following expression,

$$I = \frac{2e}{h} \int_{-\infty}^{+\infty} dE T(E) \left(- \left. \frac{df(E)}{dE} \right|_{\mu=E_F, T} \right) \left[e\Delta V + \frac{E - E_F}{T} \Delta T \right] \tag{2.84}$$

$$\begin{aligned}
 \dot{Q} &= \frac{2}{h} \int_{-\infty}^{+\infty} dE (E - E_F) T(E) \left(- \left. \frac{df(E)}{dE} \right|_{\mu=E_F, T} \right) \left[e\Delta V \right. \\
 &\quad \left. + \frac{E - E_F}{T} \Delta T \right]
 \end{aligned} \tag{2.85}$$

Now we have the matrix expression,

$$\begin{pmatrix} I \\ \dot{Q} \end{pmatrix} = \frac{2}{h} \begin{pmatrix} e^2 L_0 & \frac{eL_1}{T} \\ eL_1 & \frac{L_2}{T} \end{pmatrix} \begin{pmatrix} \Delta V \\ \Delta T \end{pmatrix} \tag{2.86}$$

Where $(T = \frac{(T_L + T_R)}{2}, \mu = E_F)$ is the reference temperature and chemical potential (Fermi level of the system in the equilibrium), and $L_n = \int_{-\infty}^{+\infty} dE (E - E_F)^n T(E) \left(- \frac{df(E)}{dE} \right)$. The Fermi-Dirac distribution $f_{L,R}(E) = \frac{1}{e^{\frac{E - (E_F \pm eV_b/2)}{k_B T}} + 1}$.

When $\Delta T = 0$, Eq. 2.86 give us the electric conductance,

$$G = \frac{2e^2}{h} L_0 \quad 2.87$$

Which is just the conductance in finite temperature and zero bias limit shown in Eq.2.15.

When $I = 0$, Eq. 2.86 gives us the Seebeck coefficient $S = -\left(\frac{\Delta V}{\Delta T}\right)_{I=0}$,

$$S = \frac{L_1}{eTL_0} \quad 2.88$$

Where $e = -|e|$.

Alternatively, the Eq. 2.86 can be rearranged into

$$\begin{pmatrix} I \\ \dot{Q} \end{pmatrix} = \begin{pmatrix} G & GS \\ GST & K \end{pmatrix} \begin{pmatrix} \Delta V \\ \Delta T \end{pmatrix} \quad 2.89$$

$$\begin{pmatrix} \Delta V \\ \dot{Q} \end{pmatrix} = \begin{pmatrix} 1/G & -S \\ \Pi & \kappa_e \end{pmatrix} \begin{pmatrix} I \\ \Delta T \end{pmatrix} \quad 2.90$$

Where Peltier coefficient is $\Pi = ST = \frac{L_1}{eL_0}$, the thermal conductance due to electrons is $\kappa_e = K - GS^2T = \frac{2}{hT} \left(L_2 - \frac{(L_1)^2}{L_0} \right)$. In terms of these quantities, the electric contribution to thermoelectric figure of merit is $ZT_e = \frac{S^2GT}{\kappa_e} = \frac{(L_1)^2}{L_0L_2 - (L_1)^2}$.

[58]

When energy is close to Fermi level E_F and transmission spectrum varies approximately linearly with energy E in the scale of $k_B T$, then there are

expressions $L_0 \approx T(E_F)$, $L_1 \approx (eT)^2 \alpha \left. \frac{dT(E)}{dE} \right|_{E=E_F}$, $L_2 \approx (eT)^2 \alpha T(E_F)$ where the

Lorenz number $\alpha = \left(\frac{1}{eT}\right)^2 \int_{-\infty}^{+\infty} dE (E - E_F)^2 \left(-\frac{df(E)}{dE}\right) = 2.44 \times 10^{-8} W \cdot \Omega \cdot K^{-2}$.

In the derivation of the above expressions, Taylor expansion for transmission

coefficient $T(E) = T(E_F) + \left. \frac{d(T(E))}{dE} \right|_{E=E_F} + \dots$ is required. Based on these

approximations, there is.

$$S \approx eT \alpha \left. \frac{d \ln[T(E)]}{dE} \right|_{E=E_F} \quad 2.91$$

$$\kappa_e \approx \alpha T G \quad 2.92$$

So the Seebeck coefficient S could be enhanced by increasing the slope of transmission spectra $T(E)$. Eq. 2.92 demonstrates the Wiedemann–Franz law

which states thermal conductance from electronic contribution against electrical

conductance is proportional to temperature T where $\alpha = 2.44 \times 10^{-8} W \Omega K^{-2}$ is

the Lorenz number. In basis of Wiedemann-Franz law, there is $ZT_e = \frac{S^2}{\alpha}$. As for

$ZT_e > 1, S > 150 \mu V/K$.

As for $I = G \Delta T + G \Delta V$, the two terms correspond to the two current paths of J_1

and J_2 shown in Fig. 2.11. ΔT is the electromotive force of the thermoelectric

device and $\Delta V = V_L - V_R$ is the output voltage on load. When $I=0$, $\Delta T = -\Delta V$.

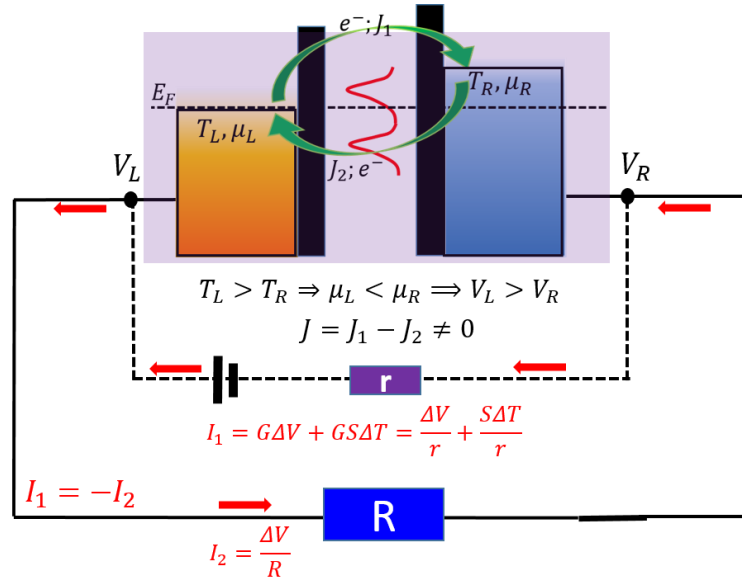


Fig. 2.11 Effective replacement (a battery with an inner resistance r) of the molecular device (the light purple region). $\Delta V = -S\Delta T$ in open effective circuit where $I = 0$, $\Delta V = V_L - V_R$ and $I = G\Delta V + GS\Delta T$ in closed effective circuit where $I \neq 0$ and $\Delta V = V_L - V_R$. The red arrows show the current in the effective circuit. The magnitude of all the currents ($|I_1| = |I_2|$) is the same. The direction of current is the same with that of the voltage ΔV . E_F is the Fermi level for the equilibrium system. $\mu_{L,R}$ is the chemical potential for the reservoirs.

So far we have ignored phonons, whose contribution to the thermal conductance is

$$\kappa_{ph}(T) = \frac{1}{2\pi} \int_0^\infty d\omega \hbar\omega T_{ph}(\omega) \frac{\partial f_{BE}(\omega, T)}{\partial T} \quad 2.93$$

Where $f_{BE}(\omega, T) = \left(e^{\frac{\hbar\omega}{k_B T}} - 1 \right)^{-1}$ is the Bose-Einstein distribution function and

$T_{ph}(\omega)$ is the transmission coefficient for phonons of energy $\hbar\omega$. Then the

thermoelectric figure of merit is $ZT = \frac{S^2 GT}{\kappa_e + \kappa_{ph}}$.

2.3.1.3 Thermoelectric efficiency η

Thermoelectric efficiency is defined as,

$$\eta = \frac{\text{energy provided to the load}}{\text{heat extracted from the hot reservoir per unit time}} \quad 2.94$$

That is to say,

$$\eta = \frac{-I\Delta V}{S\Delta TI + \kappa\Delta T} \quad 2.95$$

Where $I = I_1 = -I_2$.

- a. Efficiency at maximum output power

When the output power is maximum, that needs $r = R$ in Fig. 2.11. That is to say, $\Delta V = -S\Delta T/2$ and $I = GS\Delta T/2$. So the relationship between thermoelectric efficiency η and thermoelectric figure of merit ZT in this case is

$$\eta_{maxP} = \frac{\frac{GS\Delta T}{2} \cdot \frac{S\Delta T}{2}}{\frac{STGS\Delta T}{2} + \kappa\Delta T} = \frac{\Delta T}{2T} \cdot \frac{ZT}{ZT + 2} \quad 2.96$$

- b. The maximum efficiency

The above efficiency at maximum power is not the maximum efficiency. The maximum efficiency η_{max} is obtained by differentiating Eq. 2.95 with respect to ΔV and setting the result to zero. This yields the following expression.

$$\eta_{max} = \frac{\Delta T \sqrt{ZT + 1} - 1}{T \sqrt{ZT + 1} + 1} \quad 2.97$$

Both the efficiency at maximum power $\eta_{\max P}$ and the maximum efficiency η_{\max} achieve their maximum values when ZT tends to infinity. The derivation for maximum thermoelectric efficiency is shown in Appendices (Appendix 2).

2.3.2 Coulomb blockade

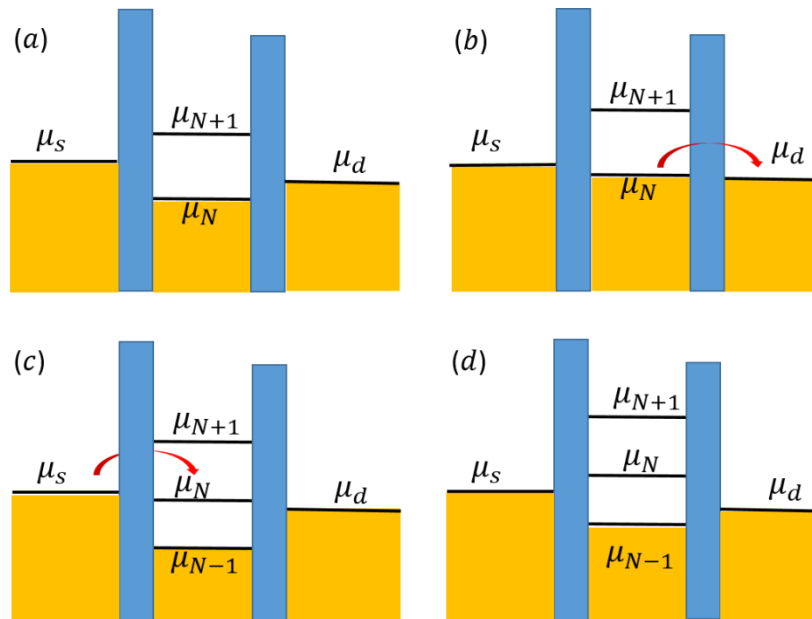


Fig. 2.12 Energy alignment for a single-electron transistor. (a), (d) Electron is blocked and the number of electrons in the dot is N and $N-1$, respectively. (b), (c) these two alignments almost happen simultaneously and in consequence the current forms. The number of charge in the dot fluctuates between $N-1$ and N . Energy level is $\Delta E = \mu_N - \mu_{N-1}$.

Current in a tunnel junction is formed by the passing of exact one electron through the tunnel barrier (The case of two-electron simultaneous tunnelling is out of consideration.) since the electrical charge is discrete. In consequence, a voltage $U = e/C$ is built up due to the charged tunnel junction, where $e = 1.6 \times 10^{-19}$ coulomb is the elementary charge and $C = e^2/\Delta E$ is the capacitance of the junction. Here, ΔE is the energy level spacing between level N and $N - 1$. Considering a small capacitance, a large voltage buildup is achieved which could hold back a second electron from tunnelling. This phenomenon around zero bias is named Coulomb blockade.

In order to observe the Coulomb blockade, the schematic of sequential tunnelling is depicted in Fig. 2.12 under small bias ($V_b < e/C$) and at low temperature ($k_B T < e^2/2C$) in terms of the energy diagram of a double tunnel barrier arrangement. Transport through the scattering region is blocked with N electrons on the dot in Fig. 2.12(a). By decreasing the gate voltage, the chemical potential μ_N inside the molecule is raised until it approximately aligns with that of the drain contact ($\mu_s \cong \mu_N$) and an electron can leave the dot. If at the same time $\mu_s \geq \mu_d$, a current can flow from source to drain and the number of electrons on the dot will fluctuate between N and $N-1$. When the gate voltage further decreases and $\mu_s < \mu_N$ the dot is left with one electron less and the current is again blocked. In summary, we therefore have a peak in the conductance whenever $\mu_N \approx \mu_s \approx \mu_d$ for a small bias.

In such a process above, the electron tunnels from the source electrode, to the molecule, and to the drain which is on-resonant tunnel. According to Heisenberg's uncertainty principle, the time of electron staying on the molecule is larger in the

case where weak coupling occurs between source and molecule and between molecule and drain. So this indicates that the electrons have sufficient time in the molecule to interact with other degrees of freedom which could lead to incoherent tunnelling. Two types of this incoherent tunnel are recognised. One is the case of elastic tunnelling due to the associated loss of phase, whereas the second case is inelastic tunnelling originating from the loss of both phase and energy [59].

2.3.3 Applying a vector field

An electromagnetic vector potential \vec{A} is related to a magnetic field B by the curl of \vec{A} ,

$$\begin{aligned} B\hat{z} = \nabla \times \vec{A} &= \begin{vmatrix} \hat{i} & \hat{j} & \hat{k} \\ \frac{\partial}{\partial x} & \frac{\partial}{\partial y} & \frac{\partial}{\partial z} \\ A_x & A_y & A_z \end{vmatrix} & 2.98 \\ &= \left(\frac{\partial A_z}{\partial y} - \frac{\partial A_y}{\partial z} \right) \hat{i} + \left(\frac{\partial A_x}{\partial z} - \frac{\partial A_z}{\partial x} \right) \hat{j} \\ &\quad + \left(\frac{\partial A_y}{\partial x} - \frac{\partial A_x}{\partial y} \right) \hat{k} \end{aligned}$$

Where the direction \hat{z} of B is subject to right-hand rule. There is some gauge freedom to choose the vector potential \vec{A} for a given perpendicular uniform magnetic field $\vec{B} = B\hat{z}$, such as the Landau gauge $\vec{A} = xB\hat{y}$ or a symmetric gauge $\vec{A} = \frac{B}{2}(x\hat{y} - y\hat{x})$. The physics of the system is gauge invariant, which means that adding the gradient of a scalar field to \vec{A} changes the overall phase of the wave

function by an amount corresponding to the scalar field. But physical properties are not influenced by the specific choice of gauge. In addition, magnetic flux is associated with this vector potential through the formula $\phi = \oint \vec{A} dl$.

The Peierls substitution describes tightly-bound electrons in the presence of a slowly varying magnetic vector potential. Based on this, there is a relationship between the hopping integral γ_{ij} between two sites and the magnetic vector potential,

$$\tilde{\gamma}_{ij} = \gamma_{ij} e^{\frac{ie}{\hbar} \int_i^j \vec{A} dl} = \gamma_{ij} e^{i2\pi \frac{\int_i^j \vec{A} dl}{\phi_0}} \quad 2.99$$

Where $\phi_0 = \frac{2\pi\hbar}{e}$ is the quantum of flux.

2.3.4 Noise spectroscopy

Noise characteristics play an important role in understanding conductance fluctuations and other fundamental information in molecular devices. In general, electrical noise is classified into four types: (a) thermal noise, (b) shot noise, (c) generation-recombination noise and (d) flicker or 1/f noise[60] where the first two types are frequency-independent, therefore called 'white noise' and the left two types are frequency dependent.

As for thermal noise, it happens in equilibrium situations where the electrical current is zero. This noise is due to the fluctuations in the quantum mechanical occupation of electronic states which is temperature-dependent. The resulting

noise power spectral density $S_I(f) = \lim_{T \rightarrow \infty} \frac{\overline{2|I(f)|^2}}{T}$ where $I(f)$ is the Fourier transform of $I(t)$ [61] is frequency f independent and described by the well-known Johnson-Nyquist theorem[62][63]: $S_I(f) \cong 4k_B T G$. Completely different from thermal noise, the shot noise arises from the discrete nature of carriers and happens only when the electrical current is nonzero and flows through a defined barrier which is due to a non-equilibrium phenomenon.[64] Shot noise can be exploited to analyse the correlation among different conductance channels through formula $S_I(f) = 2eI \left(1 - \frac{\sum_1^n \tau_i^2}{\sum_1^n \tau_i}\right)$ in the limit of low temperatures where τ_i is the transmission coefficient for a conductance channel.[65][66]

In terms of the frequency-dependent noise, the noise power spectral density (PSD) of a symmetric random telegraph signal (RTS) is $S(f) = \frac{2(\Delta I)^2 \bar{\tau}}{4 + (2\pi f \bar{\tau})^2}$ where $\bar{\tau}$ is the mean dwell time for up or down current level, put in another way, the mean life-time for each process of trapping-detrapping or generation-recombination of electrons, and ΔI is the deviation of the two current levels. [61] For the $1/f$ noise, no generic model or theory is proposed even though this noise is always observed in all kinds of electronic devices.[67] In basis of RTS noise with Lorentzian profile, McWhorter's model for $1/f$ noise in conventional semiconductors is proposed, where the PSD is equal to the superposition of the counterparts of different Lorentzian noises, that is, $S_I(f) \propto \int_{\tau_1}^{\tau_2} g(\tau) \frac{\tau}{1 + (2\pi f \tau)^2} d\tau$ where $g(\tau) = \left[\tau \ln \left(\frac{\tau_2}{\tau_1} \right) \right]^{-1}$ and the life-time τ spreads in a logarithmically wide time scale $[\tau_1, \tau_2]$. [60]

3 Thermoelectricity in vertical graphene-C₆₀-graphene architectures

3.1 Introduction

Molecular devices consisting of single or multiple molecules bridging two or more electrodes have attracted intense theoretical and experimental interest, due to their tunable and unique transport properties, including negative differential resistance (NDR)[68][69][19], electrical switching [70][71][12] and thermoelectric power generation [72][73][74][75][21][55][76]. The conversion of a temperature gradient ΔT to a voltage difference ΔV , is controlled by the Seebeck coefficient $S = -\Delta V/\Delta T$. Common inorganic thermoelectric materials such as Pb, Bi, Co, Sb are toxic and expensive due to limited global sources. Therefore, in recent years, different strategies have been proposed to exploit the thermoelectric properties of nanostructured organic materials or organic molecules [77][78][79][22][80]. At the single-molecule level, the Seebeck coefficient can be controlled using a gate electrode in a three-terminal device[81]. Furthermore, the sign and magnitude of S can be changed by modulating the

coupling of the molecule to electrodes using the pressure induced by a STM tip [74]. Additionally, it has been demonstrated that the Seebeck coefficient of molecular junctions can be enhanced by manipulating intermolecular interactions of C₆₀ molecules placed in series between two gold electrodes [75]. This effect arises from the quantum mechanical origin of the Seebeck coefficient at the molecular scale. Indeed, at a qualitative level, if the transmission probability of electrons with energy passing from one electrode to another through a C₆₀ molecule is $T_1(E)$, the transmission probability through two C₆₀ molecules placed in series is approximately proportional to $T_1^2(E)$. Consequently, the conductance of two molecules placed in series G_2 is equal to G_1^2 , whereas Ohm's law predicts $G_2 = G_1/2$. Similarly, the Mott formula $S \propto \left. \frac{-\partial \ln T(E)}{\partial E} \right|_{E=E_F}$ predicts that the thermopower coefficients are related by $S_2 \propto 2 \times S_1$, whereas classically S_2 should be the same with S_1 . The aim of the chapter is to determine if similar non-classical behavior occurs when molecules are placed in parallel between two electrodes as in the concept device shown in Fig. 3.1 (a). If two such molecules in parallel behave classically, then the electrical conductance doubles according to Ohm's law and the Seebeck coefficient is unchanged. Consequently, if many molecules are placed in parallel to form a self-assembled monolayer (SAM), then the electrical conductance would be proportional to the number of molecules and the Seebeck coefficient would be insensitive to the number of parallel molecules bridging the junction. Reuter and co-workers have addressed how the electrical conductance of two molecules placed in parallel between two electrodes need not be $2G_1$, and have proposed that deviations from Ohm's law are a signature of direct intermolecular interactions or "cooperativity" [82].

In what follows, our aim is to examine this expectation from a microscopic point of view by computing the change in thermoelectric properties when two C₆₀ molecules are placed in parallel between two graphene electrodes. The results demonstrate that even when there is no direct inter-molecular coupling, indirect inter-molecular interactions mediated by the graphene electrodes produce quantum interference effects in the electronic structure of the molecular junction. As a consequence, the Seebeck coefficient is sensitive to the number N of parallel molecules and the electrical conductance is not simply proportional to N . These indirect interactions, if controlled properly can boost the electrical and thermoelectric performance of a device over the single-molecule paradigm.

3.2 Results and discussion

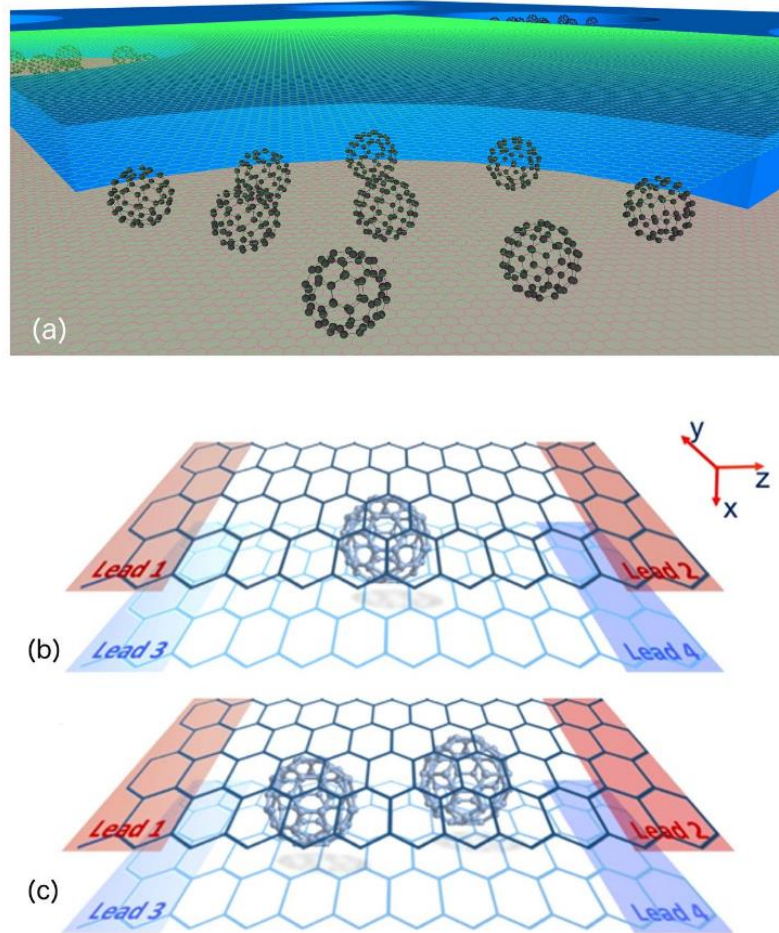


Fig. 3.1 (a) Vertical scalable concept for molecular thermoelectricity. An insulating spacer is placed on top of a graphene bottom electrode, and drilled with nanopores. These pores are filled with C₆₀ molecules. A top graphene electrode is deposited. Thermoelectricity is enhanced by quantum interference. Schematics of the two simulated four-terminal devices: (b) a C₆₀ monomer and (c) a C₆₀ dimer sandwiched between two graphene monolayers.

We have designed the vertical four-terminal devices shown in Fig. 3.1(b) and (c), where a single C₆₀ and a C₆₀ dimer are sandwiched between two horizontal graphene sheets, respectively. These two graphene sheets are separated by an

optimized vertical (z) distance and are electronically decoupled, except via the transport path through the buckyball(s) from the top to the lower sheet. The structure is assigned periodic boundary conditions in the x and y directions to avoid spurious edge effects. Furthermore, to eliminate edge effects in the z direction, the four regions (labelled leads 1–4) are semi-infinite crystalline leads, which channel electrons to and from reservoirs placed at infinity. In the case of the C60-dimer, the horizontal distance between the nearest atoms of the two C60s is initially set to 6 Å to avoid direct coupling between the buckyballs. We have used the DFT code SIESTA[83] to obtain the optimized geometry adopting the local density approximation and the Ceperley-Alder functional for exchange and correlation. We have also chosen a double- z plus polarization (DZP) basis set. After relaxing this structure, this distance is changed by only a fraction of an Å. In this situation, examination of the pseudo-atomic-orbital-based Hamiltonian describing the molecules confirms that there is no direct interaction between the two C_{60} molecules. We have extracted the resulting mean-field Hamiltonian and overlap matrices and used them to compute the electrical and thermoelectric properties of the devices with our transport code GOLLUM[84]. The transmission coefficient for electrons of energy E travelling from lead i to lead j is calculated through the standard expression[30].

$$T(E) = Tr[\Gamma_R(E)G^R(E)\Gamma_L(E)G^{R\dagger}(E)] \quad 3.1$$

where $\Gamma_{L,R}(E) = i(\Sigma_{L,R}(E) - \Sigma_{L,R}^\dagger(E))/2$ indicate the coupling between left and right electrodes and the extended molecule; $\Sigma_{L,R}(E)$ represent the self-energies;

and G^R the retarded Green's function. The thermoelectric coefficients including the electrical conductance $G(T)$, the thermopower $S(T)$, the contribution of electrons to the thermal conductance $\kappa_e(T)$ and to the figure of merit $ZT_e(T)$ can be written as follows [30][31]:

$$G(T) = G_0 L_0 \quad 3.2$$

$$S(T) = -\frac{L_1}{eTL_0} \quad 3.3$$

$$\kappa_e(T) = -2\frac{L_0L_2 - L_1^2}{hTL_0} \quad 3.4$$

$$ZT_e(T) = \frac{L_1^2}{L_0L_2 - L_1^2} \quad 3.5$$

in terms of the Lorenz numbers

$$L_n(T) = \int_{-\infty}^{+\infty} dE (E - E_F)^n T(E) \left(-\frac{df(E)}{dE}\right) \quad 3.6$$

where $G_0 = 2e^2/h$ is the conductance quantum, h is Planck's constant, e is the absolute value of electron's charge, $T = (T_i + T_j)/2$ is the mean temperature of electrodes i and j , f is the Fermi-Dirac distribution function and μ is the chemical potential of the device at equilibrium, e.g.: when all leads voltages are set to zero. The specific implementation is explained in detail in the reference article of the GOLLUM code [84].

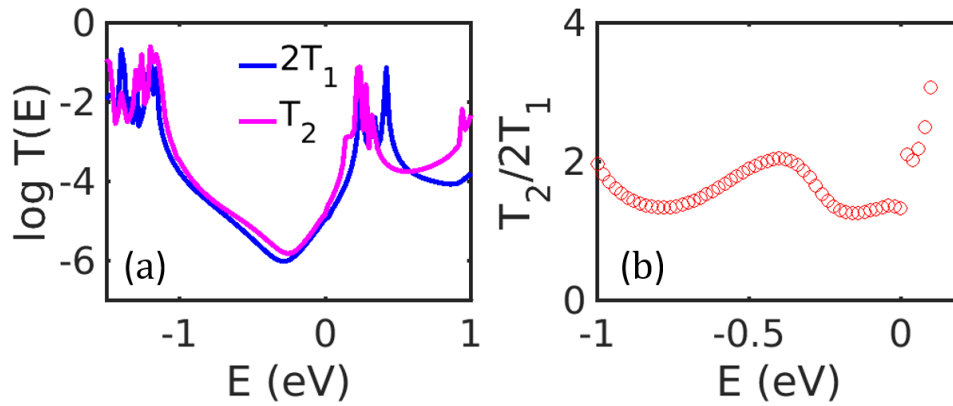


Fig. 3.2 (a) Transmission coefficient of the electrons passing from electrode 1 to electrode 4. The blue and pink curves present the transmission spectra $T_1(E)$ and $T_2(E)$ of the C_{60} -monomer and dimer devices, respectively. **(b)** The ratio of the two transmission coefficients shown in (a).

The transmission functions $T_{1,2}(E)$ for electrons of energy E passing from the top-left electrode (lead 1) to the bottom-right electrode (lead 4) are shown in Fig. 3.1 for the C_{60} -monomer and -dimer devices. As expected, due to the periodic boundary conditions chosen for the electrodes, the number of open channels for both devices is 2 in the energy range between -1.5 and $+1.5$ eV around the Fermi energy E_F . The energy position of the HOMO- and LUMO-mediated (highest-occupied and lowest unoccupied molecular orbital, respectively) resonances does not depend on the relative position and orientation of the molecule and the graphene electrodes for van der Waals chemical bonding[85]. We therefore predict that $T_{1,2}(E)$ should remain qualitatively the same as the C_{60} molecules move around and rotate. Furthermore, a close match between graphene's Fermi energy and the C_{60} HOMO or LUMO resonances is predicted since both are carbon-based materials [8]. We find that the LUMO resonances are much closer to the

Fermi energy than the HOMO-mediated ones for the vertical junctions shown in Fig. 3.2(a) result consistent with previous studies [86][17][87]. Furthermore, the conductance gap (e.g. the gap between the HOMO and LUMO resonances) for the dimer device shrinks due to the splitting of the degenerate HOMOs and LUMOs, a quantum interference effect caused by their indirect coupling mediated by the electrodes. In order to estimate the departure from Ohm's law caused by this indirect inter-molecular interaction, we show the ratio $T_2/(2T_1)$ over an energy range within the conductance gap in the plot in Fig. 3.2(b). This ratio is approximately 1.5 in the energy range between -0.8 eV and 0 eV and then increases quickly above the Fermi energy when approaching the LUMO resonance. This increase above unity breaks Ohm's law and is a consequence of the quantum interference effect that modifies the conductance gap. Indirect inter-molecular coupling not only changes the conductance ratios, but also affects the slope of the logarithm of the transmission coefficients. At low-enough temperatures, the Seebeck coefficient can be obtained using Mott formula [72]

$$S = -\frac{\pi^2}{3} \frac{k_B^2 T}{|e|} \partial_E \ln T(E) |_{E=E_F} \quad 3.7$$

Consequently, the Seebeck coefficient is proportional to the slope of natural logarithm of transmission function at the Fermi level and since these slopes differ, the Seebeck coefficients of the monomer and dimer junctions are different.

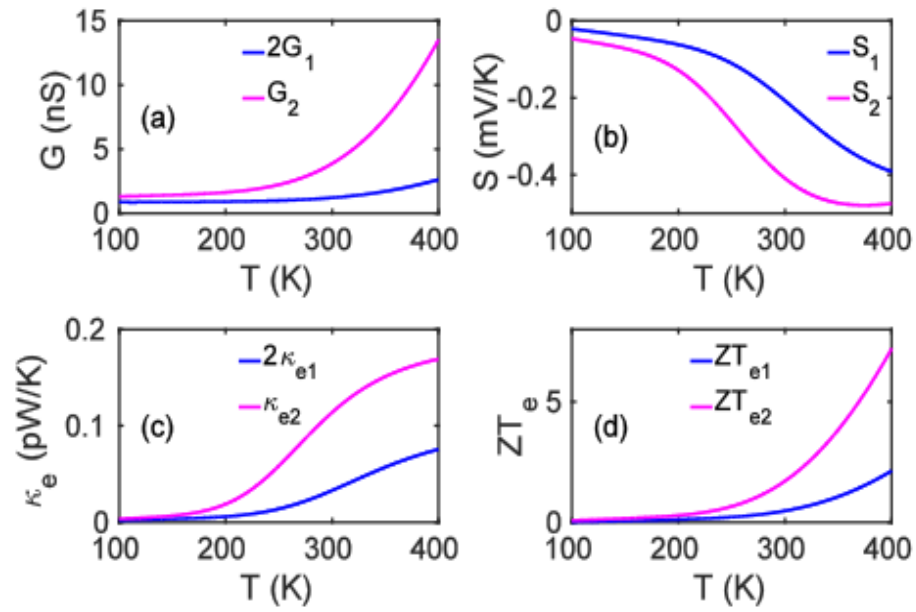


Fig. 3.3 Temperature evolution of thermoelectric coefficients. (a) Electrical conductance $G(T)$. (b) Seebeck coefficients $S(T)$. (c), (d) electronic contribution to thermal conductance $\kappa_e(T)$ and thermoelectric figure of merit ZT_e . The pink and blue curves correspond to dimer and monomer respectively.

Fig. 3.3 demonstrates that G , S , the electronic contribution to the thermal conductance κ_e and the electronic contribution to the thermoelectric figure of merit $ZT_e = S^2GT/k_e$ behave non-classically over a wide range of temperatures. Fig. 3.3(a) shows that the electrical conductance of the dimer system (pink curve) is more than twice that of the monomer (blue curve) over a wide temperature range. Fig. 3.3 (b) reveals that the Seebeck coefficient of the dimer junction is higher than that of the monomer junction. Fig. 3.3 (d) shows that although the electronic contribution to the thermal conductance (Fig. 3.3 (c)) of the dimer junction is higher than that of the monomer device, the higher electrical conductance and Seebeck coefficient of the dimer junction combine to deliver a higher electronic figure of merit.

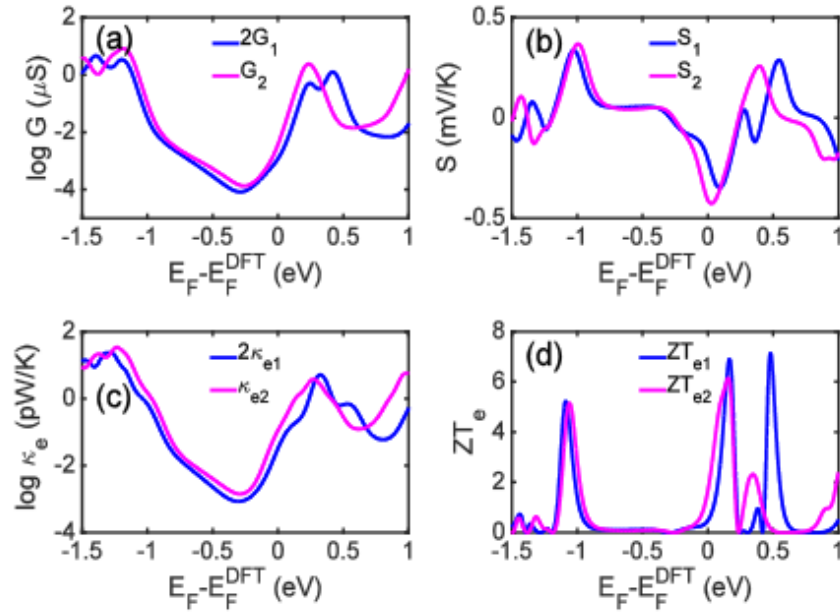


Fig. 3.4 Thermoelectric properties as a function of the Fermi energy at room temperature. (a) Electrical conductance G . (b) Seebeck coefficient S . (c) and (d) Electronic contribution to thermal conductance κ_e and thermoelectric figure of merit ZT_e .

Since the Fermi energy of the electrodes may be changed by doping or external gating, we analyze the quantum behavior of the thermoelectric properties of the junctions as a function of the Fermi energy at room temperature. Fig. 3.4 (a) and (c) demonstrate that both the electrical conductance and the electronic contribution to the thermal conductance of the dimer device are more than twice that of the monomer junction over an energy window around the Fermi energy. Fig. 3.4 (b) reveals that the dimer configuration also has a larger Seebeck coefficient than the monomer in the energy range between -0.2 and 0.1 eV and also from 0.3 to 0.5 eV. Fig. 3.4 (d) demonstrates that ZT_e is also larger in the vicinity of E_F .

In order to obtain further insight into this quantum interference effect, we have performed calculations of model tight-binding structures that share similar parallel electron pathways as the devices shown in Fig. 3.1. The schematics of those model structures is shown in Fig. 3.5. The red balls representing C_{60} molecules are sandwiched between the blue chains representing the graphene electrodes. There is no direct hopping between the two red sites in the two-site model as in the C_{60} dimer DFT calculation. Therefore, any departure from Ohm's law must be due to the indirect coupling between the two sites arising from quantum interference via the electrodes.

The transmission coefficients $T_{1,2}$ and the ratio $T_2/(2T_1)$ of these models are displayed in Fig. 3.6 (a). The pink curve shows that for the two-site model, the transmission resonance at energy $E = \epsilon$ is split in two due to the indirect coupling via the electrodes. The ratio $T_2/2T_1$, shown in Fig. 3.6 (b) varies from approximately 0.5 to 2.5 and converges at a constant around 2, which is twice the expected classical value of unity. Consequently, despite the simplicity of the tight binding, we find that it captures the mechanism underlying the quantum interference effects uncovered in the DFT-based analysis.

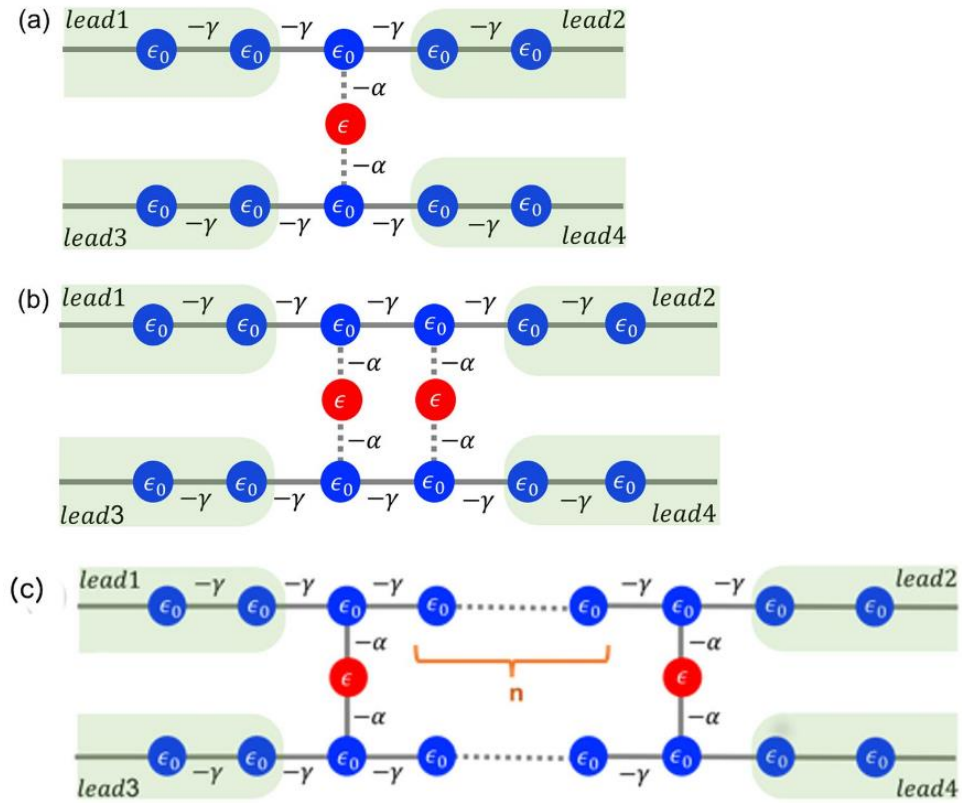


Fig. 3.5 Tight binding models having (a) one-atom pathway and (b) two-atom pathways. The chains represent the graphene electrodes, where blue dots correspond to carbon atoms. The red dots represent the C₆₀ molecules. To fix the energy scale, the hopping integral γ between blue sites is set to unity. The hopping integral α between red and blue site is set to 0.2. The hopping integral between red sites in (b) is set to zero. The on-site energy of both blue and red sites ϵ_0 and ϵ is set to 0.25. This reflects the relevant energy levels landscape found in the DFT calculation and displayed in Fig. 3.5. (c) A modified two-atom model where n represents the separation between red sites evaluated by the number of the blue sites lying in between.

We now discuss how this quantum interference behavior depends on the separation between the two sites. To do so, we modify the model shown in Fig. 3.5 (b) and displace the two red sites laterally so that there are n blue sites in between them as shown in Fig. 3.5(c). Fig. 3.6(b) shows the conductance ratio $G_2/(2G_1)$ at

three different temperatures (low, intermediate and high). We find that the ratio varies periodically with the distance n , and that it has an envelope that decreases with increasing n . We also find an even-odd quantum interference effect in the conductance ratio as a function of the parity of n . We therefore plot two curves for each temperature, one for even and another for odd n .

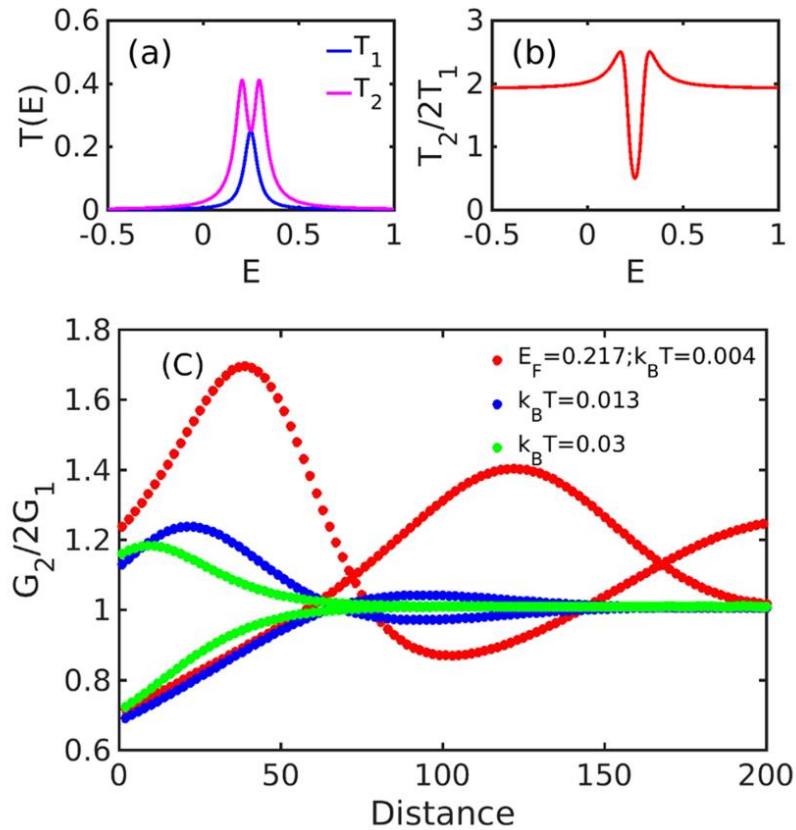


Fig. 3.6 (a) Transmission coefficients as a function of energy for the one-site and two-site models shown in Fig. 3.5. The blue line stands for one-site model while the pink is for the two-site model. (b) Ratio $T_2/2T_1$. (c) Conductance ratio $G_2/2G_1$ evaluated at $E_F = 0.217$ and different temperatures: $k_B T = 0.004, 0.13$ and 0.03 (red, blue and green curves). The two curves at each temperature show the conductance ratio for even and odd n .

The Figure also shows that this low-temperature oscillatory behavior is damped as the temperature increases. This damping is set by the temperature-dependent phase coherence length, and can be understood straightforwardly from the standard expression of the conductance $G = G_0 L_0$, where G_0 is the conductance quantum unit and the integral L_0 is defined in equation 3.6. The integration window for the integrals L_n covers an energy range of order $k_B T$ that is centered at the Fermi energy. Because the period of the oscillations in the transmission are energy-dependent and the different contributions to the integral dephase, the conductance oscillations die away at values of n beyond a certain dephasing length that is inversely proportional to the temperature, as illustrated in Fig. 3.6. Interestingly, in the absence of inelastic scattering, the asymptotic ratio $G_2/2G_1$ does not approach unity for large distances n , even though the oscillations disappear above a certain temperature. This is because the asymptotic ratio depends on the position of the Fermi energy relative to the quantum interference-split resonance shown in Fig. 3.6 (a). The above behavior is analogous to that of AlGaAs/GaAs quantum rings, where the temperature-dependent phase coherence length, extracted from Aharonov-Bohm magnetoresistance measurements, decreases as the temperature rises above 2.0 K [88]. The result also agrees well with that obtained by magneto-transport experiments combined with weak localization theory in MgZnO thin film [89], where the phase coherence length varies from 38.4 nm to 99.8 nm when temperature declines from 50 K to 1.4 K. If the model is extended to two-dimensional system where the one-dimensional leads is replaced by two-dimensional leads, the dephasing length is expected to decrease because of the quantum interference due to other conduction channels.

3.3 Conclusion

The electrical conductance G_2 of two parallel C₆₀ molecules sandwiched between two graphene monolayers does not follow Ohm's law, because it is more than twice larger than the conductance G_1 of a single C₆₀ molecule. This non-classical behaviour is due to indirect inter-molecular quantum interference effects mediated by the electrodes. Furthermore, increasing the number of C₆₀ molecules sandwiched in parallel between graphene monolayers from one to two also increases the Seebeck coefficient, which is another non-classical effect. This is significant because it demonstrates that single-molecule thermoelectric properties will not translate into thin-film materials formed from self-assembled monolayers in a classical manner and by exploiting quantum interference, the thermoelectric performance of such SAMs can exceed classical expectations. Further insight into this quantum interference effect is gained by analyzing a tight binding model that features parallel electron transport through two sites. The model predicts that the thermoelectric properties of the dimer will oscillate with the dimer separation n up to a phase coherence length, which decreases with increasing temperature.

4 A single-molecule porphyrin-based switch for graphene nanogaps

4.1 Introduction

Single-molecule electronic devices have been investigated intensively both experimentally[90][91][92][81][93][94][95] and theoretically [55][78][96][97][7][98], starting with the first molecular rectifier reported in 1974[99]. Since that time a variety of tuneable transport properties and active functionalities have been investigated, including molecular switches [100][101][102][103][104][40]. One example is the photo-switching operation of aryl azobenzene monolayer bridges between two vertical graphene sheets, whose conductance can be switched using optically-induced length changes of the molecule[105]. A second example involves redox based switching, in which a molecule based on anthraquinone with a cross-conjugated structure is in the “off” state, whereas it is in the “on” state when it is reduced to linear conjugation[101]. Another is based on conformational change, in which the conductance is tuned by decreasing the pi-pi orbital overlap within a bridging moiety by rotating adjacent phenyl rings[100][106]. Recently, in an effort to overcome the limitations of gold electrodes for contacting single molecules, graphene electroburnt

nanogaps[107][108][109][26][110][111] have been developed, which can be electrostatically tuned by a nearby buried gate electrode[112][6]. This opens the way to the design of new molecular switches, which take advantage of specific properties of such planar geometries.

In the present work, stimulated by the fact that conjugation can be broken by rotating two adjacent planar aromatic rings[100], we examine the possibility of single-molecule conductance switching when a single aromatic ring is rotated relative to the pi system of graphene electrodes. The target three-terminal device is shown in Fig. 4.1 and consists of a single porphyrin molecule placed in the nanogap between two graphene electrodes and simultaneously gated by a third electrode. When the porphyrin and graphene sheets are in the same plane, we expect the conductance to be high. When the plane of the porphyrin is perpendicular to the graphene plane, the conjugation will be broken and we expect the conductance to be low.

In the device of Fig. 4.1, the single porphyrin suspended in the graphene nano-gap contains pendant moieties, which create a dipole moment parallel to the plane of the porphyrin. The concept we aim to investigate is whether or not the porphyrin can be rotated by application of a modest electric field and whether or not this rotation creates a significant on-off ratio of the electrical conductance. In what follows, we demonstrate that there can be a huge difference in conductance between the zero-gate-voltage state and the device above a certain gate threshold value and therefore this combination of graphene electrodes and a porphyrin bridge is a promising design for a single-molecule switch. Crucially, it is possible

to enhance the switching behaviour by increasing the separation between the graphene electrodes and functionalised porphyrin molecule. We demonstrate that the room-temperature on-off conductance ratio can vary from 100 to 200 by increasing the number of C-C triple bonds from one to four, which act as spacers between porphyrin and graphene. We also demonstrate that the conductance ratio increases further from 200 to approximately 2200 by reducing the temperature to 100K.

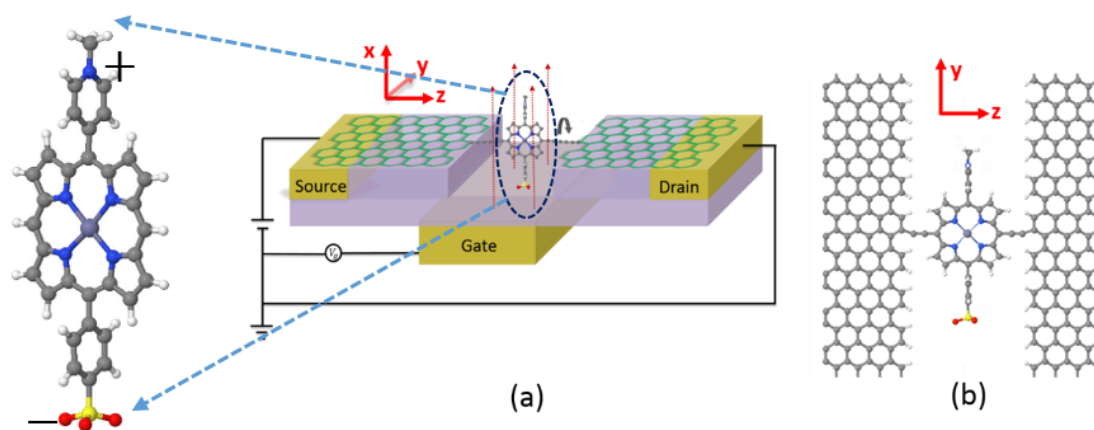


Fig. 4.1 (a) Three terminal concept for nanoscale switch with source and drain and gate electrodes. The functionalised porphyrin is shown on the left of the device. The red, yellow and blue atoms represent oxygen, sulphur and nitrogen respectively. The top moment group is positively charged while the bottom moment group is negatively charged. (b) Schematic of graphene/molecule/graphene device with one triple bond as spacer. Graphene is terminated by hydrogen (white atoms).

4.2 Results and discussion

Fig. 4.1 (b) shows a single porphyrin molecule functionalised with side groups which impart a dipole moment of 38.5 Debye in the y direction, parallel to the plane of the porphyrin core. The latter is connected to two electroburnt graphene sheets via acetylene linkers. The separation between the two planar graphene sheets is $d \approx 1.3$ nm and therefore they are electronically decoupled, except via the transport path through the porphyrin. Initially, as shown in Fig. 4.1, we consider only a single C-C triple bond spacer between each graphene electrode and the porphyrin. We used the DFT code SIESTA[83] to obtain the optimized geometry adopting the generalised gradient approximation (GGA) and PBE functional[113] for the exchange and correlation. We also chose a double- ζ plus polarized (DZP) basis set. Here, a large unit cell 50×51.12 in x, y direction shown in Fig. 1(a) is adopted to avoid the electrostatic interaction between the dipole moieties due to periodic boundary conditions. We then extracted the resulting mean-field Hamiltonian and overlap matrices and used them to compute the electrical properties of the devices with transport code Gollum[84]. The transmission coefficient $T(E)$ for electrons as a function of energy is calculated through the equations:

$$T(E) = Tr[\Gamma_L(E)G(E)\Gamma_R(E)G^\dagger(E)] \quad 4.1$$

Where $\Gamma_{L,R}(E)$ is the anti-Hermitian part of the self-energies: $\Gamma_{L,R}(E) = i(\Sigma_{L,R}(E) - \Sigma_{L,R}^\dagger(E))/2$. $\Gamma_{L,R}$ determines the width of transmission resonances, $\Sigma_{L,R}(E)$ are the

self-energies describing the contact between the molecule and left (L) and right (R) electrodes. while G is the retarded Green's function of the molecule in the presence of the electrodes. The thermally-averaged conductance $G(E_F, V)$ is evaluated using the following formulae:

$$P(\theta_i, V) = \frac{1}{A} e^{-U(\theta_i, V)/(k_B T)} \quad 4.2$$

$$A = \sum_{i=1}^{19} e^{-U(\theta_i, V)/(k_B T)} \quad 4.3$$

$$G = G_0 \int_{-\infty}^{+\infty} dE T(E) \left(-\frac{\partial f(E)}{\partial E} \right) \quad 4.4$$

$$G(E_F, V) = \sum_{i=1}^{19} G_i(E_F, \theta_i) P_i(\theta_i, V) \quad 4.5$$

$$I = \frac{2e}{h} \int_{-\infty}^{\infty} dE T(E) [f_l(E, E_F, T) - f_r(E, E_F, T)] \quad 4.6$$

where $G_0 = 2e^2/h$ is the conductance quantum; h is the Planck's constant; e is the charge of a proton; $f(E) = (1 + \exp(E - E_F/k_B T))^{-1}$ is the Fermi-Dirac probability distribution function, E_F is the Fermi energy and V indicates the gate voltage. In equation (5), the quantity $P(\theta, V)$ is the well-known Boltzmann distribution, which determines the statistical probability density that a system in thermodynamic equilibrium will be found to have energy $U(\theta, V)$ and hence a rotation angle θ .

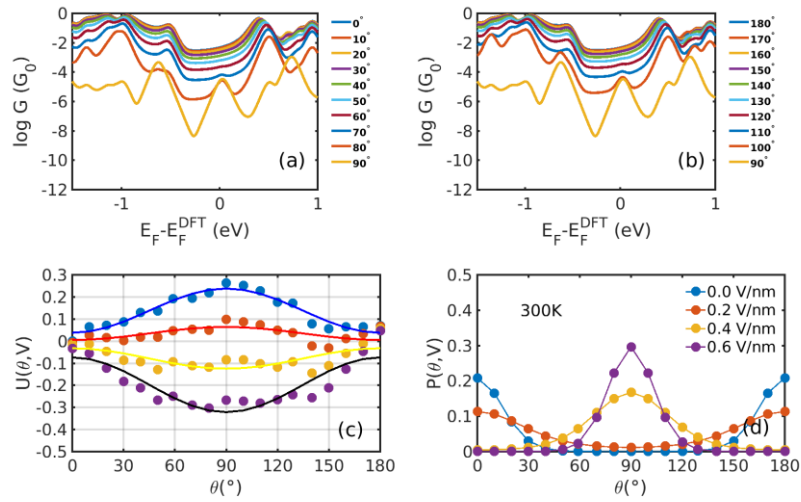


Fig. 4.2 Electrical conductances and energy landscapes of the device in Fig. 4.1, with one triple bond on each side. (a), (b) For a series of fixed values of θ , these figures show room-temperature electrical conductances (in units of $G_0=2e^2/h$) without a gate electric field as a function of the Fermi level E_F of the electrodes relative to the DFT-predicted value. (c) Potential energy versus θ for a series of perpendicular electric fields 0.0 V/nm (blue), 0.2 V/nm (red), 0.4 V/nm (yellow), 0.6 V/nm (purple). The dots represent the total energies relative to the energy at 0° and 0 V/nm calculated by DFT, which are fitted by $y = a \sin^2 \theta + b$. (d) The corresponding Boltzmann probability distribution (defined by equation (2) and (3)) against θ under different gate electric fields at 300K. The different structures corresponding to different rotating angles are not relaxed, because otherwise, upon relaxation, they would all relax back to the same minimum-energy angle.

To understand the change in conductance due to a rotation θ about the axis of the triple bonds, we first compute the room-temperature electrical conductance (see theoretical methods) when the porphyrin is frozen at a series of θ values between zero and 180° . Since the Fermi energy E_F of the electrodes relative to the HOMO and LUMO levels could be tuned by doping or external gating, in Fig. 4.2 (a) and Fig. 4.2 (b), we plot graphs of room temperature ‘frozen’ zero-bias conductance

$G(E_F, \theta)$ versus E_F for different values of θ . Fig. 4.2 (a) shows results for rotation angles θ between 0° and 90° , while Fig. 4.2 (b) shows results for θ between 90° and 180° . The transmission spectra from which these conductances are derived are shown in Fig. 4.3.

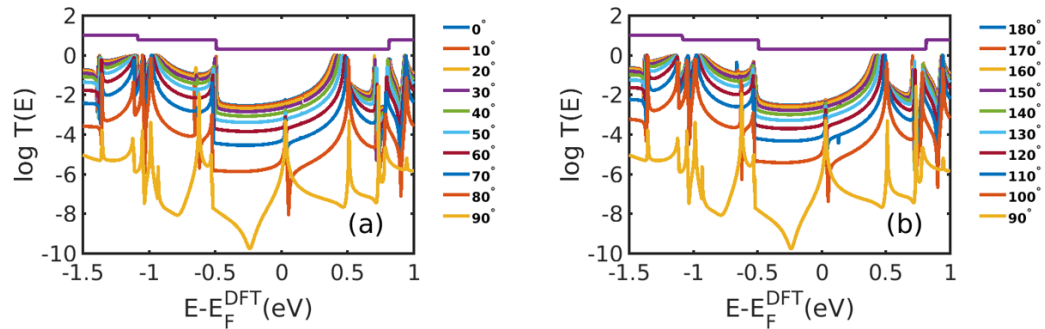


Fig. 4.3 Transmission spectra of different rotating configurations with one triple bond as the spacer on each side.

Results are plotted against $E_F - E_F^{DFT}$, where E_F^{DFT} , is the DFT-predicted Fermi energy. The junction in Fig. 4.1 (b) is not exactly symmetric about a perpendicular plane passing through the triple bonds, and therefore $G(E_F, 90^\circ - \theta)$ is almost, but not quite equal to $G(E_F, 90^\circ + \theta)$. This slight asymmetry is due to the different structures of the dipole moieties $-C_6H_4SO_3$, $-NC_5H_4CH_3$ and the slight asymmetric connection to the graphene, imposed by the armchair edge. Clearly there is a huge variation in $G(E_F, \theta)$ as θ varies between 0° and 90° . Fig. 4.2 (a, b) show that there are two main resonances at -1eV and 0.5eV for all angles except 90° , where the conjugation between the pi system of porphyrin and the pi orbitals of graphene is broken. This broken conjugation at 90° leads to a low conductance over a range of Fermi energies in the vicinity of E_F^{DFT} . In order to gain insight into

the origin of these resonances, Fig. 4.6 (left column) shows the local density of states (LDOS) in the vicinity of E_F^{DFT} , which is concentrated on the pendant moieties, whereas the right column shows that the LDOS at the transport resonance around 0.3 - 0.5eV, which is more delocalised across the backbone of the molecule. Similarly, the LDOS at -0.7eV resonance is dominated by the pendant group, while that at -1eV resonance is delocalised on the porphyrin core. The positions of the 'delocalised' resonances near 0.3 - 0.5eV and -1eV correspond to the LUMO and HOMO of the pure porphyrin molecule sandwiched in graphene nano-gap shown in Fig. 4.4, whose molecular orbitals are plotted in Fig. 4.5.

Fig. 4.2 (a) and Fig. 4.2 (b) shows the conductance when a rotation angle θ is artificially imposed. In practice, the junction is controlled by imposing an external gate voltage V and at a finite temperature T , the rotation angle will fluctuate thermally. The probability of finding a given angle θ will be proportional to the Boltzmann factor $e^{-U(\theta,V)/(k_B T)}$, where $U(\theta,V)$ is the change in energy of the junction as a function of θ and V [114]. Fig. 4.2 (c) shows the change of total energy $U(\theta,V)$ versus rotation angle θ with a series of gate voltages V . The dots in blue, red, yellow and purple correspond to energy changes under perpendicular electric fields 0 V/nm, 0.2 V/nm, 0.4 V/nm, 0.6 V/nm obtained from DFT calculation. These dots are fitted to the function $y = a * \sin^2 \theta + b$ presented in solid lines, where b is an irrelevant constant, which disappears after normalising the Boltzmann weights. The blue line shows that in the absence of a gate field, the energy minimum occurs at $\theta = 0^\circ$ and the maximum appears at 90° . On the other hand, the purple line shows that as the gate electric field increases, the energy minimum eventually switches from 0° to 90° . To compute each of the conductance curves of Fig. 4.2 (a)

and Fig. 4.2 (b), the rotation angle is constrained at a particular value of θ and the conductance calculated using Eq. 4.4 To determine the value of θ adopted by the switch at a given gate voltage V , the total energy $U(\theta, V)$ was computed for a series of angles θ and plotted in Fig. 4.2 (c). At absolute zero and at a given gate voltage V , the switch would adopt the angle corresponding to the minimum of $U(\theta, V)$. However, at finite temperatures, the switch is subject to thermal fluctuations and will sample all angles. The probability distribution $P(\theta, V)$ that at a particular instant, the switch will assume an angle θ is given by the Boltzmann distribution of Eq. 4.2 For the single triple bond and different values of V , the room-temperature probability distributions are plotted in Fig. 4.2 (d) and show that those angles corresponding to minima in $U(\theta, V)$ are sampled with the highest probability.

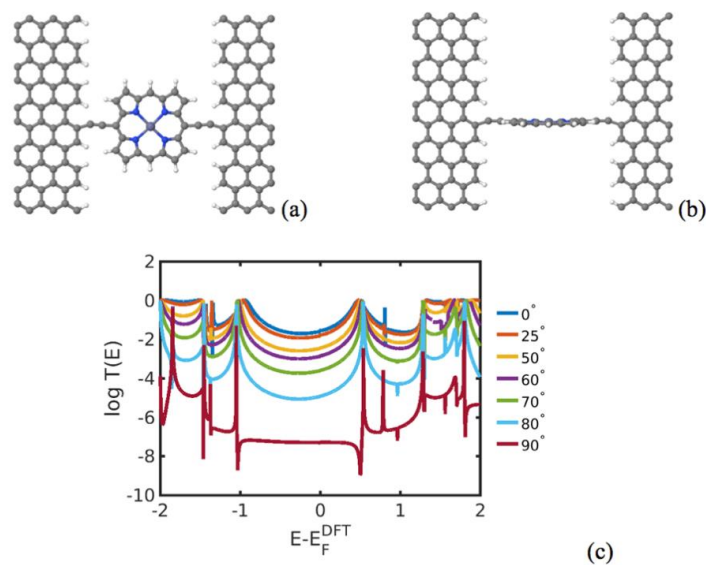


Fig. 4.4 The transmission spectra for Zn-porphyrin molecule without functionalized dipole group bridging the two graphene sheets from 0 (shown in (a)) torsion angle to 90 (shown in (b)) between the molecule and graphene plane.

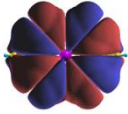
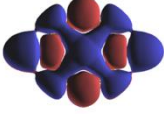
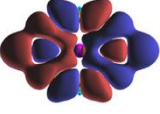
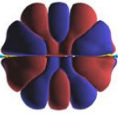
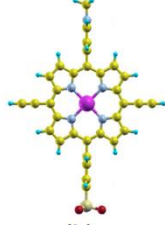
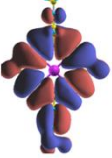
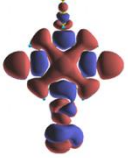
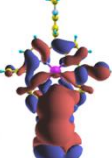
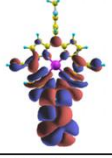
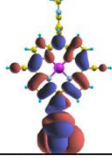
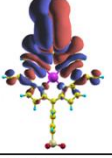
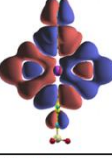
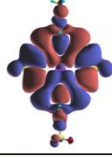
1	 (a)					
2	$E_F = -3.970\text{eV}$	-5.009eV HOMO-1	-4.753eV HOMO	-3.080eV LUMO	2.847eV LUMO+1	
3	 (b)					
4		-5.24 HOMO-5	-5.005 HOMO-4	-4.945 isov=0.005 HOMO-3	-4.910 isov=0.0005 HOMO-2	
5						
6	$E_F = -3.976\text{eV}$	-4.593 isov=0.003 HOMO-1	-4.010 isov=0.0005 HOMO	-3.943 LUMO	-3.381 LUMO+1	-3.162 LUMO+2

Fig. 4.5 The wave functions for (a)Zn-porphyrin with one triple bond each side and (b)functionalised Zn-porphyrin. The 1st and 2nd show the four frontier molecular orbitals for molecule (a). The 3rd ~6th depict the frontier molecular orbitals for molecule (b).

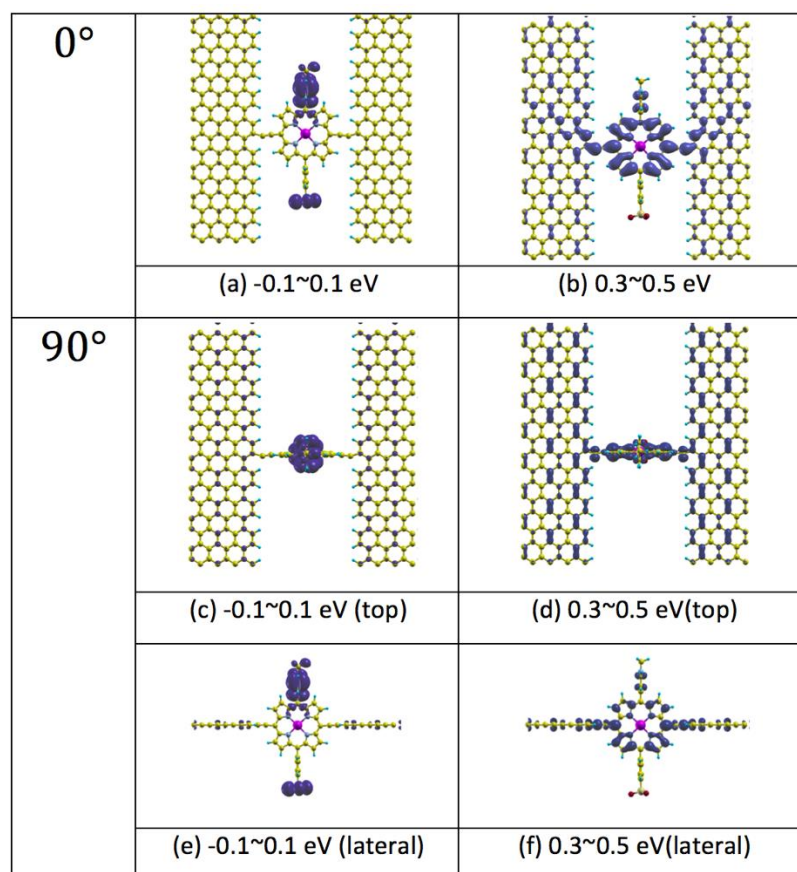


Fig. 4.6 Local density of states (LDOS) of the junctions at 0° and 90° rotation angles. (a), (b) show the LDOS in the energy windows $-0.1\sim 0.1\text{eV}$ and $0.3\sim 0.5\text{eV}$ separately for 0° . (c), (d) are for 90° . (e), (f) are the lateral views for 90° . The energy windows refer to the DFT Fermi level in Fig. 4.2 (a) and Fig. 4.2 (b). Here, yellow atoms depict carbon atoms and light blue depict hydrogen atoms. The LDOS is calculated by integrating the imaginary part of the Green's function $G(\mathbf{r}, E)$ with respect to energy E over a small energy window, centred of a particular energy. In Fig. 4.6, results for two energy windows are presented, namely -0.1eV to 0.1eV and 0.3eV to 0.5eV . The orbitals within the first energy window are mainly located in the pendant groups, while the orbitals within the second energy window are localised on the porphyrin backbone.

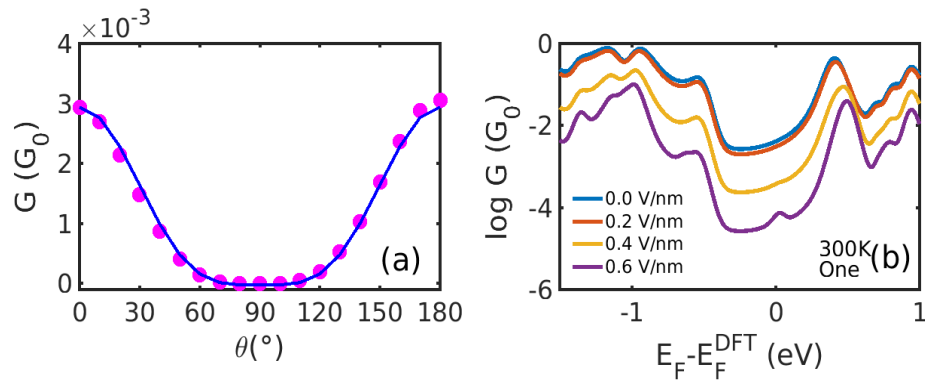


Fig. 4.7 (a) Conductance versus the rotation angle derived from Fig. 4.2 (a) and 2(b) at $(E_F - E_F^{\text{DFT}} = -0.25 \text{ eV}$ and electric field is 0 eV .) The pink dots are obtained from the DFT calculation and the blue solid line is the fitting curve by $y = a * \cos^4 \theta + b$. **(b) Boltzmann-averaged conductances versus Fermi energy calculated using equation (5) by averaging over the curves in Fig. 4.2 (a), Fig. 4.2 (b), using the probability distributions in Fig. 4.2 d).**

Fig. 4.7 (a) shows the $\cos^4 \theta$ relationship between the conductance and the rotation angle. Here, the Fermi level is chosen to be $E_F - E_F^{\text{DFT}} = -0.25 \text{ eV}$, which is close to the middle of the HOMO-LUMO gap. The $\cos^4 \theta$ dependence arises, because the coupling to both the left and right graphene electrodes is proportional to $\cos^2 \theta$ and the total conductance through the whole junction is proportional to the product of these couplings [8][115][116][117].

Fig. 4.7 (b) illustrates the Boltzmann-averaged conductances obtained from Eq. 4.5 for the series of perpendicular electric fields shown in Fig. 4.2 (d). Specifically, the 4 average conductance curves shown in Fig. 4.7 (b) are obtained based on the conductance curves in Fig. 4.2 (a) and Fig. 4.2 (b) of the 19 rotation angles and the distribution curves of the 4 electric fields in Fig. 4.2 (d) according to Eq. 4.5. This

shows that for a wide range of Fermi energies within the HOMO-LUMO gap (more precisely, $-0.4 \sim 0.4 \text{ eV}$), the conductance decreases approximately by two orders of magnitude due to the switching on of a 0.6 V/nm electric field and therefore this porphyrin-graphene device is a potential switch. On the other hand, an on-off conductance ratio of 100 (one specific value at a Fermi energy $E_F - E_F^{\text{DFT}} = -0.25 \text{ eV}$) in comparison with the gate electric field of 0 and 0.6 V/nm is not quite sufficient to be of technical interest and therefore we now demonstrate that this ratio can be improved by increasing the number of triple bonds connecting the porphyrin core to the graphene.

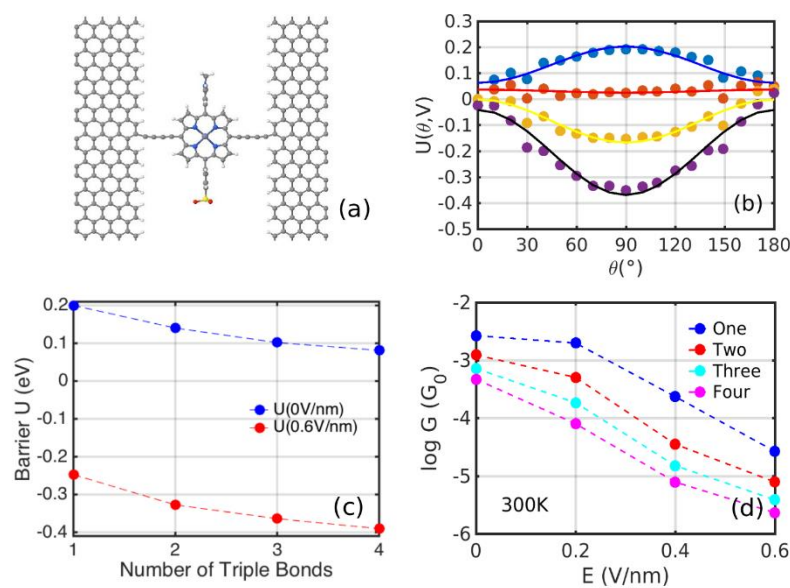


Fig. 4.8 (a) Geometry of the switch with two carbon-carbon triple bonds on each side. (b) Potential landscape under different perpendicular electric fields (0.0 V/nm (blue), 0.2 V/nm (red), 0.4 V/nm (yellow), 0.6 V/nm (purple) from top to bottom). Similar plotting to Fig. 4.2 (c). (c) Potential barrier extracted from the fitting curve as the function of the number of triple bonds on each contact. The blue one represents the energy barrier without gate while the red shows the potential well

under 0.6 V/nm. (d) Zero-bias, room-temperature conductance versus the external perpendicular electric field. The blue, red, cyan and pink are for one, two, three and four triple bonds structure. Here, the Fermi level is chosen to be near the centre of the HOMO-LUMO gap, at $E_F - E_F^{\text{DFT}} = -0.25$ eV.

Fig. 4.8 (a) shows a sketch of the device with two C-C triple bonds connecting the porphyrin to the graphene and Fig. 4.8 (b) shows the corresponding energy landscape for four values of the perpendicular electric field ranging from 0.0 V/nm to 0.6 V/nm. This series of calculations was repeated for junctions with three and four triple bonds connecting the porphyrin to each graphene electrode and in each case, a fit to the formula $U(\theta, V) = a \sin^2 \theta + b$ was carried out. The energy landscapes for the structures with three and four triple bonds on each side are shown in Fig. 4.9 and Fig. 4.10.

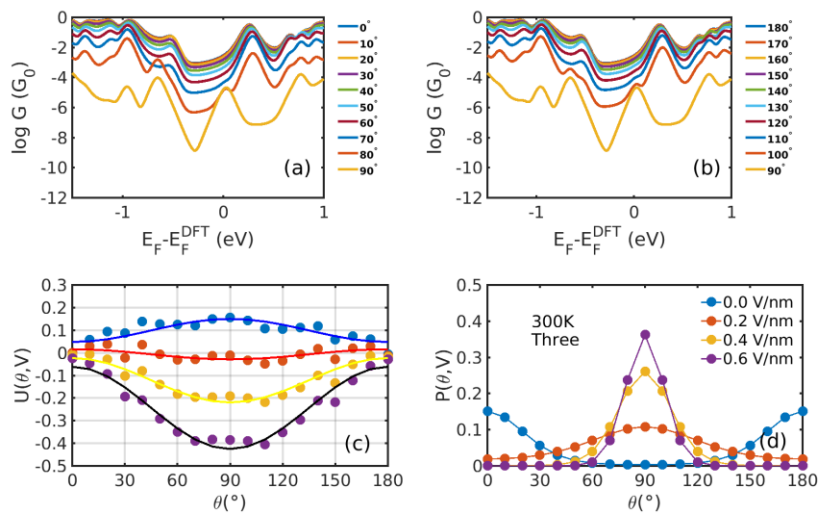


Fig. 4.9 (a), (b) Electrical conductance in units of the conductance quantum $G_0=2e^2/h$ without gate electric field as a function of the Fermi level E_F of the electrodes relative to the DFT-predicted value in zero bias limitation at 300K. (c) Potential landscape under a series of perpendicular electric field 0.0 V/nm (blue),

0.2 V/nm (red), 0.4 V/nm (yellow), 0.6 V/nm (purple) shown in (d). The dots represent the total energies relative to the energy at 0° and 0 V/nm calculated by DFT which are fitted by $y = a \sin^2 \theta + b$. (d) Corresponding Boltzmann distribution probability (obtained by formula (2), (3)) against the rotation of porphyrin under different gate electric fields at 300K. ‘Three’ indicates 3 triple bonds between the molecule and each electrode.

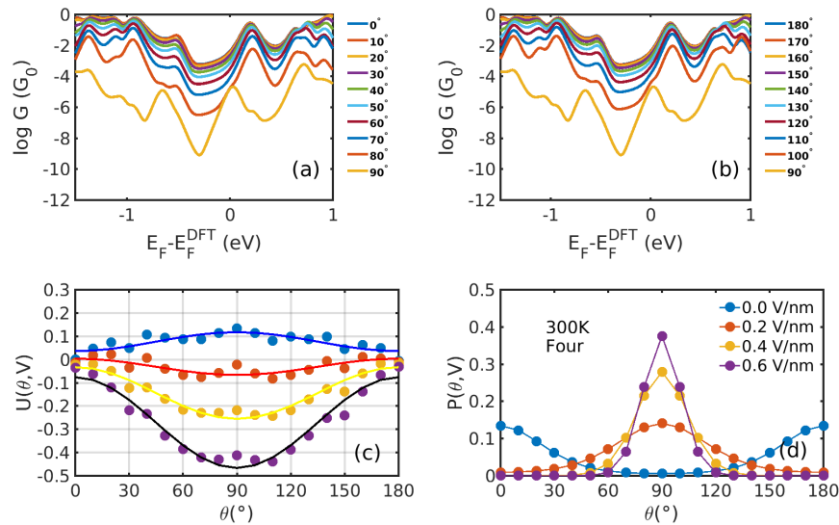


Fig. 4.10 (a), (b) Electrical conductance in units of the conductance quantum $G_0=2e^2/h$ without gate electric field as a function of the Fermi level E_F of the electrodes relative to the DFT-predicted value in zero bias limitation at 300K. (c) Potential landscape under a series of perpendicular electric field 0.0 V/nm (blue), 0.2 V/nm (red), 0.4 V/nm (yellow), 0.6 V/nm (purple) shown in (d). The dots represent the total energies relative to the energy at 0° and 0 V/nm calculated by DFT which are fitted by $y = a \sin^2 \theta + b$. (d) Corresponding Boltzmann distribution probability (obtained by formula (2), (3)) against the rotation of porphyrin under different gate electric fields at 300K. ‘Four’ indicates 4 triple bonds between the molecule and each electrode.

Fig. 4.8 (c) shows plots of the barrier heights a when the perpendicular electric field is either zero (blue) or 0.6 V/nm (red). For the former, a is positive,

corresponding to a maximum at $\theta = 90^\circ$, and the barrier decreases with the number of triple bonds. For the latter, a is negative, corresponding to a minimum at $\theta = 90^\circ$ and the energy barrier increases with the number of triple bonds. In the absence of a gate voltage, this varies from about 0.2eV for the single triple bond linker, to 0.09eV for the 4-triple bond linker. For comparison, $k_B T$ at room temperature is 0.025eV. In the presence of a 0.6 V/nm gate field, these increase from about 0.25eV for the single triple bond linker, to 0.39eV for the 4-triple bond linker. Since these are an order of magnitude greater than room temperature, switching is significant. Of course mathematically, for a large enough number of triple bonds, this trend should reverse and the energy barrier would tend to zero. However, in practice, the number of triple bonds is restricted by limits of synthetic chemistry, and therefore Fig. 4.8 (c) suggests that this limit is not readily accessible.

Fig. 4.8 (d) shows the Boltzmann-averaged conductances obtained at a Fermi energy $E_F - E_F^{\text{DFT}} = -0.25$ eV near the middle of the HOMO-LUMO gap. As expected, the conductances decrease as the number of triple bonds increases, because transport takes place via phase-coherent tunneling[118]. Furthermore, all conductances decrease with increasing electric field, because the most probable rotation angle switches from $\theta = 0^\circ$ at low fields to $\theta = 90^\circ$ at high fields. Fig. 4.8 (d) shows that when the gate field 0.6 V/nm is imposed, the room-temperature conductance decreases by a factor of 100 for one triple bond, approximately 150 for two triple bonds, 185 for three, and 200 for four triple bonds (pink curve). This demonstrates that the on-off ratio can be increased significantly by increasing length of the linkers between the porphyrin core and the electrodes.

Of course, as the length of the linkers increases, the synthetic chemistry becomes more challenging and therefore to further increase the on-off ratio, we considered the effect of reducing the temperature. As shown in Fig. 4.11, reducing the temperature from 300K to 100K increases the on-off ratio from 100 to 1000 for one triple bond structure using the same electric field. This increase occurs, because in the presence of a 0.6 V/nm gate field, thermal fluctuations about the energy minimum are suppressed and therefore only low-conductances near at $\theta = 90^\circ$ are sampled.

Fig. 4.11 (a) shows the on/off ratio evolution as the function of temperature. At infinite temperature, the on/off ratio would be, because all rotation angles would be sampled with equal probability, independent of the energy landscape. Fig. 4.11 (b) shows the on/off ratio at room temperature, which increases from 100 to 200 when the number of triple bonds increases to four. Furthermore, from Fig. 4.11 (a), at 100K, the corresponding increase is from 1000 to 2200.

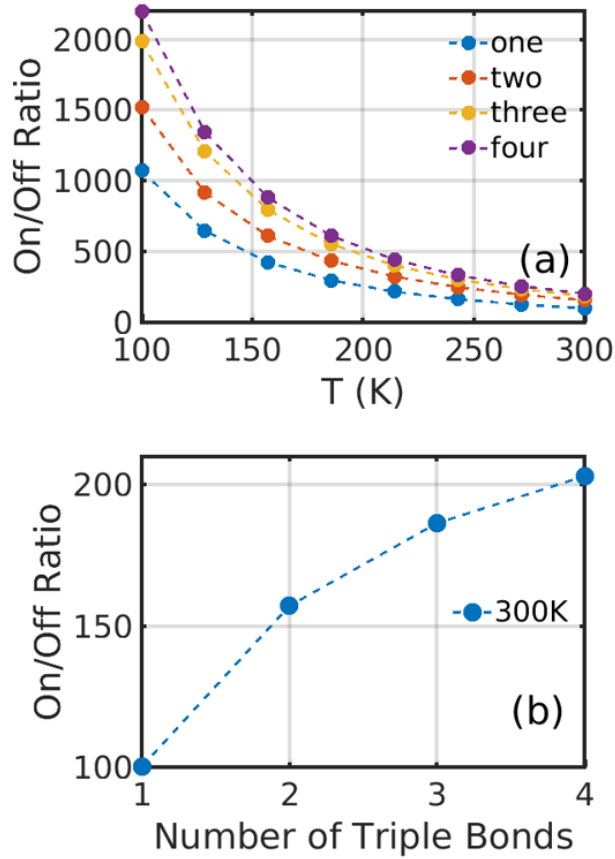


Fig. 4.11 (a) On/Off ratio evolution versus temperature T . The blue, orange, yellow and purple are for one-triple bond, two triple bonds, three triple bonds and four triple bonds structure, respectively. Here one, two, three, four mean the number of triple bonds on each contact between electrode and molecule. (b) On/Off ratio evolution versus the number of triple bonds on each side. As an example, the on-off ratio of 100 for a single triple bond is obtained from Fig. 4.7(b) by comparing the conductance at one specific Fermi energy for gate voltage of 0 with the corresponding value at a gate voltage of 0.6V/nm. In practice, the precise Fermi energy depends on the doping of the graphene, which in most experiments is hole doped. Therefore, the selected Fermi energy was chosen to be $E_F - E_F^{DFT} = -0.25$ eV relative to the pristine value.

Further, the currents under finite biases are calculated and shown in the following plots. Transmission spectra of the four devices with one, two, three, four triple

bonds are presented in Fig. 4.12 (a). Fig. 4.12 (b) show the currents corresponding to each rotation angle under finite bias obtained by Landauer formula shown in Eq. 4.6. Fig. 4.12 (c)s depict the Boltzmann-averaged currents under different gates on the basis of the current shown in Fig. 4.12 (b). We can see the current increases linearly as the bias arises in a reasonable range. The corresponding On-Off ratios extracted from Fig. 4.12 (c) are presented in Fig. 4.12 (d). Fig. 4.13 presents the On-Off ratios of the four devices under three finite biases ($V_b=0.1\text{eV}$, 0.2eV , 0.3eV) at room temperature. It is found that there is no big difference in the On-Off ratios under the three finite biases.

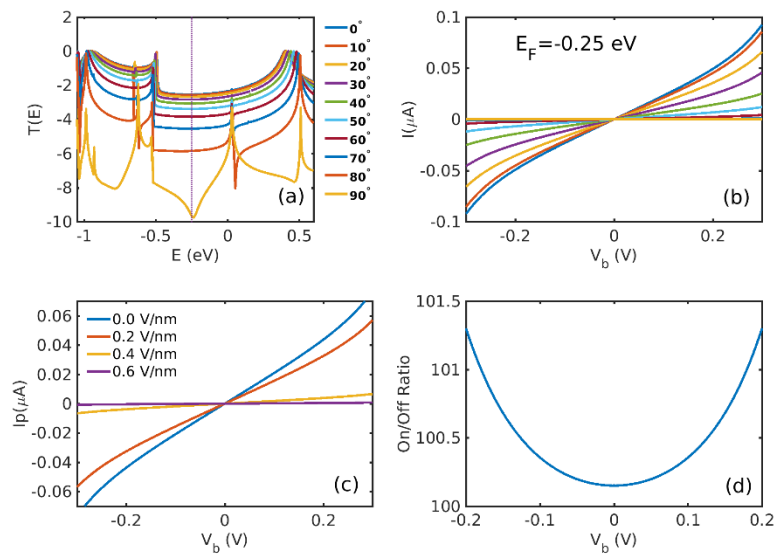


Fig. 4.12 Transmission spectra and I-V curves of the device with one triple bonds.

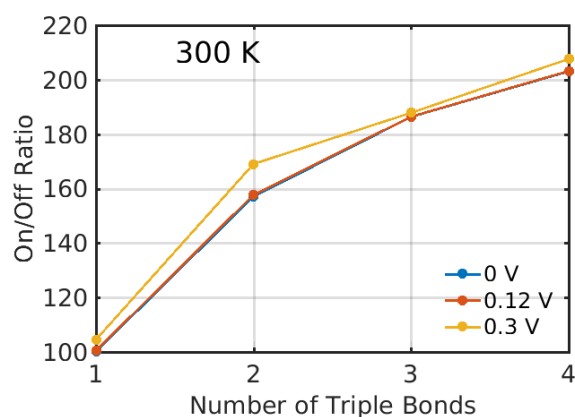


Fig. 4.13 On-Off ratio of four devices with one, two, three, four triple bonds under finite biases.

4.3 Conclusions

In summary, using density functional theory combined with Green's function scattering techniques, we have computed the electrical conductance versus gate voltage of a porphyrin molecule sandwiched between two electro-burnt graphene electrodes. The porphyrin is connected to each electrode by oligoyne spacers formed from one to four triple bonds. Due to the presence of pendant moieties, which create an electric dipole moment, the gate voltage rotates the pi system of the porphyrin relative to the pi system of the graphene. For a rotation angle $\theta = 0^\circ$, the pi systems are aligned and the conductance is high. For $\theta = 90^\circ$, the pi systems are orthogonal, the conjugation is broken and conductance is low. It is found that there exists a large conductance ratio between the on ($\theta = 90^\circ$) and off ($\theta = 0^\circ$) states, whose room-temperature value ranges from approximately 100 of one-triple-bond spacers to 200 for four-triple-bond spacers. This on-off ratio can be

further increased to 2200 by cooling the switch to 100K. The above strategies for increasing the on-off ratio could be applied to other molecules with a conjugated core, connected to graphene electrodes by oligoynes linkers. To date switches of the kind discussed in this paper have not been realised experimentally, but we are hopeful that our study will encourage progress in this direction. There are two possible junction-formation techniques, which could be used to create these switches. The first uses electroburning to produce graphene nanogaps of the required size[107][108][26], while the second uses ultrahigh-resolution electron-beam lithography and oxygen plasma ion etching[109].

5 Distinguishing Lead and Molecule States

5.1 Introduction

Graphene electrodes are advantageous for use in single-molecule devices,[26][112][119] because unlike metal electrodes, they do not suffer from high atomic mobility and screening. Large area single-layer graphene can be grown and patterned into electrodes separated by nanogaps,[120] and then molecules bridging the gap can be anchored to the electrodes via covalent bonding [109] or π - π -stacking[121][25]. However, the nontrivial density of states in graphene nanostructures, combined with the fact that graphene can be electrostatically gated, can lead to the transport features which are not intrinsic to the molecule under investigation, but are rather a property of the leads in graphene-based single-molecule devices. Experimental and theoretical studies have shown that quantum interference in graphene ribbons [122][123][124] and nano-constrictions [125] lead to conductance fluctuations at cryogenic temperatures. Quantum confinement in the source and drain electrodes of semiconductor single-electron transistors results in the observation of density of states oscillations in the sequential electron tunnelling transport through these

devices.[126] Therefore we expect that quantum interference effects in graphene electrodes will also influence the charge transport in single-molecule devices.

Here the experimental data by the collaborator presents a transport spectroscopy investigation of a graphene-based single-electron transistor where the sequential electron tunnelling is attributed to the presence of a single molecule bridging the graphene nanogap. Although the charge island is most likely formed by an individual zinc-porphyrin dimer, the observed transport features are completely independent of the type of molecule used, and in fact can also be observed in graphene quantum dots in a similar device geometry. Experimental data show how the graphene leads couple electrostatically to a global back-gate, and that hybridization between the lead and molecule states results in distinct fluctuation patterns as a function of gate and bias voltage. This behaviour is confirmed by our simple tight-binding model, which we deal with both analytically and numerically. Finally, a strategy is proposed to recover transport features that are intrinsic to the molecule, and might be obscured by the density of states fluctuations in the leads. Simultaneously, another tight-binding model considering the effect of magnetic field is designed and the features are in good agreement with the experimental data.

5.2 Results and discussion

5.2.1 The observation and simulation of Coulomb blockade

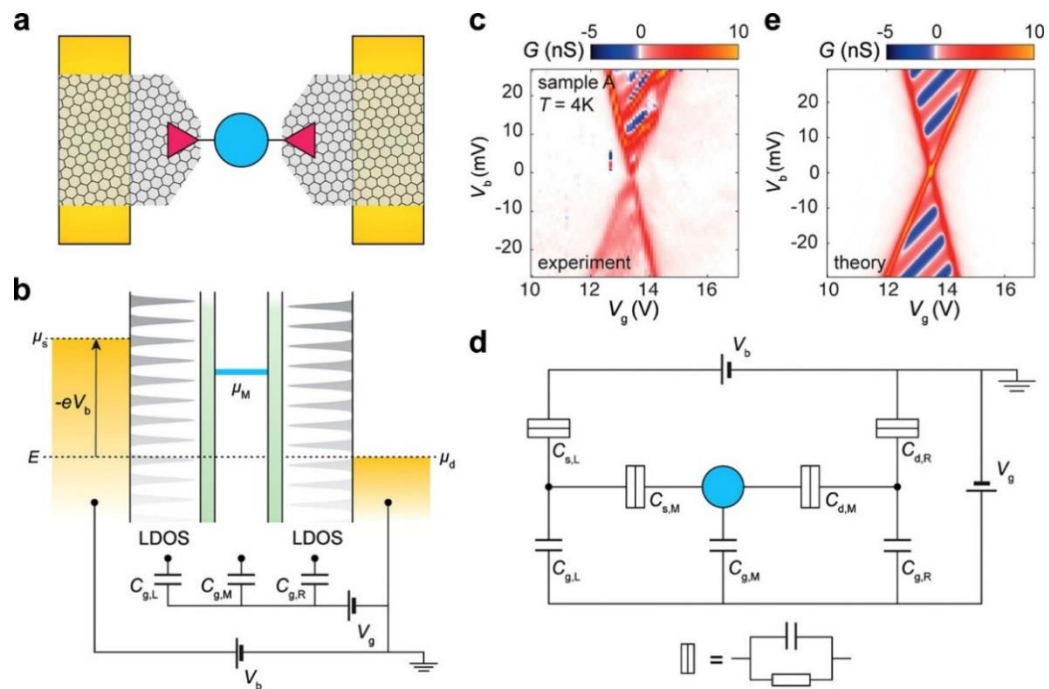


Fig. 5.1 Measurement and theory of a graphene-based single-electron transistor. (a) Schematic depiction of the device. Graphene electrodes are connected to gold reservoirs left and right; a single molecule bridges the gap between the graphene electrodes. (b) Schematic energy diagram of the graphene–molecule–graphene junction. (c) Measured differential conductance $G = dI/dV_b$ as a function of bias and gate voltage (sample A). (d) Equivalent circuit diagram of (a) and (b); the Ohmic approximation for a tunnel barrier is valid in the low bias regime of (c) and (e). (e) Calculated differential conductance as a function of bias and gate voltage.

The conductance through the single zinc-porphyrin dimers was investigated via single-electron tunnelling from a metallic source reservoir via the left graphene lead, through the molecule, to the metallic drain reservoir via the right graphene

lead shown in Fig. 5.1a. The silicon dioxide substrate was used as a backgate to apply V_g . In contrast with metal-based single-molecule transistors, where the metal electrodes screen the gate electric field, the electrostatic gating influences both the molecular orbital states and the states in the graphene leads (Fig. 5.1b). These fluctuations in the graphene leads influence the transmission through the molecule as orbital states are tuned in and out of resonance with the lead states. Fig. 5.1c shows the differential conductance measured as a function of the applied bias and gate voltage for sample A. The data reveal a dense set of positive and negative conduction resonances visible as red and blue lines of positive slope that we attribute to fluctuations in the graphene leads. A striking feature of the data is that the red and blue lines do not run parallel to the lines at the edges of white regions of suppressed conductance. In what follows, we will discuss the origin of the conduction resonances and analyse the electrostatic gating of the molecule and the lead states.

For charge to flow through a molecule, electrons need to be added and removed from it. The energy required to add one electron to the molecule, i.e., its electron affinity, is given by the electrochemical potential $\mu_M(N) = U(N) - U(N - 1)$, where $U(N)$ is the total energy of the N-electron redox state.[127] This electrochemical potential consists of the discrete orbital energy plus the electrostatic contribution to the energy, which depends linearly on the source (drain) $V_{s(d)}$ and gate V_g voltage as

$$\mu_M = -\frac{|e|(C_{s,M}V_s + C_{d,M}V_d + C_{g,M}V_g)}{C_{s,M} + C_{d,M} + C_{g,M}} \quad 5.1$$

where the capacitance $C_{s(d,g),M}$ describes the electrostatic interaction between the source (drain, gate) electrode and the molecule.[128] Electrons can tunnel through the molecule when its electrochemical potential is within the bias window defined by the electrochemical potentials $\mu_s = -|e|V_s$ and $\mu_d = -|e|V_d$ in the source and drain reservoirs, respectively. When μ_M is outside this bias window, electrons do not have the necessary energy to occupy/empty an orbital, resulting in diamond-shape regions of Coulomb blockade in the conductance versus bias and gate voltage map. The slopes of these Coulomb peaks (Fig. 5.3d) are given by the conditions

$$\mu_M = \mu_d; \mu_M = \mu_s \quad 5.2$$

When the device is biased asymmetrically, in our case, i.e., $V_s = V_b$ and $V_d = 0$, these conditions yield the slopes

$$b_1 = \frac{C_{g,M}}{C_{d,M} + C_{g,M}}; b_2 = -\frac{C_{g,M}}{C_{s,M}} \quad 5.3$$

Similar to the molecular orbital states, the states in the graphene leads shift linearly as a function of the applied bias and gate voltage. The energy shift of the states in the left lead, which is coupled to the source reservoir, is given by

$$\Delta\epsilon_L = -|e|(C_{sL}V_s + C_{gL}V_g)/(C_{sL} + C_{gL}) \quad 5.4$$

and for the right lead coupled to the drain reservoir

$$\Delta\epsilon_R = -|e|(C_{dR}V_d + C_{gR}V_g)/(C_{dR} + C_{gR}) \quad 5.5$$

In the case of asymmetric biasing, stripes in the conductance map for which a molecular orbital aligns with a state (quantization of the N_L sites due to the reflecting hopping integral) in the left lead have a slope given by $\mu_M = \epsilon_L = 0 + \Delta\epsilon_L$

$$\frac{dV_b}{dV_g} = \frac{C_{g,L}(C_{s,M} + C_{d,M}) - C_{s,L}C_{g,M}}{C_{g,L}C_{s,M} - C_{s,L}(C_{g,M} - C_{d,M})} \quad 5.6$$

For states (quantization of the N_R sites due to the reflecting hopping integral) in the right lead $\mu_M = \epsilon_R = 0 + \Delta\epsilon_R$, there is

$$\frac{dV_b}{dV_g} = \frac{C_{g,R}(C_{s,M} + C_{d,M}) - C_{s,R}C_{g,M}}{C_{g,R}C_{s,M} + C_{s,R}C_{s,M}} \quad 5.7$$

From the slopes of the edges of the Coulomb diamonds in Fig. 5.1c, it is inferred that there are ratios: $C_{g,M}/C_{s,M} = (33 \pm 1) \times 10^{-3}$, and $C_{g,M}/C_{d,M} = (20 \pm 1) \times 10^{-3}$. The relatively strong coupling to the source and drain electrodes compared to the gate electrode is due to the fact that the backgate is separated from the device by a 300nm layer of SiO₂. Next, the electrostatic coupling of the

lead states to the backgate is estimated. Conduction resonances with positive slopes is only observed, which implies that the experiment predominantly probes the left lead. From the positive slope of the conduction resonances it is found that $C_{g,L}/C_{s,L} = (7 \pm 1) \times 10^{-3}$, indicating that the gate coupling to the molecule is approximately 3~5 times stronger than to the lead states. So the difference in gate coupling between the molecule and the lead states is attributed to the higher carrier concentration in the graphene leads, which results in a more effective screening of the gate electric field. The average spacing between the conduction resonances is approximately 5 meV.

In basis of the above parameters such as $\epsilon_L, \epsilon_R, \mu_M$, we introduce a chain tight binding model to obtain a further insight into the Coulomb blockade and sequential tunnelling in terms of the effect of source-drain bias and backgate. The molecule is represented by a single site at $n = 0$ with an on-site energy μ_M and a hopping integral $\gamma_{L,R}$ to the left and right lead, respectively. The left and right leads are represented by semi-infinite chains with on-site energies $\epsilon_{L,R}$ and nearest-neighbour hopping integrals $\alpha_{L,R}$. We introduce scattering into the left and right compound electrodes at $n = -N_L$ and $n = N_R$ by adjusting the hopping integrals $\beta_{L,R}$.

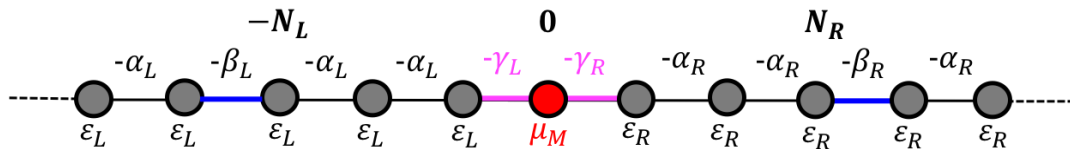


Fig. 5.2 Tight binding model of chain model with left, right semi-infinite electrodes and one molecular site. In each electrode, there exists one reflecting hopping

integrals $-\beta_{L(R)}$ at $-N_L$ and N_R sites. The number of sites between $-\beta_{L(R)}$ and $-\gamma_{L(R)}$ is $N_{L(R)} = 1000$ in the following simulation in order to keep consistent with the experimental energy level spacing of approximate 4~5meV.

When the lead states are clamped to the electrochemical potential of the reservoirs, i.e., if the capacitive coupling between the leads and the gate is zero, the slope of the lines for which the molecular orbitals align with the lead states run parallel to the edges of the Coulomb diamonds (see Fig. 5.5). Parallel lines in conductance maps resulting from disorder and confinement in the leads of single-electron transistors have been studied extensively, for example in STM-fabricated devices in silicon. However, when there is capacitive coupling between the leads and the gate, these lines no longer run parallel to the edges of the Coulomb diamonds (see Fig. 5.4), and resonances between molecular and lead states shift in and out of the bias window.

As a starting point, the Coulomb peak without fluctuations is researched based on the model in Fig. 5.2. In this case, $n = 1$ in the expression $\beta_L^2 = \beta_R^2 = n\alpha_{L(R)}^2$ is needed which means there exists no reflection in both electrodes. Fig. 5.3 shows the corresponding features.

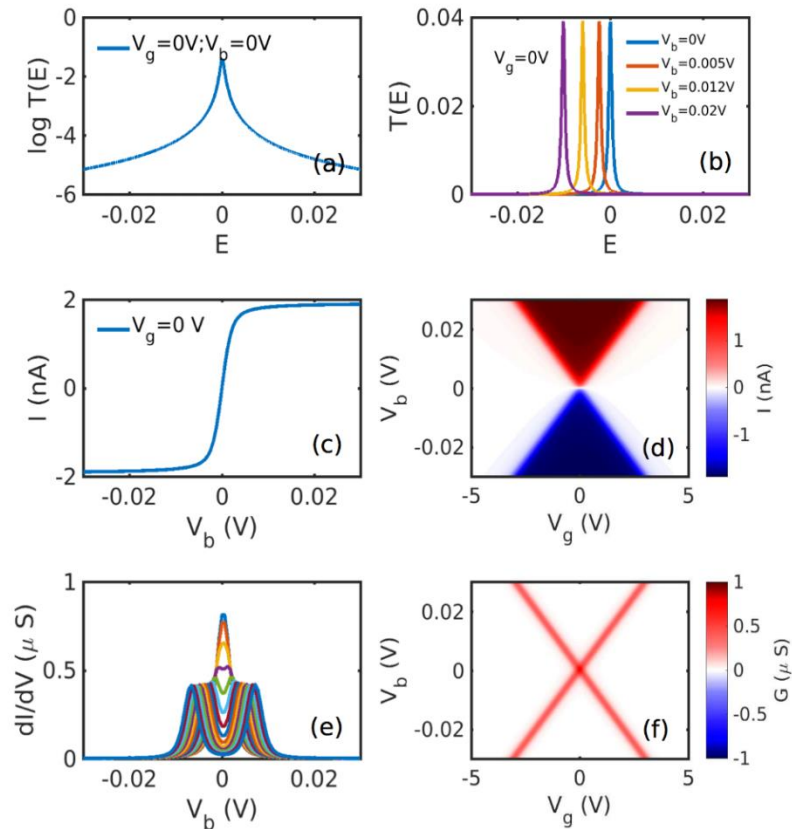


Fig. 5.3 The Coulomb peak of single-electron transistors (SETs) without Local density state (LDOS) fluctuations in leads where $\beta_L^2 = \beta_R^2 = n\alpha_{L(R)}^2$, $n = 1$. (a) Transmission spectrum at $V_g = 0V$ in logarithm scale. (b) Transmission spectra at $V_g = 0$ and $V_b = 0V$ (blue), $0.005V$ (red), $0.12V$ (yellow), $0.02V$ (purple) respectively. (c) I-V curve at $V_g = 0V$. (d) Coulomb peak of current I . The blue and red triangles depict the opposite current. The current is blocked outside the triangles. The light blue and orange lines represent the slopes of the coulomb peak when the chemical potential (on-site energy) of the molecular site is equal to those of source and drain electrodes. (e) Differential conductances versus source-drain bias under different back gate voltage. (f) Coulomb peak of differential conductances G .

Fig. 5.3a and b present the transmission spectra under different bias and at $V_g = 0$. Due to the tuning of the bias, the shifting of the resonance is observed. Fig. 5.3 c,

d show the one specific current as a function of bias at $V_g = 0$ and the Coulomb peak of current as the function of V_b and V_g . The current plateaus appear in the curve and the Coulomb peak since the Breit-Wigner resonance is narrow relative to the energy-bias window $[-eV_b, 0]$. In consequence, the integration in Landauer formula always contain the whole Breit-Wigner resonance in the plateau range. Fig. 5.3 e and f depict the differential conductance curves versus bias under different gate and the corresponding Coulomb peak which rises from the non-zero slopes in Fig. 5.3 c. The magnitudes are always positive and so negative differential resistance can't be observed here.

As for $n = 0.6$ in the expression $\beta_L^2 = \beta_R^2 = n\alpha_{L(R)}^2$, that is, there exists reflection in both electrodes. Fluctuations (nonparallel stripes to the edges of Coulomb peak) in current or differential conductance Coulomb peak are observed which are different from the features in Fig. 5.3. The slope of the stripes is positive in agreement with the experiment. It is realized by setting γ_L smaller than γ_R , in our simulation, e.g. $\gamma_L = 0.1\gamma_R$. Consequently, the states in left lead dominates the fluctuations in conductance map which confirms the analysis that the experiment probes the states in left lead. Fig. 5.4a and b present the transmission spectra consisting of one main peak and many shoulder-resonances each side under different bias and at $V_g = 0$. The main peak corresponds to the molecular site while the shoulder-peaks are due to the quantized energy levels of the $N_{L(R)}$ sites in each electrode. In Fig. 5.4b, the higher and broader resonances (red and purple) happen when the level of molecular site aligns with the level in left lead. As the energy levels in lead and molecular single level are tuned separately by bias and backgate and when the levels in lead and molecule don't match each other, e.g. the

molecular single level aligning with the middle gap between two levels in lead, the lower and narrower transmission spectra in Fig. 5.4b occur.

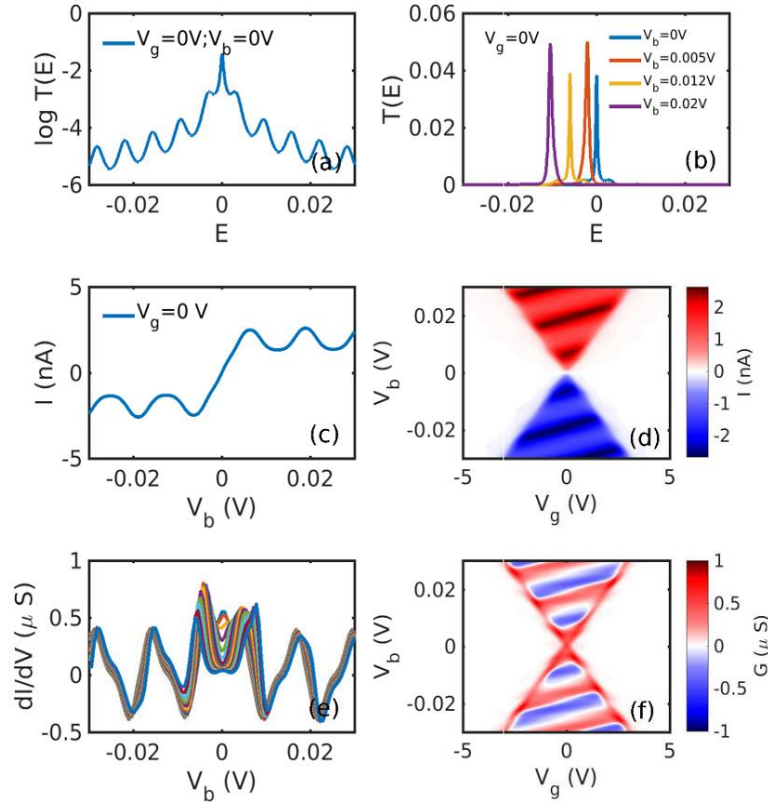


Fig. 5.4 Coulomb peak of SETs with non-parallel Local density state (LDOS) fluctuations to the edges of the coulomb blockade. $\beta_L^2 = \beta_R^2 = n\alpha_{L(R)}^2, n = 0.6$ (a) Transmission spectrum at $V_g = 0V$ in logarithm scale. (b) Transmission spectra at $V_g = 0$ and $V_b = V_b = 0V$ (blue), $0.005V$ (red), $0.12V$ (yellow), $0.02V$ (purple) respectively. (c) I-V curve at $V_g = 0V$. (d) Coulomb peak of current I . The light blue and orange lines represent the slopes of the coulomb peak when the chemical potential of the molecule is equal to those of source and drain electrodes. (e) Differential conductances versus source-drain bias under different back gate voltage. (f) Coulomb peak of differential conductances G .

Fig. 5.4c, d show the one specific current as a function of bias at $V_g = 0$ and the Coulomb peak of current as the function of V_b and V_g . Fluctuations are observed in

the curve and the Coulomb peak. The peaks in Fig. 5.4c correspond to the integration over the higher and broader transmission resonances. In contrast, the valleys in Fig. 5.4c arises from the lower and narrower transmission resonances. Fig. 5.4e and f depict the differential conductance curves versus bias under different gate and the corresponding Coulomb peak. Negative differential resistance is observed here which is due to the energy level's alignment and mismatch dependent on source-drain bias and backgate separately.

Based on the above model ($n = 0.6$ in the expression $\beta_L^2 = \beta_R^2 = n\alpha_{L(R)}^2$; $\gamma_L = 0.1\gamma_R$), the couplings between backgate and electrodes are not considered which means $C_{gl} = 0.0$; $C_{gr} = 0.0$ which means the back gate can't tune the two electrodes any more. Fluctuations in current (Fig. 5.5d) or differential conductance Coulomb peak (Fig. 5.5f) are observed, where the stripes are parallel to the edges of Coulomb peak. Fig. 5.5 a, b, c and d present the similar transmission spectra, $I \sim V_b$ and differential conductance $G \sim V_b$ curve to those in Fig. 5.5.

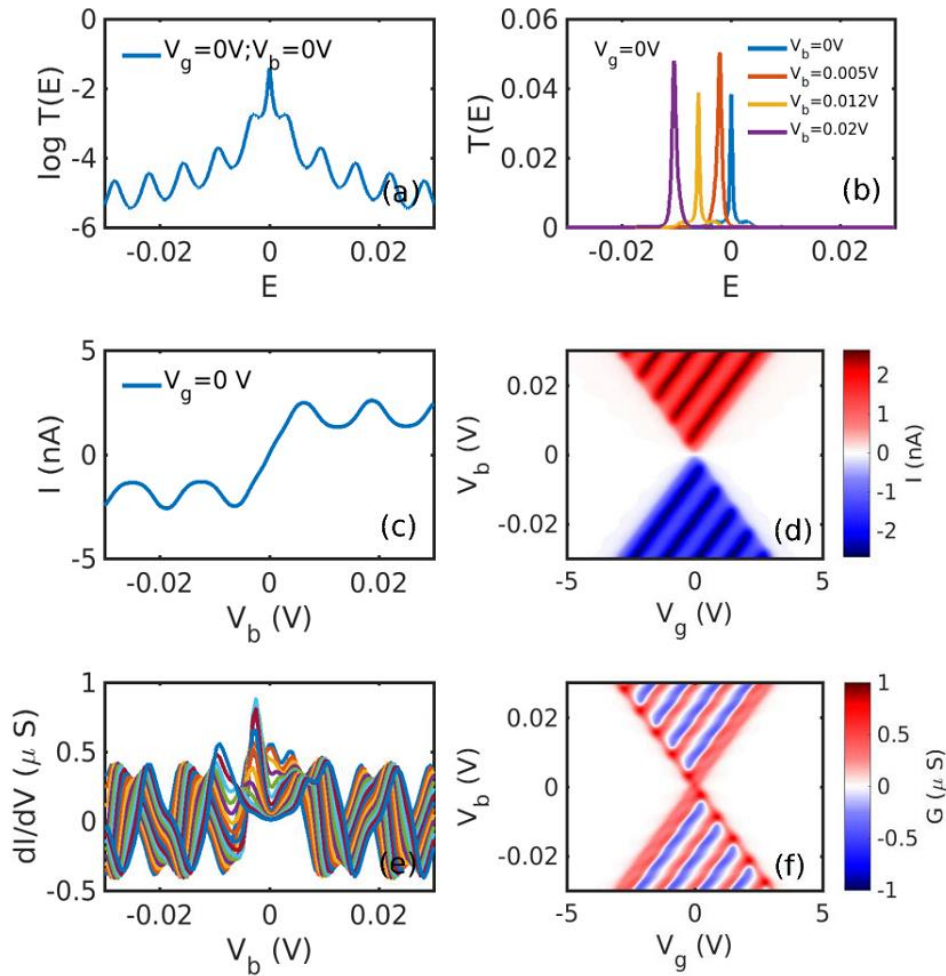


Fig. 5.5 Coulomb peak of SETs with parallel Local density state (LDOS) fluctuations to the edges of the coulomb blockade. $\beta_L^2 = \beta_R^2 = n\alpha_{L(R)}^2$, $n = 0.6$. The effect of gate on electrode is removed which means $C_{gl} = 0.0$; $C_{gr} = 0.0$. (a) Transmission spectrum at $V_g = 0V$ in logarithm scale. (b) Transmission spectra at $V_g = 0$ and $V_b = 0V$ (blue), $0.005V$ (red), $0.12V$ (yellow), $0.02V$ (purple) respectively. (c) I-V curve at $V_g = 0V$. (d) Coulomb peak of current I . The light blue and orange lines represent the slopes of the coulomb peak when the chemical potential of the molecule is equal to those of source and drain electrodes. (e) Differential conductances versus source-drain bias under different back gate voltage. (f) Coulomb peak of differential conductances G .

Now I want to discuss the hybridization between the lead states and the molecular orbitals as they are tuned in and out of resonance. The current through a molecular orbital is given by the Landauer formula[55] shown in Eq. 2.11.

To investigate the role of scattering in the leads on the transmission through the molecular orbital we continue adopting the simple tight-binding model as shown in Fig. 5.2. For simplicity, the equilibrium system is considered, that is to say, $V_b = 0$ and $V_g = 0$.

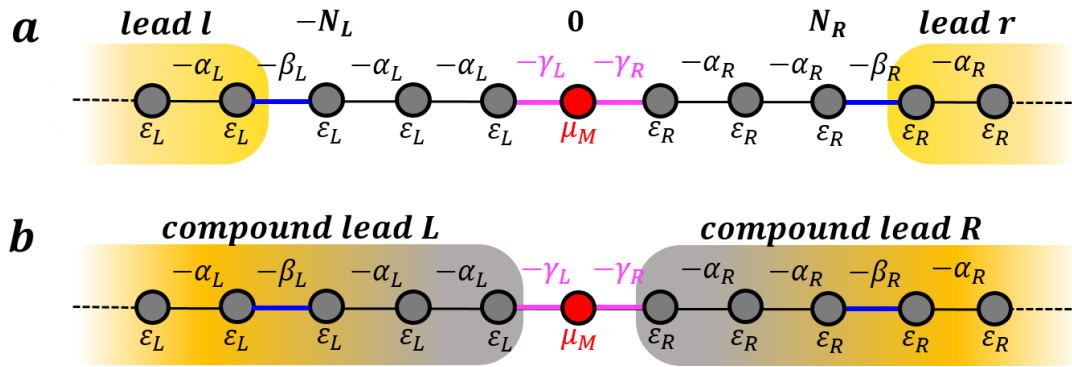


Fig. 5.6 Partitioning the molecule-lead system. (a) Partitioning of the system into simple lead l and lead r with a complex scattering region, and (b) into "compound leads" L and R and a simple scattering site M.

Traditionally one would regard this structure as a complicated scatterer (S) consisting of the region between $-N_L \leq n \leq N_R$ and two simple crystalline leads (shaded orange in Fig. 5.6a) along which electrons propagate ballistically into and from the simple leads. For such a system,

$$T(E) = 4Tr[\Gamma_l G_{SS} \Gamma_r G_{SS}^\dagger] \quad 5.8$$

where Γ_l and Γ_r describe the level broadening due to contact with the crystalline semi-infinite leads, l and r . In this expression, the scattering region is a complex combination of the molecule and graphene and G_{SS} is the Green's function of the scattering region in the presence of the simple crystalline leads. Our aim is to separate the contributions to scattering from the molecule and graphene and therefore we adopt an alternative formulation in which the left graphene, and left semi-infinite lead, i.e., the region $n < 0$, are regarded as a compound electrode (L) and the right graphene and right semi-infinite lead ($n > 0$) form the right compound electrode (R). This viewpoint is encapsulated in the following alternative expression for the transmission coefficient, which is mathematically equivalent to Eq. 5.8

$$T(E) = 4Tr[\Gamma_L G_{MM} \Gamma_R G_{MM}^\dagger] \quad 5.9$$

The Green's function of the molecule in the presence of the compound electrodes is given by

$$G_{MM} = (E - \mu_M - \Sigma_L - \Sigma_R)^{-1} \quad 5.10$$

where the self-energies of the left and right compound electrodes are

$$\Sigma_L = H_{ML}[g_{LL}]_{bb}H_{LM} = \sigma - i\Gamma_L \quad 5.11$$

$$\Sigma_R = H_{MR}[g_{RR}]_{cc}H_{RM} = \sigma - i\Gamma_R \quad 5.12$$

Where b, c represent the surficial sites for the compound leads shown in Fig. 5.7.

Using Eq.s 5.9-5.12, we obtain the following formula

$$T(E) = \frac{4\Gamma_L\Gamma_R}{(E - \mu_M - \sigma_L - \sigma_R)^2 + (\Gamma_L + \Gamma_R)^2} \quad 5.13$$

In this equation, the level broadening due to contact between the molecule and the left and right compound electrodes are described by

$$\Gamma_L = \frac{\gamma_L^2 \left([g_{LL}]_{bb} - [g_{LL}^\dagger]_{bb} \right)}{-2i} \quad 5.14$$

$$\Gamma_R = \frac{\gamma_R^2 \left([g_{RR}]_{cc} - [g_{RR}^\dagger]_{cc} \right)}{-2i} \quad 5.15$$

where $[g_{LL}]_{bb}$ and $[g_{RR}]_{cc}$ are the Green's functions of the isolated compound left and right electrodes, and γ_L and γ_R denote the coupling between the left, right compound electrodes and the molecule.

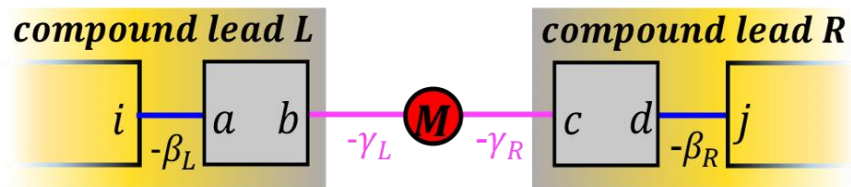


Fig. 5.7 A specific model for Fig. 5.6b. The molecule M is connected to b and c sites of compound electrodes L and R. $-\beta_L$ is the scattering integral which connects site i and site a in the left lead while the other scattering integral $-\beta_R$ connects site d and site j in the right lead.

In Fig. 5.7, the surface Green's functions for the compound left and right electrodes are derived as follows,

$$[g_{LL}]_{bb} = \frac{g_{bb} - \beta_L^2 g_i (g_{aa} g_{bb} - g_{ba} g_{ab})}{1 - \beta_L^2 g_i g_{aa}} \quad 5.16$$

$$[g_{RR}]_{cc} = \frac{g_{cc} - \beta_R^2 g_j (g_{dd} g_{cc} - g_{cd} g_{dc})}{1 - \beta_R^2 g_j g_{dd}} \quad 5.17$$

$$\hbar V_L \gamma_L^2 |[g_{LL}]_{ib}|^2 = 2\Gamma_L = -2\gamma_L^2 \text{Im}[g_{LL}]_{bb} \quad 5.18$$

$$\hbar V_R \gamma_R^2 |[g_{RR}]_{jc}|^2 = 2\Gamma_R = -2\gamma_R^2 \text{Im}[g_{RR}]_{cc} \quad 5.19$$

Where g_{bb} , g_{aa} , g_{ab} , and g_{ba} are Green's function for the isolated finite chain. $g_{i(j)} = -e^{ik}/\alpha_{L(R)}$ is the surface Green's function for the electrode in Fig. 5.6b. $V_{L(R)}$ is the Fermi velocity of the electrode in Fig. 5.6b. Eq. 5.18 and Eq. 5.19 indicate the relationship between surface Green's function $[g_{LL}]_{bb}$, $[g_{RR}]_{cc}$ and the Green's function $[g_{LL}]_{ib}$, $[g_{RR}]_{jc}$ which contain the information of disorders in the compound electrodes.

In the case of the simple tight binding model, this implies that the tunnel-rate $\Gamma_{L(R)}$ is proportional to the local density of states ρ_b at site $n = -1$ and Γ_R is proportional to the local density of states ρ_c at site $n = +1$. The relationship between them is given by

$$\Gamma_L = -\gamma_L^2 \text{Im}[g_{LL}]_{bb} = \pi\gamma_L^2 \rho_b \quad 5.20$$

Similarly

$$\sigma_L = \gamma_L^2 \text{Re}[g_{LL}]_{bb} \quad 5.21$$

Similar expressions hold for the right electrode.

Both the tunnel-rates and the energy shifts depend on the electrode density of states, which in turn is determined by the random locations of scattering centers within the graphene electrodes. The self-energies of the compound electrodes in the tight binding model can be found numerically by decimation or analytically by solving Dyson's equation. The latter yields

$$Z_L = \frac{\sin k_L e^{-ik_L N_L} - x_L \sin k_L (N_L - 1)}{\sin k_L e^{-ik_L N_L} - x_L \sin k_L N_L e^{ik_L}} \left[-\frac{\gamma_L^2}{\alpha_L} e^{i(k_L)} \right] \quad 5.22$$

where $x_L = \beta_L^2/\alpha_L^2 - 1$ and $k_L = \cos^{-1}(\varepsilon_L - E)/2\alpha$. Similarly Γ_R is obtained by replacing L by R in the above expression. Here we have derived the transmission for a simple one-dimensional tight binding model, however Eq. 5.8 and Eq. 5.9 are completely general, and the transmission function will depend on the details of the system Hamiltonian. Experimentally, we find that the position of the molecular energy level with respect to the Fermi energy of the leads and the strength of the coupling between the molecule and the graphene leads varies significantly from device to device.

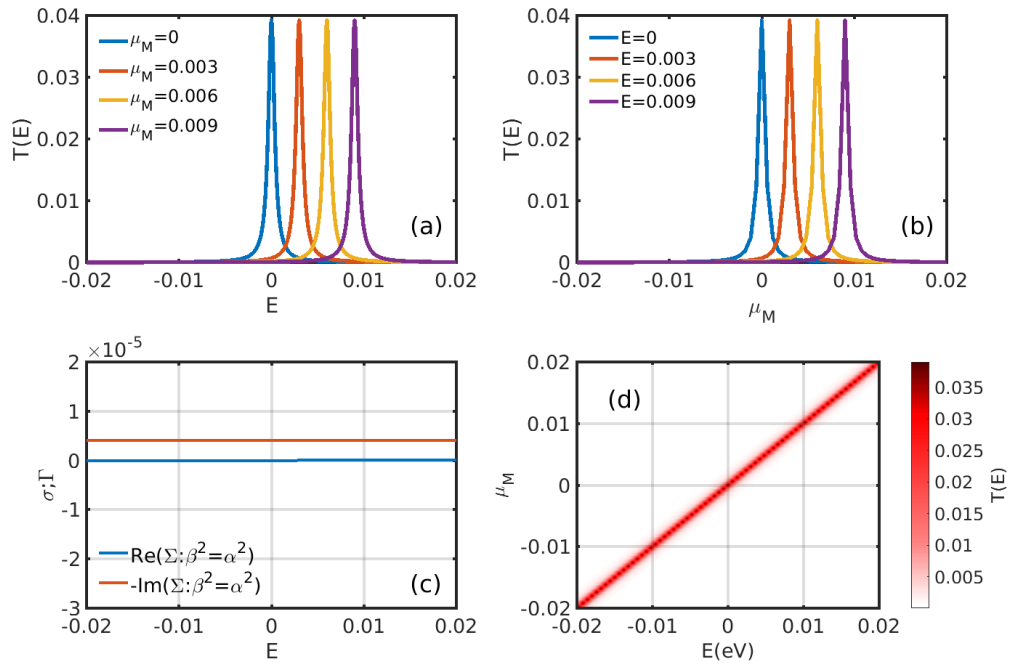


Fig. 5.8 Transmission spectra, tunnel-rate and hybridization energy calculated for $\alpha_{L,R} = 1$, $\epsilon_{L,R} = 0$, $\gamma_L = 0.002$, $\gamma_R = 0.02$, $\beta^2 = \alpha^2$ and $N_{L,R} = 1000$. (a) Transmission spectra as a function of energy with different chemical potential (on-site energy) of the dot, $\mu_M=0$ (blue), 0.003 (red), 0.006 (yellow), 0.009 (purple). (b) Transmission spectra as a function of different chemical potential μ_M of the dot with four specific energies $E=0$ (blue), 0.003 (red), 0.006 (yellow), 0.009 (purple). (c) Real (σ) and imaginary (Γ) parts of the self-energies. Here the curves of imaginary parts are shifted up by 0.0005 in order to present the curves clearly. (d) Transmission as a function of energy E and on-site energy μ_M .

As a starting point, Fig. 5.8 shows the real and imaginary parts of the self-energies and transmission spectra for the system without reflections ($\beta^2 = \alpha^2$) in the leads. The self-energy or Green's function are almost independent of energy (Fig. 5.8c) on the scale plotted, in agreement with equations (5.20) and (5.21). Transmission spectra have the same behaviour as a function of energy of the electron injected given a specific μ_M (Fig. 5.8a) and the on-site energy of the molecular site given an

electron of specific energy (Fig. 5.8b). Consequently, one straight line with a slope of unity is observed in the plotting of transmission coefficients as functions of the injected electron's energy and on-site energy of the molecular site (Fig. 5.8d).

Fig. 5.9a and b represent the transmission spectra as a function of E and μ_M . Both show that when the molecular level matches with a lead level, the transmission is broader and higher which accounts for the large Γ (Fig. 5.9c). These broader resonances correspond to the crossing points in Fig. 5.9d. In particular, the broader resonance has two peaks in Fig. 5.9a because the alignment happens between the left lead and molecule due to strong asymmetry in coupling strength between the left and right lead, i.e. $\Gamma_L \ll \Gamma_R$. The transmission resonance is only sensitive to states in the left lead.

Fig. 5.9c shows the real and imaginary part of the self-energies for strong and weak reflections in the leads. For strong reflection ($\beta_{L,R}^2 = 0.3\alpha_{L,R}^2$) we find sharp peaks in the imaginary part of the self-energies, i.e., the density of states at the surface sites ($n = \pm 1$), arising from quasi-bound states between the molecule and the reflection sites ($n = -N_L, N_R$). In contrast, for weak reflections ($\beta_{L,R}^2 = 0.6\alpha_{L,R}^2$) we find a small sinusoidal modulation of both the tunnel-rates $\Gamma_{L,R}$ and the energy shift $\sigma_{L,R}$. The tunnel-rate is maximum on resonance with the quasi-bound lead states while the real part of the self-energy changes sign upon crossing the resonance condition. The transmission as a function of energy and electrochemical potential of the molecule μ_M (Fig. 5.9d) shows both the effect of the modulation of the tunnel-rate and the real part of the self-energy (hybridization energy).

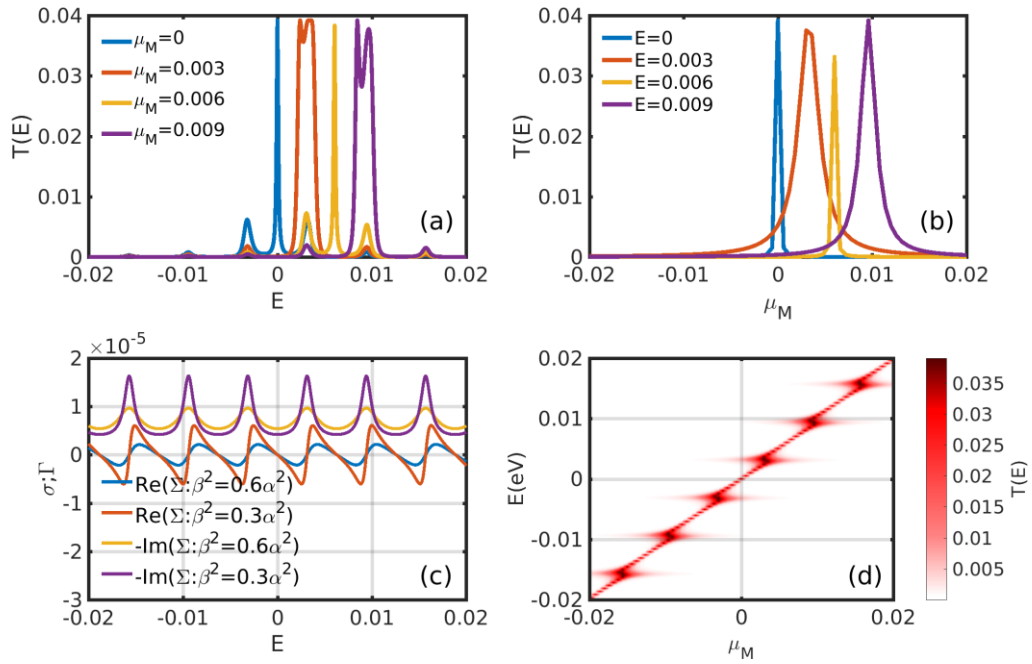


Fig. 5.9 Transmission spectra , tunnel-rate and hybridization energy calculated for $\alpha_{L,R} = 1$, $\epsilon_{L,R} = 0$, $\gamma_L = 0.002$, $\gamma_R = 0.02$ and $N_{L,R} = 1000$. (a) Transmission spectra ($\beta^2 = 0.3\alpha^2$ case) as a function of energy with different chemical potential (on-site energy) μ_M of the dot $\mu_M=0$ (blue), 0.003 (red), 0.006 (yellow), 0.009 (purple). (b) Transmission spectra as a function of different chemical potential μ_M of the dot with four specific energies $E=0$ (blue), 0.003 (red), 0.006 (yellow), 0.009 (purple). (c) Real and imaginary parts (σ) of the self-energies in two cases: $\beta^2 = 0.6\alpha^2$ and $\beta^2 = 0.3\alpha^2$. Here the curves of imaginary parts (Γ) are shifted up by 0.0005 in order to present the curves clearly. (d) Transmission as a function of energy E and on-site energy μ_M for the case $\beta^2 = 0.3\alpha^2$.

5.2.2 Applying magnetic field to distinguish the DOS in leads and molecule

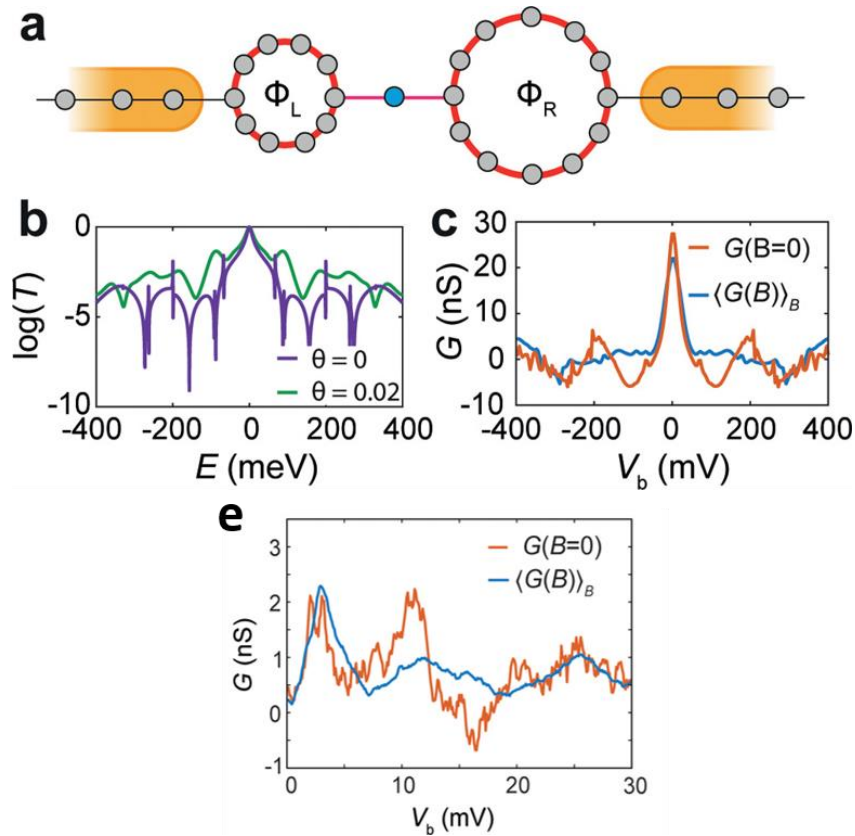


Fig. 5.10 Electrodes with ring-paths. (a) Tight binding model describing a molecular orbital connected to semi-infinite one-dimensional leads via ring paths. (b) Calculated transmission for two different values of $\theta = 2\pi\Phi/\Phi_0$. (c) Differential conductance at $B = 0$ compared to the ensemble averaged values, calculated for $\alpha_{ring,L} = \alpha_{ring,R} = 0.7\alpha_{L,R}$ and $\gamma_L = \gamma_R = 0.075\alpha_{L,R}$. (e) Differential conductance measured at $B = 0$ T compared with the ensemble averaged differential conductance in experiment.

The conductance fluctuations observed in the sequential tunnelling regime arise from interference effects in the leads, which can either be the result of scattering of random impurities leading to universal conductance fluctuations (UCFs), or Fabry-Pérot interferences resulting from reflections at potential barriers. When a magnetic field is applied perpendicular to the graphene leads, electron waves acquire an additional phase due to the vector potential. Theoretically, conductance

fluctuations can be reduced by a factor of \sqrt{N} where N is the size of the ensemble[129]. This behaviour can be illustrated by a tight-binding model shown in Fig. 5.10a, in which the leads contain circular regions through which a magnetic flux can pass. Again the transmission coefficient can be obtained analytically as a function of the flux Φ passing through each of the loops. This is imposed via a Peierls substitution by adding a phase factor $\theta = 2\pi\Phi/\Phi_0$ to nearest neighbour hopping integrals. In the absence of a magnetic field, Fig. 5.10b and c show an example of the transmission and differential conductance, which reflects the density of states fluctuations in such a model. The ensemble averaged curves show a strong reduction of the fluctuations, in correspondence with the experimental results in Fig. 5.10e.

The following presents the analytical derivation for the ring tight binding model shown in Fig. 5.10a. Consider a ring of N_L sites, with periodic boundary conditions. All of the above equations Eq. 5.8-5.22 are unchanged, except g_{aa}, g_{bb}, g_{ab} are replaced by the Green's function of a ring in Eq. 5.13. If the ring is threaded by a magnetic flux ϕ , then we define $\theta = \frac{2\pi\phi}{\phi_0} = \frac{2\pi}{\phi_0} \int_i^j \hat{A} dl$, where ϕ_0 is the flux quantum. This gauge applying is shown in the section 2.3.3.

The Schrödinger equation for such a lattice is

$$\varepsilon_L \varphi_j - \alpha_L e^{-i\theta} \varphi_{j+1} - \alpha_L e^{i\theta} \varphi_{j-1} = E \varphi_j \quad 5.23$$

The solutions which satisfy periodic boundary conditions are $\varphi_j = e^{i(\frac{2n\pi}{N})j}$. These have n eigen energies $E_n = \varepsilon_L - 2\alpha_L \cos[\frac{2n\pi}{N} - \theta]$, $n = 0, \pm 1, \pm 2 \dots, \pm(N-1)/2$, $N/2$ for N even (or $n = 0, \pm 1, \pm 2 \dots \pm(N-1)/2$, for N odd.)

Another way of stating this result is to write $\varphi_j = e^{i(\theta+\eta)j}$ or $\varphi_j = e^{i(\theta-\eta)j}$. The energy of these states is $E = \varepsilon_L - 2\alpha_L \cos \eta$.

Periodic boundary conditions require $\theta + \eta = 2n\pi/N$ and $-\eta = 2n\pi/N$. In fact, these are the same condition, because the set of numbers $\cos \eta_n = \cos(\frac{2n\pi}{N} - \theta)$ is identical to the set of numbers $\cos \eta_n = \cos(\theta - \frac{2n\pi}{N})$. To obtain the Green's function of such a ring at energy E , we define $\eta = \cos[(\varepsilon_L - E)/2\alpha_L]$.

Then for a ring of N sites, the Green's function matrix element g_{jl} connecting a source site l to a drain site j is

$$g_{jl} = \frac{e^{is\theta(|j-l|-\frac{N}{2})}}{4\gamma \sin \eta} \left\{ \frac{e^{i\eta(|j-l|-\frac{N}{2})}}{\sin[\frac{(\eta + s\theta)N}{2}]} + \frac{e^{-i\eta(|j-l|-\frac{N}{2})}}{\sin[\frac{(\eta - s\theta)N}{2}]} \right\} \quad 5.24$$

Where s is the sign of $(j-l)$. [$s = 1$ if $j-l > 0$ and $s = -1$ if $j-l < 0$] If $j = l$ either sign of s can be chosen, since both choices yields the same result.

Note that:

1. As expected $g_{jl} = g_{lj}^*$.

2. When $\theta = 0$, $g_{jl} = \frac{\cos \eta(|j-l| - \frac{N}{2})}{2\gamma \sin \eta \sin[\frac{\eta N}{2}]}$, in agreement with eq (9) of the literature [55].
3. Clearly g_{jl} diverges when $\theta + \eta = 2n\pi/N$ and $-\eta = 2n\pi/N$, as expected.
4. Derivation of Eq. 5.24 is shown in Appendices (Appendix 3).

5.3 Conclusion

In this work we have investigated the role of density of states fluctuations in single-molecule devices contacted to single-layer graphene nanoelectrodes experimentally and theoretically. By analysing local measurements of the quasi-bound lead states, we find that the electrostatic coupling to the global back-gate is weaker than the gate coupling to the molecule. This enables electrostatic control over the hybridization between lead and molecule states. A chain tight binding model is designed to show exactly the effect of local states in electrodes on the conductance map against V_g and V_b and further verifies the conduction fluctuations in the conductance map is due to the lead not the intrinsic characteristics of the molecule. If the energy-spacing between the quasi-bound lead states can be increased by further quantum confinement, they may act as an energy filter for the transport through the molecular orbitals. The approach of ensemble averaging magnetoconductance traces provides an effective way of distinguishing between features that are intrinsic to the molecule and those that are the result of quantum interference in the leads. A tight binding model with rings in the electrodes is investigated to have a further sight into the effect of the

magnetic fields which confirms the suppression of the fluctuations due to additional acquired phase. The averaging magnetoconductance traces provides a useful tool for the spectroscopic investigation of single molecules.

To conclude, our results highlight the importance of the electronic properties of the lead electrodes in single-molecule electronics. While graphene may be a material system that is very well suited to host these devices, further understanding of the hybridization between graphene and molecules will be needed to develop these devices into a technology. Atomically precise control of the structure and edge termination of the graphene leads, [130] together with stacked two-dimensional material approaches could enable functional graphene-molecule hybrid systems.

6 Low frequency noise in graphene tunnel junctions

6.1 Introduction

As the size of the electronic circuit decreases to the nanoscale, it is supposed that the device will be more sensitive to noise. In a molecular system, this is due to defects in the contact between electrodes and molecules or in the molecular layers, traps in the substrate[131][65], or due to the molecules in the solvent[132] or configurational changes[133]. So research on noise characteristics can make contributions to the understanding of fundamental principles and information in molecular junctions. Random telegraph noise (RTN), $1/f$ noise and shot noise in an alkyl-based self-assembled monolayer (SAM) adhered to two gold electrodes originate from the localized states in the tunnel barrier which helps to assess the effects of the localized states on charge transport[65]. Shot noise could provide information about the correlations of transmission probabilities among different conductance channels[65]. Noise characterisation is even exploited for biosensing[134]. In the past 40 years, varieties of functionalities in molecular electronics have been discovered and investigated in terms of the intrinsic charge transport properties[16][23][7][100] whereas only few studies on the electrical

noise characteristics as the functionalities of molecular devices have been carried out. It is of great significance to carry out the research and understand electrical fluctuations and noise for promoting and enhancing the development of molecular-scale devices.

Recent studies have demonstrated charge transport through single molecules which were firmly anchored between a pair of graphene electrodes via π - π stacking[25] or covalent bonding[40]. Moreover, graphene nanogaps have been proposed as candidate systems for molecular sensing,[132] in particular for sequencing DNA molecules[97]. These devices rely on the unique material properties of graphene: its two-dimensional nature, zero-energy bandgap, and semi-metallic conductance[135]. However, in graphene-based devices, electrical noise can't be avoided where both carrier fluctuations and mobility fluctuations play an important role[60]. As for the observation of random telegraph noise (RTN) in graphene, it has not been systematically researched and is expected to exist in small sized graphene where fewer surface or interface traps are expected. Furthermore, RTN in graphene nanogap junction has not been reported up to now. Conductance fluctuations or noise in 40–70 nm wide graphene nanoribbons was enhanced due to the quantum confinement effect [136]. So when structure approaches a ~ 1 nm nanogap, how the noise in empty graphene junctions behaves has not been addressed to date. This question becomes particularly pertinent for applications that require a large signal-to-noise ratio, such as DNA sequencing

Low-frequency $1/f$ noise or 'flicker' noise is ubiquitous in nanoscale electronic systems. While the physical mechanisms that generate these fluctuations may vary

and are often not known, it is generally accepted that $1/f$ noise is the result of a distribution of nonidentical random telegraph noise (RTN) which was first described by McWhorter in the context of interface traps in metal-oxide-semiconductor field-effect transistors (MOSFETs) where trapping and detrapping of charges results in fluctuations in the number of charge carriers in the semiconductor channel[131]. In the case of tunnel junctions, fluctuations in the electrostatic environment and mechanical instabilities will lead to noise in the tunnel current through modulation of the transmission function. Here, we will investigate the noise properties of nanometre-sized graphene tunnel junctions and present a theoretical description of the emergence of $1/f$ noise resulting from a distribution of classical fluctuators coupled to a quantum mechanical system.

6.2 Results and discussion

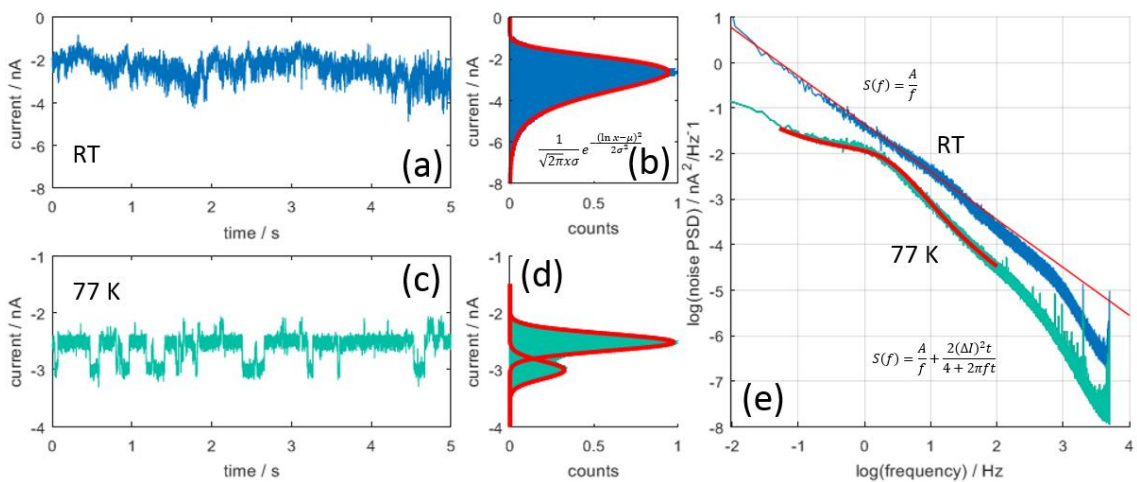


Fig. 6.1 Characteristics of 1/f and random telegraph noise (RTN) in graphene nanogaps (tunnel junctions). (a) Fluctuations in the tunneling current at room temperature (RT). (b) The corresponding log-normal distribution of current values of room temperature. (c) I-t trace with two levels upon cooling the device to 77 K. (d) Bimodal current distribution with two Gaussian peaks at 77K. (e) Noise power spectral density (PSD). Noise PSD follows 1/f trend at room temperature and Lorentzian noise spectral at 77K with lower overall noise level.

Fig. 6.1(a) shows the typical current–time ($I-t$) trace measured for a graphene tunnel junction at room temperature. The room temperature $I-t$ trace (Fig. 6.1a) shows characteristic flicker noise behaviour, in which the signal has a wandering baseline as the high frequency noise rides on a low frequency component. The corresponding histogram of the current at room temperature (Fig. 6.1b) reveals a distinct log-normal distribution of the current values and gives a first hint at the physical mechanism behind the $1/f$ noise. By contrast, the $I-t$ trace (Fig. 6.1c) predominantly fluctuates between two levels, indicating that a single two-level fluctuator dominates the noise. Similarly, Fig. 6.1(d) presents the corresponding current histogram distribution, which consists of two Gaussian peaks. The power spectral density of a single two-level fluctuator is given by $S_I(f) = \frac{2\Delta I^2\tau}{4+(2\pi f\tau)^2}$, where ΔI is the deviation between the two levels in the $I-t$ trace and τ the mean dwell time or lifetime of the fluctuator.[60][137] The Lorentzian profile consists of the frequency independent region below τ^{-1} and a $1/f^2$ dependence region far above τ^{-1} . If the fluctuations are thermally activated, the process follows the Arrhenius law $\tau^{-1} = \tau_0^{-1} e^{-E_a/k_B T}$. Reducing the temperature will shift the corner frequency τ^{-1} down[137]. The fact that RTS at 77 K is observed indicates that at

this temperature a smaller number of RTSs are sampled. More features correlated to RTNs observed in experiment are shown in Fig. 6.2.

When comparing the noise power spectral density $S_I(f)$ of the tunnel junction at room temperature and 77 K (Fig. 6.1e), it is found that $S_I(f)$ at room temperature is well described by A/f , whereas $S_I(f)$ at 77K shows a Lorentzian-shape noise with a distinct corner around $f = 1$ Hz superimposed onto a linear slope $1/f^a$ where $1 < a < 2$ which might originate from the switching of more remote traps with larger dwell times. Since the density of thermally activated fluctuators is typically not constant in space, their different activation energies can lead to the dominance of a single fluctuator within different spectral windows when the temperature is reduced.

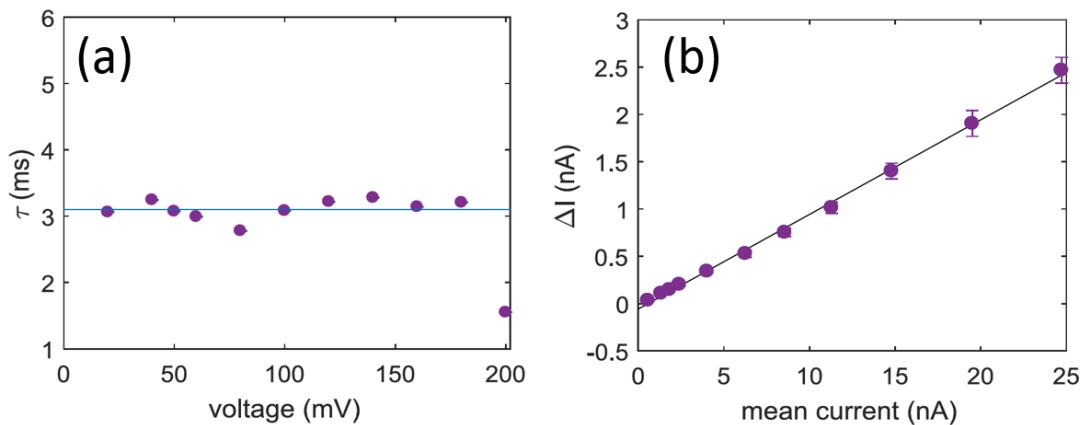


Fig. 6.2 RTS characteristics with voltage bias and tunnelling current. (a) Dependence of mean dwell time τ on applied voltage. Horizontal line shows $\tau = 3.1$ ms reference level. (b) Dependence of ΔI amplitude on the measured mean tunneling current.

The dependence of the amplitude and dwell time of RTS on applied voltage is presented in Fig. 6.2. The dwell time distribution shows no meaningful trend within the experimental error bars with increasing voltage (Fig. 6.2a). It indicates that a smaller number of environmental fluctuators with a narrower dwell time window are sampled. On the contrary there is a linear increase of the RTS ΔI amplitude with the increase in the mean tunnelling current (Fig. 6.2b). This indicates that the observed fluctuations in conductance are not driven by the tunnelling current, but they exist regardless of the current. The current is only a readout method of the independent fluctuations. This feature is clearly obtained in our tight binding simulation when one environmental fluctuator is considered.

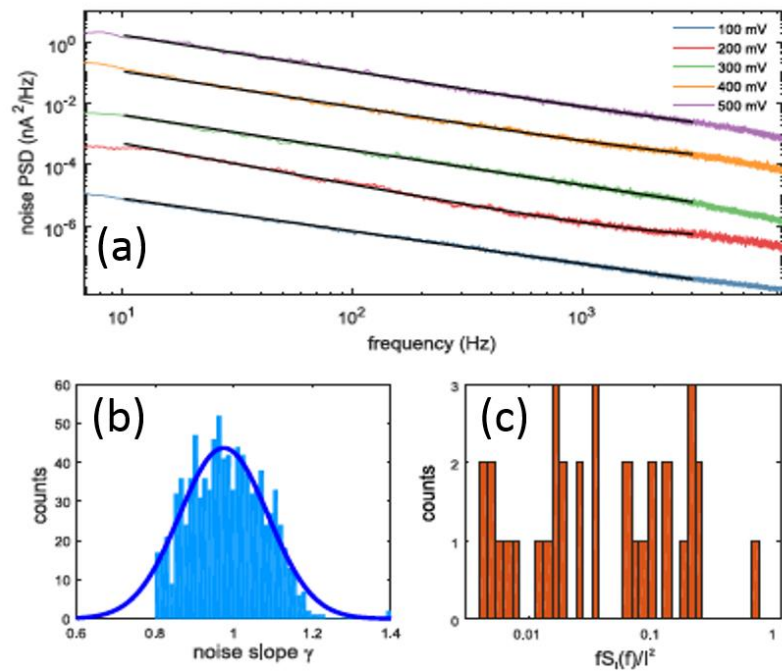


Fig. 6.3 $1/f$ noise in GTJs at room temperature (a) Noise spectra for several bias values. (b) Distribution of γ slopes fitted with Gaussian function. (c) Distribution of normalized $fSI(f)/I^2$ noise amplitude for 35 measured GTJs.

In terms of $1/f$ noise, to further characterise the noise amplitude, the normalized noise power spectral density $SI(f)/I^2$ for 35 devices are compared in experiment in Fig. 6.3. The noise spectra recorded for several voltage values show that the $1/f$ noise profile is present independent of the applied voltage and increasing voltage does not induce RTS at room temperature (Fig. 6.3a). It is found that the exponent $\gamma = 1 \pm 0.2$ (Fig. 6.3b) and its value does not depend on the tunnelling current. Deviations from $1/f$ are typically attributed to variations in the distribution of the RTSs, and the γ values obtained in our graphene tunnel junctions are very similar to values obtained for silicon devices[138], tunnel junctions[139], and nanopores[140]. More surprising are the values for the normalized noise amplitude, or pseudo-Hooge parameter, $\alpha = fS_I(f)/I^2$, which ranges from $\log \alpha = -2$ to 0 (Fig. 6.3c). These values are 7 to 9 orders of magnitude larger than those reported in micrometre-sized graphene channels[141], and 2 to 3 orders of magnitude higher than the normalized noise amplitude measured in graphene nanopores of comparable size to our tunnel junctions[142]. We attribute this large noise amplitude to the extreme sensitivity of the tunnel current to environmental fluctuations.

Here, I employ a simple one-dimensional tight binding models to gauge the effect of two-level fluctuations in the electrostatic environment of the tunnel junction. The tunnel barrier is modelled as a scattering region containing N sites with onsite energies ε_i , located between two semi-infinite leads. We investigate two types of models. Model I shows the effect of local environmental fluctuators on the tunnel barrier, while Model II represents the collective effect of the remote fluctuators in the environment on the tunnel barrier. By comparing our simulated and

experimental $I-t$ traces, we conclude that the 77 K data is best described by a single fluctuator influencing the transmission through the tunnel barrier for both types of models. A $1/f$ signal emerges as more fluctuators are added to the environment, corresponding to the thermal activation of multiple RTSs at room temperature.

Before starting the simulations, I present some background and simple introduction for the tight binding model which consists of three ingredients:

1. A quantum system comprising a conducting chain of N quantum levels with energies ε_i placed between two electrodes.
2. A classical fluctuating environment represented by one or more generalized coordinates x_i .
3. The coupling between the classical environment and the quantum levels of the conducting chain.

To introduce this tight binding model (TBM), the simplest case is considered which comprises a single energy level (red) and one environment fluctuator (trap x in Fig 6.4). In a more general model, the number of energy levels in the scattering region (i.e. the tunnel barrier) can be increased and the number of generalized coordinates x in the fluctuating environment can also be varied.

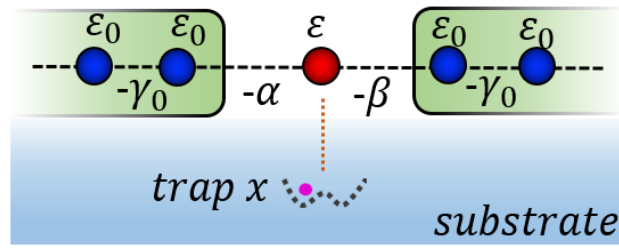


Fig. 6.4 A single energy level one dimensional tight binding model. $\varepsilon_0 = 0$ indicates the on-site energies of the left and right electrodes (blue balls). ε shows the on-site energy for the scattering site (red ball). The hopping integrals γ_0 in the two electrodes are all set to be unity. $\alpha = \beta = 0.35$ represents the coupling between electrodes and scattering site. x is a generalized coordinate describing an environmental trap.

The time dependence of the generalized coordinate x is described by the Langevin equation (Eq. 6.1), which models an overdamped ‘particle’ whose mass is negligible. In what follows, the potential landscape of this classical coordinate is represented in Eq. 6.2, which possesses two minima, as shown Fig. 6.5(a). The two minima are located at $x = \pm\sqrt{c_i}$, and the depth of the wells is $\frac{c_i^2}{40}$ relative to $U = 0$ in Fig. 6.5(a). The values of c_i are specified in each model below. The fluctuating environment x is subject to Gaussian white noise, as shown in Fig. 6.5(b). As for the Gaussian white noise, Eq. 6.3 and Eq. 6.4 show the correlation function and the derived variance when the expectation μ is 0. The damping coefficient λ is set to be 0.0015. Here, k_B is Boltzmann’s constant and T is temperature. Fig. 6.5 (c) shows that the displacement $x(t)$ is located mainly at -1, 1 and fluctuates between when $c_i = 0.4$. More examples for c and U are shown in Table 1.

$$\lambda \frac{dx(t)}{dt} = \frac{-dU(x)}{dx} + \eta(t) \quad 6.1$$

$$U_i(x) = \frac{x^4}{40} - c_i \frac{x^2}{20} \quad 6.2$$

$$\langle \eta(t) \eta(t') \rangle = 2\lambda k_B T \delta(t - t') \quad 6.3$$

$$\langle \eta^2(t) \rangle = \frac{2\lambda k_B T}{\Delta t} = \sigma^2 \text{ (when } \mu = 0 \text{)} \quad 6.4$$

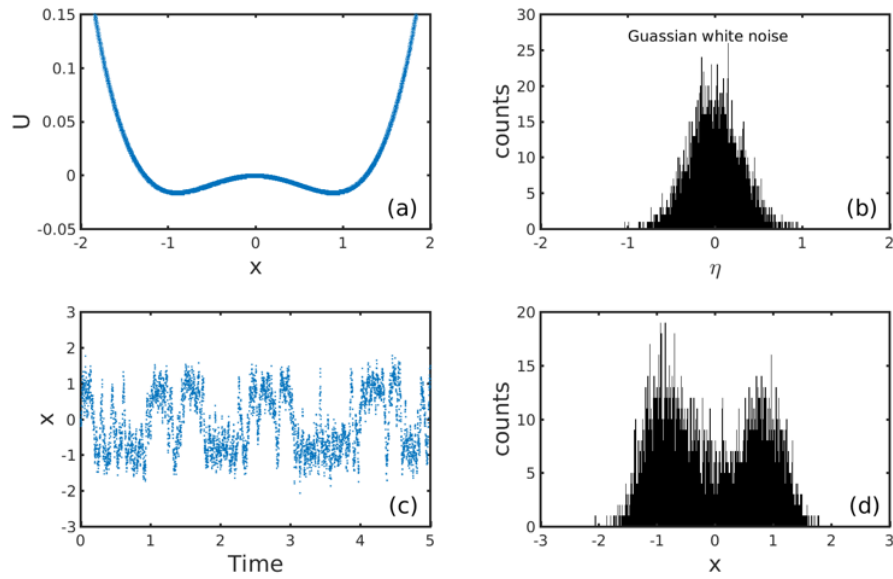


Fig. 6.5 An environmental 'charge' x fluctuating between two potential minima. (a) The potential landscape introduced in Langevin Equation. (b) Gaussian white noise. (c)-(d) Fluctuations versus time and histogram distribution of the fluctuating environment x .

Table 1: The potential well depth associated to parameter c and a . At low temperature (77K), $k_B T = 6.6 \text{ meV}$ and at room temperature $k_B T = 25 \text{ meV}$ provided $\gamma_0 = 1 \text{ eV}$ in my simulation.

c	0.4	0.6	0.8	1.0	1.8	2.4	3.0
$U=c^2/a; a=40; (\text{meV})$	4	9	16	25	81	144	255

As for the relationship between the quantum system and the environmental classic system, the simplest possible relationship, $\varepsilon \propto x$ is adopted. More specific details could be found in the following sections. In what follows, two types of TBMs are considered, denoted model I and model II. In each type, two models (a) and (b) are displayed, which reproduce the switching behaviour and log-normal distribution of measured current.

Fig. 6.6 shows the models used for low temperatures (77K) and room temperature. Variants (a) and (b) of Model I are used to simulate the case where the perturbation originates from the local environment. Or we can say, the tunnel barrier is driven by the environmental fluctuators differently and locally. The one-dimensional chains consisting of blue balls represent electrodes. ε_i shows the on-site energies for the scattering region (the grey and red balls) which forms a tunnel barrier. The red sites could be stimulated by the environmental charge x while the grey sites are static. At 77K, one trap in the substrate is considered while several traps are activated by the higher temperature.

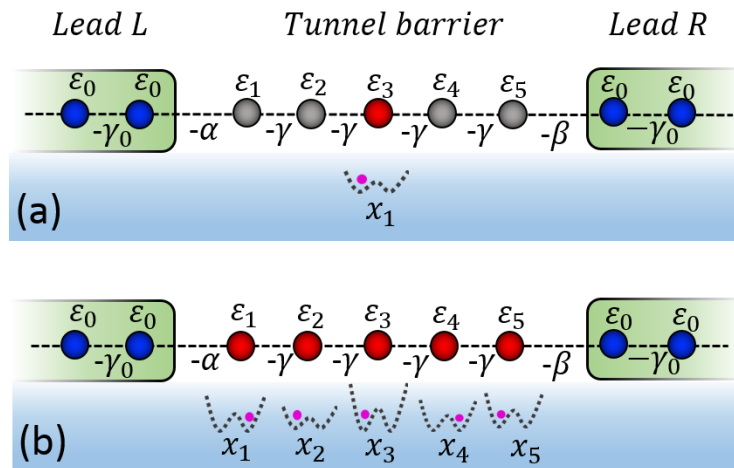


Fig. 6.6 Tight binding models I for two-level current at 77K and current with $1/f$ noise at room temperature. $\varepsilon_i \sim x_i$ (a) One fluctuating level (red) among the five in the scattering region due to one environmental trap x_1 . The index number of the fluctuating level (red) is randomly chosen in different samples which are used for ensemble average noise power spectral density. (b) All levels fluctuating stimulated by more potential wells $\{x_1, x_2, \dots, x_5\}$ with different well depths. $\varepsilon_0 = 0$ indicates the on-site energies of the left and right electrodes (the blue balls) in the light green shades. ε_i shows the on-site energy for the scattering region (the grey and red balls) which forms a tunnel barrier. The red sites could be stimulated by the environmental charge x while the grey stays static. The hopping integrals γ_0, γ in the two electrodes are all set to be unity. $\alpha = \beta = 0.35$ represent the coupling between electrodes and scattering site. x is a generalized coordinate describing an environmental trap. ε_i is linear to x_i .

Here, we define the height of tunnel barrier between the two leads to be the difference between the Fermi level and the mean value (the blue dashed baseline in Fig. 6.7c) of the lowest eigenvalue of the scattering region. So the deviation means the difference between the two mean values (the red dashed baselines in Fig. 6.7c) of the two-level eigenvalue trace. The deviations of tunnel barrier height depend on the position of the site energy in the scattering region, which is

perturbed by the environmental fluctuator. That means the position where perturbation is imposed will determine the amplitudes of the fluctuations of the quantum system. More details are shown in Fig. 6.7 which corresponds to model I (a) in Fig. 6.6.

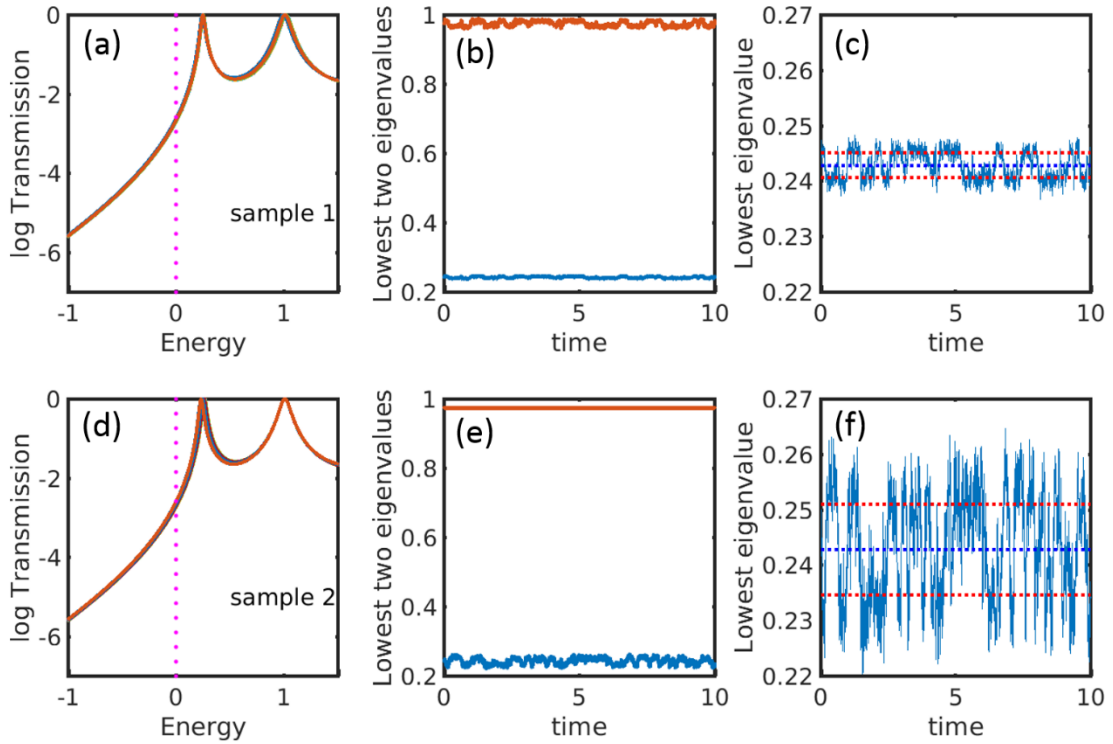


Fig. 6.7 Fluctuations of eigenvalues depending on the position in the scattering region which is influenced by the environmental trap in model I(a) shown in Fig. 6.6(a). (a, d) Transmission spectra of the two samples. ε_5 is influenced by the fluctuating environmental charge in sample 1 (the top panel) while ε_3 is affected in sample 2 (the bottom panel). (b, e) Lowest two eigenvalues which correspond to the two transmission peaks in (a, d). (c-f) The lowest eigen value trace among the five eigenvalues. The blue dashed baseline demonstrates the mean tunnel barrier height referred to the Fermi level of the whole device $E_F = 0$. The two red dashed baselines above and below the blue are the mean value for each level. The difference between the two red lines is defined as the deviation of the tunnel barrier.

Fig. 6.7 depicts the dependence of the fluctuating amplitude of the eigenvalues on the position which is influenced by the environmental charge. This phenomenon is explained by the perturbation theory. For a Hamiltonian $H = H_0 + H_1$, where H_0 is the original Hamiltonian and H_1 is the perturbation, the total energy is approximately $E = E_0 + \langle \psi^n | H_1 | \psi^n \rangle$. For a finite chain consisting of 5 sites, the eigenstate is $\psi_j^n = \sqrt{\frac{2}{N+1}} \sin k_n j$ where $k_n = \frac{n\pi}{6}$; $n = 1, 2, \dots, 5$. So finally, in terms of the lowest eigenvalue, the additional energy stemming from eg a perturbation $H_1 = \eta \delta_{i5}$, which acts on site 5 only, is $\Delta E_1 = \frac{2\eta}{N+1} \left(\sin^2 \frac{\pi}{6} \cdot 5 \right)$. Similarly a perturbation $H_1 = \eta \delta_{i3}$, which acts on site 3 only causes a shift $\Delta E_2 = \frac{2\eta}{N+1} \left(\sin^2 \frac{\pi}{6} \cdot 3 \right)$. Since $\Delta E_2 > \Delta E_1$, the amplitudes of the lowest eigenvalues in Fig. 6.7(c) is less than those in Fig. 6.7(f). The second-lowest eigenvalues in orange in Fig. 6.7(e) exhibit a totally a straight line because the site ε_3 in the middle of the scattering region and $\Delta E_2 = \frac{2\eta}{N+1} \left(\sin^2 \frac{2\pi}{6} \cdot 3 \right) \frac{x}{20} = 0$. So when the perturbation is imposed on the nodes in eigenstate for the chain consisting of odd sites, there can be no influence on the backbone for some eigenvalues. A more pronounced effect is observed for other eigenvalues. All these features are determined by the position at which the perturbation is imposed.

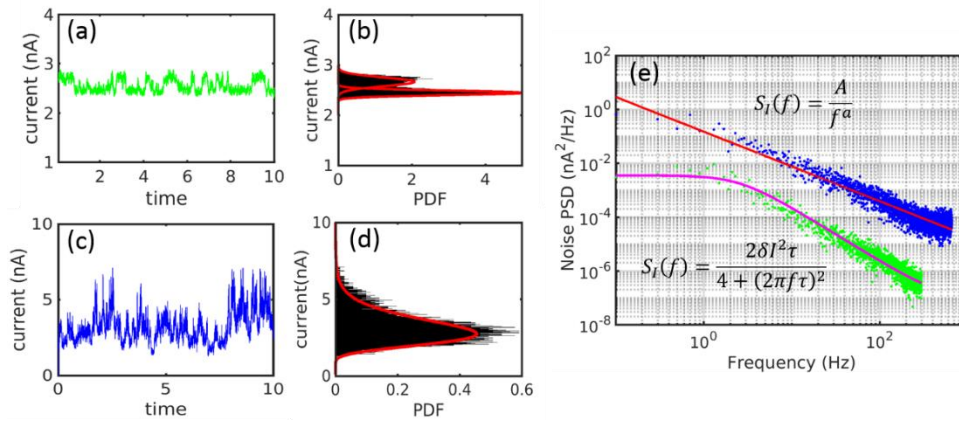


Fig. 6.8 Characteristics of currents and noise power spectral density (PSD) corresponding to Model I in Fig. 4. (a)-(b) Switching behavior corresponding to Model I (a) where the potential parameter $c=0.4$. Therefore, the ratio of potential well and thermal energy at 77K is $\frac{U}{k_B T} = \frac{4}{6.6}$ which means this environmental fluctuator could be activated easily. (c)-(d) Log-normal current distribution with flicker noise $1/f^a$ corresponding to Model I (b) where a is equal to 1.2. ε_i is linear to x_i , i.e. $\varepsilon_i = \frac{x_i}{20} + 1.975$. $\{c_i\} = 0.4, 1.0, 1.7, 2.4, 2.9$ where the potential of $c = 1.0$ corresponds to the $k_B T$ at room temperature in terms of energy.

Fig. 6.8 shows the current traces, current histograms, noise power spectral density for the tight binding model I (a), (b) in Fig. 6.6. Fig. 6.8(a) shows that the current-time trace has a switching behaviour with two main steps which originates from the tunnel barrier in the scattering region subject to a single potential well with two minima. Fig. 6.8 (b) is the corresponding current histogram with two Gaussian peaks. Then in terms of the features in the experiment at room temperature, more potential wells in the environment are activated, so in the simulation, we consider the effect of 5 potential wells with different well depths. These 5 potential wells drive the energy levels differently to simulate traps close to the tunnel barrier, which leads to the log-normal current histogram distribution shown in Fig. 6.8(c),

(d) where potential-well parameters are $\{c_i\} = \{0.4, 1.0, 1.7, 2.4, 2.9\}$. These five potential wells have depth $\frac{U}{k_B T} = 4/25, 25/25, 72/25, 144/25, 210/25$ compared to $k_B T$ at room temperature. In addition, the magnitude a is also associated with other factors (i.e. the fluctuations of the barrier height) shown in Fig. 6.10. Fig. 6.8(e) is the PSD spectra for the two-level current and the current with a log-normal distribution. It should be noted that the PSD denoted by green dots (with a magenta fitting curve) has a good Lorentzian profile, while the one denoted by blue dots (with a red fitting curve) has flicker noise characteristic $S_I(f) = A/f^a$ where a is equal to 1.2 which is in an acceptable region[137].

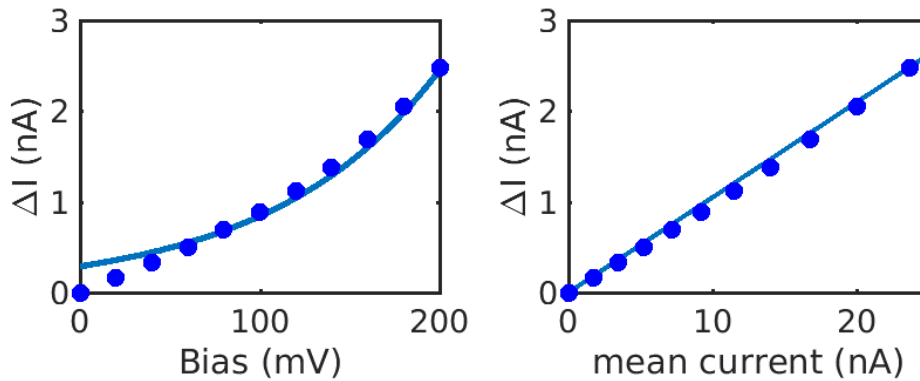


Fig. 6.9 Features of current and noise power spectral density (PSD) corresponding to Model I (a). ε_i is linear to x_i , i.e. $\varepsilon_i = \frac{x_i}{20} + 1.975$. (a) Exponential increase between current deviations ΔI and source-drain bias voltages applied. (b) The linear relationship between current deviations ΔI and mean currents of the two-level current system. Current deviation ΔI means the difference between the mean values of the two levels. The mean currents in (b) are the mean values for the whole two-level currents.

Fig. 6.9(a) presents the exponentially increasing tunneling current feature against bias. ΔI is the difference of the two mean values of the two steps $\Delta I = I_{up} - I_{down}$. Here, the transmission has the form of $T(E) = T_0 e^{-\beta(E_F)L}$ due to the Fermi level located in the tail of the transmission peak dominated by the lowest eigenvalue. This exponential term in transmission is the origin of the exponential current feature. In the other hand, this deviation of current ΔI increases linearly with the mean current of the whole current trace with time. It is noted that the slope of fitting curves consist is 0.1, which is in qualitative agreement with the experimental results. In my simulation, the fluctuators in the environment are not affected by the bias voltage applied on the quantum system. The obtained qualitative agreement with experiment support the conclusion that the noise is not driven by the tunneling current in graphene nanogaps. In the basis of these qualitative agreements, it is estimated that the ratio between the tunnel barrier u and the deviation of the tunnel barriers between the two-level steps Δu is approximately 0.035 ($\Delta u/u = 0.035$). All the features depicted in Fig. 6.12 are in qualitative agreement with the experimental results.

Put in another way, if the Fermi level is fixed, variations of the tunnel barrier height among the samples could exist and can lead to the transmission variations. Consequently, the current would vary and the slope magnitude a of the flicker noise $1/f^a$ would have fluctuations. For the choice of $\varepsilon_i = \frac{x_i}{4} + 2.35$, the corresponding plots are shown in Fig. 6.10. The two-level current, the Lorentzian noise, exponential and linear increasing current features, the log-normal distribution currents, the $1/f$ noise power spectral density are all shown in Fig. 6.10, which are in good agreement with the previous simulation. Finally, we find

that the slope a of flicker noise $1/f^a$ varies in the range of 1.0~1.2 in the simulations, which agrees very well with the experimental results shown in Fig. 6.3. The inset in Fig. 6.10(e) shows the linear relationship between current deviation and mean current.

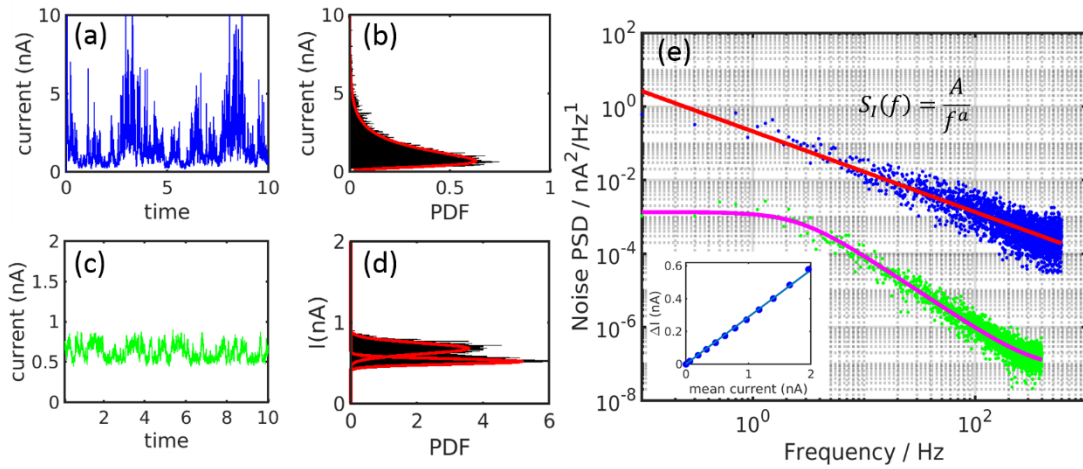


Fig. 6.10 Features of current and noise power spectral density (PSD) corresponding to Model I a, b. (a), (b) Current for Model I (a). (c), (d) Current for Model I (b). (e) PSD spectra for the two current traces. The magnitude of the flicker noise slope a is 1. ε_i is linear to x_i , i.e. $\varepsilon_i = \frac{x_i}{4} + 2.35$. $\{c_i\} = 0.4, 1.0, 1.7, 2.4, 2.9$.

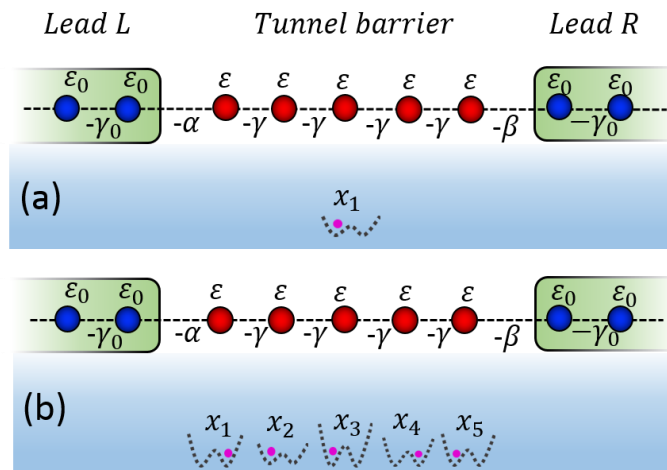


Fig. 6.11 Tight binding models II for switching behaviour at 77K and 1/f noise at room temperature. $\varepsilon \sim \sum_{n=1}^5 x_i$ The scattering region (tunnel barrier) driven by one environmental trap x_1 at 77K (a) and by the sum of several traps $\{x_1, x_2, \dots, x_5\}$ in different potential well depths at room temperature (b). $\varepsilon_0 = 0$ indicates the on-site energies of the left and right electrodes (the blue balls) in the light green shades. ε shows the on-site energy for the scattering region (the red balls) which forms a tunnel barrier. The hopping integrals γ_0, γ in the two electrodes are all set to be unity. $\alpha = \beta = 0.35$ represent the coupling between electrodes and scattering site. x is a generalized coordinate describing an environmental trap. The tunnel barrier could be tuned by the environmental traps synchronously.

Fig. 6.11 presents the models for low temperature (77K) and room temperature. (a) and (b) of Model II are used to simulate the case where the traps are buried deeper in the substrate. The semi-infinite chains consisting of blue balls represent electrodes. The scattering region (red balls) forms a tunnel barrier with the same on-site energy ε for both models (a) and (b). In other words, the tunnel barrier is driven by the superposition of all the potential wells. At 77K, one trap in the substrate is considered, while several traps are activated at higher temperatures. The simulation results are shown in the following. Fig. 6.12 shows the current

traces, current histograms, noise power spectral density for the tight binding models (a), (b) shown in Fig. 6.11. Fig. 6.12(a) depicts the current trace has switching behaviour with two main levels which originates from the tunnel barrier in the scattering region subject to one two-well potential. Fig. 6.12 (b) is the corresponding current histogram with two Gaussian peaks. To model the experiments at room temperature, more fluctuators in the environment are activated, where, for example, 5 potential wells with different well depth are considered in the simulation. These 5 fluctuators drive the energy levels in the scattering region equally to simulate the traps buried deeply in the substrate, which leads to the log-normal current histogram distribution shown in Fig. 6.12 (c), (d). Fig. 6.12(e) presents PSD spectra with the potential wells $\{c_i\} = 0.4, 0.8, 1.2, 1.8, 2.5$ for the A/f^a noise, where $a=1.3$ in this calculation and $c=0.4$ for the Lorentzian-shape noise. $\{c_i\}=0.4, 1.2, 1.9, 2.5, 3.2$ was also tried and the magnitude of the slope was found to decrease further to 1.2. In addition, the magnitude a is associated with other factors (i.e. the fluctuations of the tunnel barrier height) shown in Fig. 6.14. All the features depicted in Fig. 6.12 are in qualitative agreement with the experimental results.

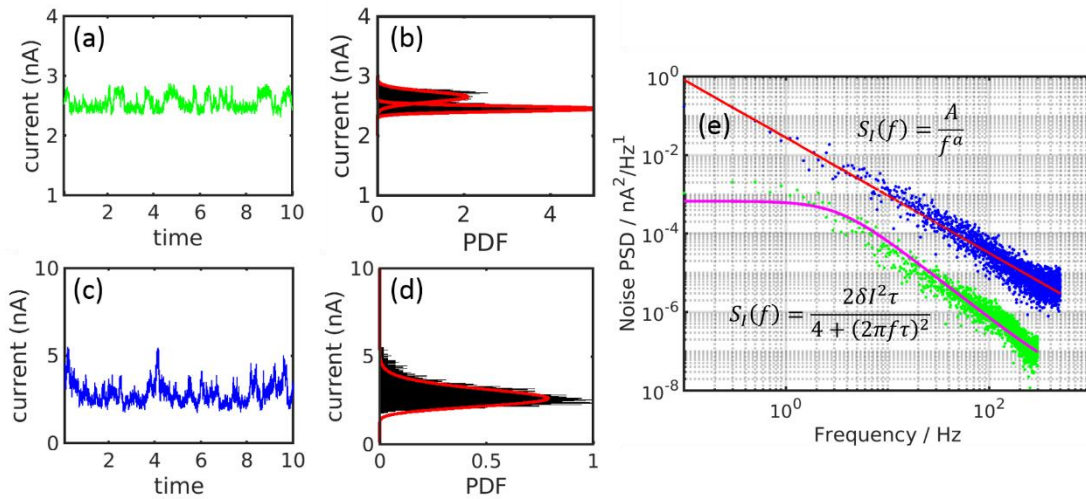


Fig. 6.12 Features of current and noise power spectral density (PSD) corresponding to Model II a, b. (a), (b) Current for Model II (a). (c), (d) Current for Model II (b). (e) PSD spectra for the two current traces. The magnitude of the flicker noise slope is 1.3. ε is linear to the sum of x_i , i.e. $\varepsilon = 1.975 + \sum_{n=1}^5 \frac{x_i}{150}$. $C=0.4, 0.8, 1.2, 1.8, 2.5$ (If $c_i=0.4, 1.2, 1.9, 2.5, 3.2$ are chosen, the magnitude of the slope could decrease to 1.2.).

As for the two-level system, current deviations for the graphene nanogaps (1~2 nm) increase exponentially in experiment. In our model, this feature is clearly shown in Fig. 6.13(a). ΔI is the difference of the two mean values of the two steps $\Delta I = I_{up} - I_{down}$. Here, the transmission has the form of $T(E) = T_0 e^{-\beta(E_F)L}$ due to the Fermi level located in the tail of the transmission peak dominated by the lowest eigenvalue. This exponent term in transmission is the origin of the exponential current feature. In addition, this deviation of current ΔI increases linearly against the mean current of the whole current trace with time. It is noticed that the slope of the fitting curve is around 0.1, which is in qualitative agreement with the experimental results. Again, in this simulation, the environmental fluctuators are related to the bias or tunnelling current in graphene nanogaps. Consequently, this

model can also support the conclusion that the noise in graphene nanogaps are not driven by the tunnelling current. In the basis of these qualitative agreements, it is concluded that the ratio between the tunnel barrier u and the deviation of the tunnel barriers between the two-level steps Δu is approximately 0.028 ($\Delta u/u = 0.028$).

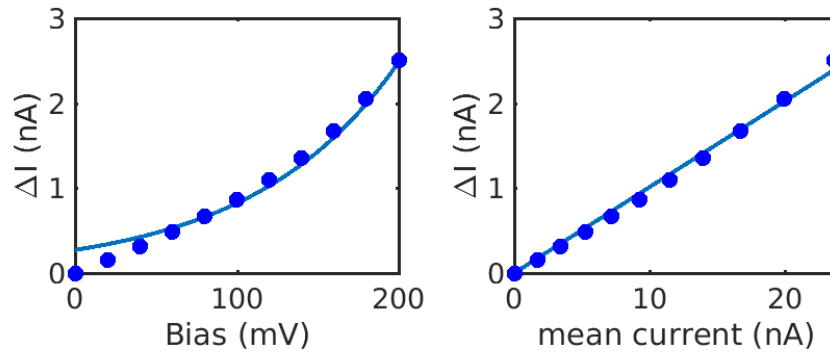


Fig. 6.13 Features of current and noise power spectral density (PSD) corresponding to Model II(a). (a) Exponential increase between the square of current deviations and source-drain bias voltages applied. (b) The linear relationship between current deviations ΔI and mean currents of the two-level current system. Current deviation ΔI means the difference between the mean values of the two levels. The mean currents in (b) mean the mean value for the whole two-level currents. ε is linear to the sum of x_i , i.e. $\varepsilon = 1.975 + \sum_{n=1}^5 \frac{x_i}{150}$.

If the Fermi level is fixed, the oscillations of the tunnel barrier height due to different widths of the graphene nanogap among the samples could happen and this can lead to the transmission variations. Consequently, the current would vary and the slope magnitude a of the flicker noise A/f^a would have fluctuations. The relationship of $\varepsilon_i = \frac{x_i}{15} + 2.35$ is chosen and the corresponding plots are shown in

Fig. 6.14. The two-level current, the Lorentzian noise, exponential and linear

increasing current features, the log-normal distribution currents, the flicker noise power spectral density A/f^a with $a = 1$ are all shown in Fig. 6.14, which are in good agreement with the previous simulation. Finally, we would say the slope a of flicker noise A/f^a varies in the range of 1~1.3 in the simulations, which is also in agreement with the experimental results shown in Fig. 6.3.

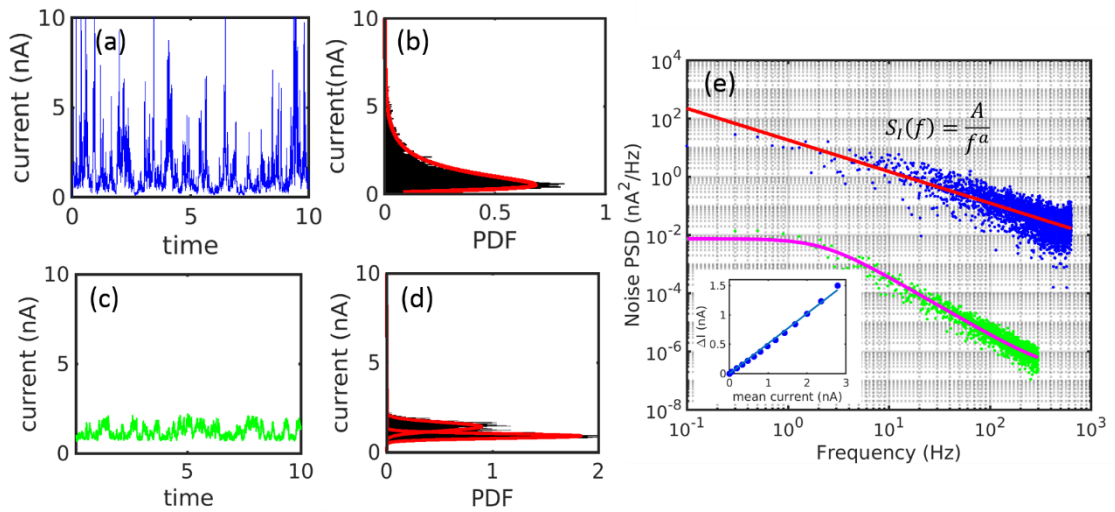


Fig. 6.14 Features of current and noise power spectral density (PSD) corresponding to Model II a, b. (a), (b) Current for Model II (a). (c), (d) Current for Model II (b). (e) PSD spectra for the two current traces. The magnitude of the flicker noise slope a is 1. ε is linear to the sum of x_i , i.e. $\varepsilon = 2.35 + \sum_{n=1}^5 \frac{x_i}{15}$. $c=0.4, 0.8, 1.2, 1.8, 2.5$. The inset shows the linear relationship between deviations of the two-level current and the mean currents of the whole I-t trace under different biases.

6.3 Conclusions

In electroburnt graphene nanogaps, $1/f$ noise and random telegraph noise are observed at room temperature and 77K respectively. The RTN is the first time

observed in graphene nanogaps due to the small exposure surface compared to submicron devices. Larger noise amplitude in graphene nanogaps is attributed to the extreme sensitivity of the tunnel current to environmental fluctuations. In addition, the noise in graphene nanogaps is not driven by the tunnelling current, which is indicated by the linear increasing relationship between current deviation ΔI and mean tunnel current. This feature of the linear $\Delta I \sim I$ is confirmed by our tight binding models, where environmental fluctuators are not affected by the source-drain bias.

I employed simple one-dimensional tight binding models to gauge the effect of two-level fluctuations in the electrostatic environment of the tunnel junction. The tunnel barrier is modelled as a scattering region containing N sites with onsite energy ε_i between two semi-infinite leads. I investigate 4 limiting cases, where: I(a) there is only a single environmental fluctuator coupled to a single level in the tunnel barrier; I(b) there are multiple fluctuators that independently couple to each individual site; II(a) there is only a single fluctuator coupled to all energy levels in the barrier; II(b) there are multiple fluctuators that couple collectively to all energy levels.

The calculated $I-t$ traces for cases I(a) and II(a) show a distinct RTS, in contrast to the $I-t$ traces for case I(b) and II(b), which have the characteristic wandering baseline associated with flicker noise. Moreover, the current histograms for I(b) and II(b) have the same log-normal distribution that was observed in the room temperature experiments. By comparing our simulated and experimental $I-t$ traces, we conclude that our 77 K data is best described by a single fluctuator

influencing the transmission through the tunnel barrier. This may either occur via a local perturbation of the barrier potential, or via an overall modulation of the barrier height. A $1/f$ signal emerges as more fluctuators with the dwell time sampled in a large range are added to the environment, corresponding to the thermal activation of multiple RTSs at room temperature.

Model I and II both work very well compared with the experimental data. Our models can be extended to simulate all the tunnel junction with a molecule bridging the two electrodes or without. It combines the classic environment and the quantum system by the coupling term which could be tuned according to the experimental system of interest.

7 Conclusions

Using DFT and Green's function methods as well as a simple tight binding method (TBM), we can theoretically investigate transport properties of molecular scale junctions and achieve qualitative agreement with experimental data. Consequently, theory and experiment could effectively communicate and help each other to finally explain physics phenomena at the molecular scale.

In Chapter 3, I presented the thermoelectric properties of vertical graphene/C₆₀/graphene architectures. It is found that quantum interference between two C₆₀ placed in parallel enhances the conductance by more than two times in comparison with the monomer C₆₀. Importantly, the Seebeck coefficient also increases which is not expected classically. These results are considered as the starting point to understand the properties of SAMs, when they are sandwiched between two electrodes.

In chapter 4, I showed a new design for single-molecule porphyrin-based switch for graphene nanogaps. Based on the development of feedback controlled electroburning, graphene nanogaps are utilised to propose a conjugation-dependent switch. It is found that the system has an on-off ratio from 100 to 200 when the number of triple-bond spacers between the porphyrin and graphene is increased. Also the switching ratio is further enhanced by decreasing the temperature, reaching approximate 2200 at 100K.

Chapter 5 describes a joint work with experimental collaborators. I proposed a model to understand experimentally observed conductance fluctuations in electro-burnt graphene nanogaps. In the simulation, a simple tight binding model is introduced to prove that the fluctuations are due to the lead states and are not an intrinsic feature of the molecule. The stripes in stability diagrams happen when the molecular level matches with a density of states feature in the leads and the slope could be tuned by the coupling between the lead and a backgate. Next a magnetic field is introduced to distinguish the two kinds of states through ensemble averaging. When a ring is introduced to the tight binding model, the same features are obtained to further confirm the results in experiment. This work showed that the local density of states in graphene is easier to observe, because there are few open channels around Dirac point and the screening effect in graphene is weaker compared to metal electrodes.

Chapter 6 is also a collaborating work with experimental colleagues. In electroburnt graphene nanogaps, $1/f$ noise and random telegraph noise are observed at room temperature and 77K respectively. The RTN is the first time observed in graphene nanogaps due to the small exposure surface compared to submicron devices. Here, I employ a simple one-dimensional tight binding model to gauge the effect of two-level fluctuations in the electrostatic environment in the tunnel junctions. The tunnel barrier is modelled as a scattering region containing N sites with onsite energy ε_i between two semi-infinite leads. We investigate 4 limiting cases, where: I(a) there is only a single environmental fluctuator coupled to a single level in the tunnel barrier; I(b) there are multiple fluctuators that independently couple to each individual site; II(a) there is only a single fluctuator

coupled to all energy levels in the barrier; II(b) there are multiple fluctuators that couple collectively to all energy levels. The calculated $I-t$ traces for cases I(a) and II(a) show a distinct RTS, in contrast to the $I-t$ traces for case I(b) and II(b), which have the characteristic wandering baseline associated with flicker noise. By comparing our simulated and experimental $I-t$ traces, I conclude that our 77 K data is best described by a single dominating fluctuator influencing the transmission through the tunnel barrier. This may either occur via a local perturbation of the barrier potential, or via an overall modulation of the barrier height. A $1/f$ signal emerges as more fluctuators are added to the environment, corresponding to the thermal activation of multiple RTNs at room temperature.

For the future, apart from the investigation of whole thesis, many other aspects in this field deserve further attention, including electron-phonon coupling, spin transport in the presence of ferromagnetic electrodes[143] , phonon transport through parallel arrays of molecules in SAMs, the effect of solvent, robustness of the contact. Furthermore, when thermoelectricity is considered, new strategies are needed to suppress phonon transport, including designs for new combinations of electrodes, molecules and interfaces to improve the figure of merit. At low temperatures, it may also be of interest utilise superconducting electrodes, where Andreev scattering[144] can be utilised to reduce the thermal conductance due to electrons, without reducing the electrical conductance.

8 Appendices

Appendix 1: Dyson equation

When we want to deal with an open and non-periodic system, solving the infinite Schrödinger equation directly is impossible. In order to address this issue, Dyson equation method is introduced. The following is an example to clarify this point.

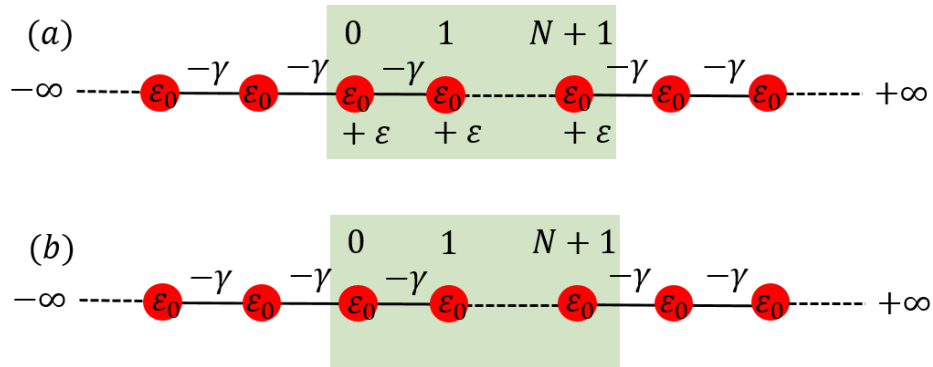


Fig. 8.1 Tight binding model of an open system with a scattering region (the light green shades).

$$H = \begin{pmatrix} \ddots & \ddots & 0 & 0 & 0 \\ \ddots & \epsilon_0 & -\gamma & 0 & 0 \\ 0 & -\gamma & \epsilon_0 & -\gamma & 0 \\ 0 & 0 & -\gamma & \epsilon_0 & \ddots \\ 0 & 0 & 0 & \ddots & \ddots \end{pmatrix} + \begin{pmatrix} 0 & 0 & 0 & 0 & 0 \\ 0 & \epsilon & 0 & 0 & 0 \\ 0 & 0 & \epsilon & 0 & 0 \\ 0 & 0 & 0 & \epsilon & 0 \\ 0 & 0 & 0 & 0 & 0 \end{pmatrix} \quad 8.1$$

Or

$$H = H_0 + H_1 \quad 8.2$$

Where H_0 is Hamiltonian which is an infinite tridiagonal matrix and H_1 is infinite diagonal matrix in which the corresponding on-site energy is ε from 0 to $N+1$ rows. Put in another way, H_1 is the difference between H and H_0 . G is the Green's function of model (a) shown in Fig. 8.1. g is the Green's function of model (b) in Fig. 8.1. Then we have

$$(E - H)G = 1 \Rightarrow (E - H_0)G - H_1G = 1 \Rightarrow g^{-1}G = 1 + \quad 8.3$$

$$H_1G \Rightarrow G = g + gH_1G$$

Or we can expand it as follows

$$G_{ij} = g_{ij} + \sum_{k=-\infty}^{+\infty} \sum_{l=-\infty}^{+\infty} g_{il}(H_1)_{lk}G_{kj} \quad 8.4$$

It is known that $(H_1)_{lk} = \begin{cases} \varepsilon & 0 \leq l = k \leq N + 1 \\ 0 & l \neq k \end{cases}$, and so we have

$$\bar{G} = \bar{g} + \bar{g}\bar{H}_1\bar{G} \Rightarrow \bar{G} = (\bar{g}^{-1} - \bar{H}_1)^{-1} \quad 8.5$$

Here the labels with hat mean the corresponding elements in the range $0 \leq l, k \leq N + 1$ where the connections or disturbances exist.

Appendix 2: Thermoelectric efficiency

The derivation for maximum thermoelectric efficiency.

$$\eta = \frac{-I\Delta V}{STI + \kappa\Delta T} \quad 8.6$$

We have $I = G\Delta V + GS\Delta T$, and substitute I in the expression of η . In order to obtain

the maximum of η , we should set $\frac{d\eta}{d\Delta V} = 0$. Then there is equation as follows,

$$\begin{aligned} GST(\Delta V)^2 + 2GS^2T\Delta V\Delta T + 2\kappa\Delta V\Delta T + GS^3T(\Delta T)^2 \\ + S\kappa(\Delta T)^2 = 0 \end{aligned} \quad 8.7$$

Using Z to replace ZT in the following derivations, then we obtain

$$\Delta V = \frac{S\Delta T}{Z} \left(\sqrt{1+Z} - (1+Z) \right) = S\Delta T a \quad 8.8$$

Where $a = \frac{1}{Z} \left(\sqrt{1+Z} - (1+Z) \right)$. Now substitute equation 8.8 to 8.6,

$$\begin{aligned} \eta &= \frac{-G(\Delta V)^2 - GS\Delta T\Delta V}{STG\Delta V + GS^2T\Delta T + \kappa\Delta T} = -\frac{\Delta T}{T} a \frac{Za + Z}{Za + Z + 1} \\ &= \frac{\Delta T}{T} \cdot \frac{\sqrt{1+ZT} - 1}{\sqrt{1+ZT} + 1} \end{aligned} \quad 8.9$$

Where T is the reference temperature, and here T is equal to the average of the high and low temperature which is consistent with the value in the derivation part (Thermoelectrical expression 2.3.1.2).

Appendix 3: Green's function of a ring

The derivation for the Green's function of a ring is as follows,

The Green's function of a doubly-infinite chain is

$$g_{jl} = \frac{e^{i(\theta+\eta)(j-l)}}{2i\gamma \sin \eta} \quad (j-l) \geq 0 \quad 8.10$$

$$g_{jl} = \frac{e^{i(\theta-\eta)(j-l)}}{2i\gamma \sin \eta} \quad (j-l) \leq 0 \quad 8.11$$

Hence for a ring, we try

$$g_{jl} = \frac{e^{i(\theta+\eta)(j-l)} + a_{jl}}{2i\gamma \sin \eta} \quad (j-l) \geq 0 \quad 8.12$$

$$g_{jl} = \frac{e^{i(\theta-\eta)(j-l)} + a_{jl}}{2i\gamma \sin \eta} \quad (j-l) \leq 0 \quad 8.13$$

Where a_{jl} is a wave function given by $a_{jl} = be^{i(\theta+\eta)(j-l)} + ce^{i(\theta-\eta)(j-l)}$.

Choosing b and c such that $g_{1l} = g_{N+1,l}$ yields the desired result.

Bibliography

- [1] S. V Aradhya and L. Venkataraman, "electronic transport," *Nat. Publ. Gr.*, vol. 8, no. 6, pp. 399–410, 2013.
- [2] G. Schull, "Medicinal Chemistry," *Nature*, vol. 531, p. 587, 2016.
- [3] D. Nozaki and G. Cuniberti, "Silicon-based molecular switch junctions," *Nano Res.*, vol. 2, no. 8, pp. 648–659, 2009.
- [4] L. Berkeley, M. Foundry, E. Division, and E. Division, "Directed Assembly of Single Wall Carbon Nanotube Field Effect Transistors," *ACS Nano*, vol. 10, no. 2, pp. 2975–2981, 2015.
- [5] X. Guo *et al.*, "Covalently Bridging Gaps in Single-Walled Carbon Nanotubes with Conducting Molecules," *Science (80-.)*, vol. 311, no. 5759, pp. 356–359, 2006.
- [6] P. Gehring *et al.*, "Distinguishing Lead and Molecule States in Graphene-Based Single-Electron Transistors," *ACS Nano*, vol. 11, no. 6, pp. 5325–5331, 2017.
- [7] Q. Wu, H. Sadeghi, V. M. García-Suárez, J. Ferrer, and C. J. Lambert, "Thermoelectricity in vertical graphene-C60-graphene architectures," *Sci. Rep.*, vol. 7, p. 11680, 2017.
- [8] H. Sadeghi, S. Sangtarash, and C. J. Lambert, "Robust molecular anchoring to graphene electrodes," *Nano Lett.*, p. acs.nanolett.7b01001, 2017.

- [9] J. C. Cuevas and E. Scheer, "Molecular electronics: an introduction to theory and experiment," *World Sci.*, vol. Vol. 1, 2010.
- [10] S. J. Van Der Molen *et al.*, "Light-controlled conductance switching of ordered metal-molecule-metal devices," *Nano Lett.*, vol. 9, no. 1, pp. 76–80, 2009.
- [11] B. Standley, W. Bao, Z. Hang, J. Bruck, N. L. Chun, and M. Bockrath, "Graphene-Based Atomic-Scale switches," *Nano Lett.*, vol. 8, no. 10, pp. 3345–3349, 2008.
- [12] R. Baer and D. Neuhauser, "Phase coherent electronics: A molecular switch based on quantum interference," *J. Am. Chem. Soc.*, vol. 124, no. 16, pp. 4200–4201, 2002.
- [13] T. Leoni *et al.*, "Controlling the charge state of a single redox molecular switch," *Phys. Rev. Lett.*, vol. 106, no. 21, pp. 4–7, 2011.
- [14] M. del Valle, R. Gutiérrez, C. Tejedor, and G. Cuniberti, "Tuning the conductance of a molecular switch," *Nat. Nanotechnol.*, vol. 2, no. 3, pp. 176–179, 2007.
- [15] P. Moreno-García *et al.*, "Charge transport in C60-based dumbbell-type molecules: Mechanically induced switching between two distinct conductance states," *J. Am. Chem. Soc.*, vol. 137, no. 6, pp. 2318–2327, 2015.
- [16] Q. Wu, S. Hou, H. Sadeghi, and C. Lambert, "A single-molecule porphyrin-based switch for graphene nano-gaps," *Nanoscale*, vol. 10, pp. 6524–6530, 2018.

- [17] X. Zheng, W. Lu, T. A. Abtew, V. Meunier, and J. Bernholc, "Negative Differential Resistance in C60 - Based Electronic Devices," vol. 4, no. 12, pp. 7205–7210, 2010.
- [18] D. Nozaki, A. Santana-bonilla, A. Dianat, R. Gutierrez, and G. Cuniberti, "Switchable Negative Differential Resistance Induced by Quantum Interference Effects in Porphyrin-based Molecular Junctions," *JPCC*, 2015.
- [19] J. Chen, M. A. Reed, A. M. Rawlett, and J. M. Tour, "Large On-Off Ratios and Negative Differential Conductance in a Molecular Electronic Device," *Science (80-.)*, vol. 286, no. November, p. 1550, 1999.
- [20] P. Dollfus, V. H. Nguyen, and J. Saint-Martin, "Thermoelectric effects in graphene nanostructures," *J. Phys. Condens. Matter*, vol. 27, no. 13, p. 133204, 2015.
- [21] M. P. and S. Datta, "Thermoelectric effect in molecular electronics," *PRB*, vol. 26, no. 5, p. 399, 2013.
- [22] M. Famili, I. Grace, H. Sadeghi, and C. J. Lambert, "Suppression of Phonon Transport in Molecular Christmas Trees," *ChemPhysChem*, vol. 18, no. 10, pp. 1234–1241, 2017.
- [23] Q. Wu, H. Sadeghi, and C. Lambert, "MoS2 nano flakes with self-adaptive contacts for efficient thermoelectric energy harvesting," *Nanoscale*, vol. 10, pp. 7575–7580, 2018.

- [24] M. L. Perrin, E. Burzurí, and H. S. J. van der Zant, "Single-molecule transistors," *Chem. Soc. Rev.*, vol. 44, no. 4, pp. 902–919, 2015.
- [25] J. A. Mol *et al.*, "Graphene-porphyrin single-molecule transistors," *Nanoscale*, vol. 7, no. 31, pp. 13181–13185, 2015.
- [26] F. Prins *et al.*, "Room-temperature gating of molecular junctions using few-layer graphene nanogap electrodes," *Nano Lett.*, vol. 11, no. 11, pp. 4607–4611, 2011.
- [27] R. Frisenda *et al.*, "Kondo effect in a neutral and stable all organic radical single molecule break junction," *Nano Lett.*, vol. 15, no. 5, pp. 3109–3114, 2015.
- [28] D. Cakir, D. M. Otalvaro, and G. Brocks, "Magnetoresistance in multilayer fullerene spin valves: A first-principles study," *Phys. Rev. B - Condens. Matter Mater. Phys.*, vol. 90, no. 24, pp. 1–12, 2014.
- [29] J. Schwöbel *et al.*, "Real-space observation of spin-split molecular orbitals of adsorbed single-molecule magnets," *Nat. Commun.*, vol. 3, 2012.
- [30] J. Zhou, K. Wang, B. Xu, and Y. Dubi, "Photoconductance from Exciton Binding in Molecular Junctions," *J. Am. Chem. Soc.*, vol. 140, no. 1, pp. 70–73, 2018.
- [31] S. Battacharyya *et al.*, "Optical modulation of molecular conductance," *Nano Lett.*, vol. 11, no. 7, pp. 2709–2714, 2011.
- [32] B. Mann,; H. Kuhn, "Tunneling through Fatty Acid Salt Monolayer," *Mann, B.; Kuhn, H.*, vol. 42, no. J. Appl. Phys., p. 4398 – 4405, 1971.

- [33] E. E. Polymeropoulos and J. Sagiv, "Electrical conduction through adsorbed monolayers," *J. Chem. Phys.*, vol. 69, no. 5, pp. 1836–1847, 1978.
- [34] L. Netzer and J. Sagiv, "A New Approach to Construction of Artificial Monolayer Assemblies," *J. Am. Chem. Soc.*, vol. 105, no. 3, pp. 674–676, 1983.
- [35] B. Xu and N. J. Tao, "Measurement of single molecule resistance by repeated formation of molecular junctions," *Science (80-.)*, vol. 301, no. August, pp. 1221–1223, 2003.
- [36] D. Xiang, H. Jeong, T. Lee, and D. Mayer, "Mechanically controllable break junctions for molecular electronics," *Adv. Mater.*, vol. 25, no. 35, pp. 4845–4867, 2013.
- [37] H. Park, A. K. L. Lim, A. P. Alivisatos, J. Park, and P. L. McEuen, "Fabrication of metallic electrodes with nanometer separation by electromigration," *Appl. Phys. Lett.*, vol. 75, no. 2, pp. 301–303, 1999.
- [38] C. Z. Li, H. X. He, and N. J. Tao, "Quantized tunneling current in the metallic nanogaps formed by electrodeposition and etching," *Appl. Phys. Lett.*, vol. 77, no. 24, pp. 3995–3997, 2000.
- [39] P. G. Collins, "Engineering Carbon Nanotubes and Nanotube Circuits Using Electrical Breakdown," *Science (80-.)*, vol. 292, no. 5517, pp. 706–709, 2001.
- [40] Y. Cao, S. Dong, S. Liu, Z. Liu, and X. Guo, "Toward functional molecular devices based on graphene-molecule junctions," *Angew. Chemie - Int. Ed.*, vol. 52, no. 14, pp. 3906–3910, 2013.

- [41] J. J. Parks, "Mechanical Control of Spin," *Science (80-.)*, vol. 1370, no. June, pp. 1–5, 2010.
- [42] R. Martin, *Electronic Structure: Basic Theory and Practical Methods*. 2004.
- [43] M. Born and R. Oppenheimer, "Zur Quantentheorie der Molekeln," *Ann. Phys.*, vol. 389, no. 20, pp. 457–484, 1927.
- [44] W. Kohn, "Nobel Lecture: Electronic structure of matter—wave functions and density functionals," *Rev. Mod. Phys.*, vol. 71, no. 5, pp. 1253–1266, 1999.
- [45] D. M. Ceperley and B. J. Alder, "Ground state of the electron gas by a stochastic model," *Phys. Rev. Lett.*, vol. 45, no. 7, pp. 566–569, 1980.
- [46] J. P. Perdew, K. Burke, and M. Ernzerhof, "Generalized gradient approximation made simple," *Phys. Rev. Lett.*, vol. 77, no. 18, pp. 3865–3868, 1996.
- [47] J. Tao, J. P. Perdew, V. N. Staroverov, and G. E. Scuseria, "Climbing the density functional ladder: Nonempirical meta-generalized gradient approximation designed for molecules and solids," *Phys. Rev. Lett.*, vol. 91, no. 14, pp. 3–6, 2003.
- [48] A. Tkatchenko and M. Scheffler, "Accurate molecular van der Waals interactions from ground-state electron density and free-atom reference data," *Phys. Rev. Lett.*, vol. 102, no. 7, pp. 6–9, 2009.
- [49] R. Baer, E. Livshits, and U. Salzner, "Tuned Range-Separated Hybrids in Density Functional Theory," *Annu. Rev. Phys. Chem.*, vol. 61, no. 1, pp. 85–109, 2010.

- [50] C. Toher and S. Sanvito, "Efficient atomic self-interaction correction scheme for nonequilibrium quantum transport," *Phys. Rev. Lett.*, vol. 99, no. 5, pp. 1–4, 2007.
- [51] C. Toher, A. Filippetti, S. Sanvito, and K. Burke, "Self-interaction errors in density-functional calculations of electronic transport," *Phys. Rev. Lett.*, vol. 95, no. 14, pp. 1–4, 2005.
- [52] V. M. García-Suárez and C. J. Lambert, "First-principles scheme for spectral adjustment in nanoscale transport," *New J. Phys.*, vol. 13, 2011.
- [53] and T. W. Wenjing Hong, David Zsolt Manrique, Pavel Moreno-García, Murat Gulcur, Artem Mishchenko, Colin J. Lambert, Martin R. Bryce, M. R. Bryce, and T. Wandlowski, "Single molecular conductance of tolanes: Experimental and theoretical study on the junction evolution dependent on the anchoring group," *J. Am. Chem. Soc.*, vol. 134, no. 4, pp. 2292–2304, 2012.
- [54] D. Z. Manrique *et al.*, "A quantum circuit rule for interference effects in single-molecule electrical junctions," *Nat. Commun.*, vol. 6, no. July, p. 6389, 2015.
- [55] C. J. Lambert, "Basic concepts of quantum interference and electron transport in single-molecule electronics," *Chem. Soc. Rev.*, vol. 44, no. 4, pp. 875–888, 2015.
- [56] M. Buttiker, "Conductance Formula," vol. 31, no. 10, pp. 6207–6215, 1985.

- [57] M. Galperin, A. Nitzan, and M. A. Ratner, "Heat conduction in molecular transport junctions," *Phys. Rev. B - Condens. Matter Mater. Phys.*, vol. 75, no. 15, pp. 1–14, 2007.
- [58] C. J. Lambert, H. Sadeghi, and Q. H. Al-Galiby, "Quantum-interference-enhanced thermoelectricity in single molecules and molecular film," *Comptes Rendus Phys.*, vol. 17, no. 10, pp. 1084–1095, 2016.
- [59] A. R. Garrigues *et al.*, "A Single-Level Tunnel Model to Account for Electrical Transport through Single Molecule-and Self-Assembled Monolayer-based Junctions," *Sci. Rep.*, vol. 6, no. February, pp. 1–15, 2016.
- [60] A. A. Balandin, "Low-frequency 1/f noise in graphene devices," *Nat. Nanotechnol.*, vol. 8, no. 8, pp. 549–555, 2013.
- [61] M. J. Kirton and M. J. Uren, "Noise in solid-state microstructures: A new perspective on individual defects, interface states and low-frequency (1/f) noise," *Adv. Phys.*, vol. 38, no. 4, pp. 367–468, 1989.
- [62] T. A. Of and I. N. Conductors, "Electricity j.," vol. 541, no. 1918, 1927.
- [63] H. Nyquist, "Thermal agitation of electric charge in conductors," *Phys. Rev.*, vol. 32, no. 1, pp. 110–113, 1928.
- [64] R. Ochs, D. Secker, M. Elbing, M. Mayor, and H. B. Weber, "Fast temporal fluctuations in single-molecule junctions," *Faraday Discuss.*, vol. 131, pp. 281–289, 2006.

- [65] T. Lee, Y. Kim, H. Song, D. Kim, and H. Jeong, "Noise Characteristics of Charge Tunneling via Localized States in Metal-Molecule-Metal Junctions," *ACS Nano*, vol. 4, no. 8, pp. 4426–4430, 2010.
- [66] D. Djukic and J. M. Van Ruitenbeek, "Shot noise measurements on a single molecule," *Nano Lett.*, vol. 6, no. 4, pp. 789–793, 2006.
- [67] D. Xiang, X. Wang, C. Jia, T. Lee, and X. Guo, "Molecular-Scale Electronics: From Concept to Function," *Chem. Rev.*, p. acs.chemrev.5b00680, 2016.
- [68] B. W. Heinrich, M. V. Rastei, D. J. Choi, T. Frederiksen, and L. Limot, "Engineering negative differential conductance with the Cu(111) surface state," *Phys. Rev. Lett.*, vol. 107, no. 24, pp. 1–5, 2011.
- [69] V. M. García-Suárez and C. J. Lambert, "Non-trivial length dependence of the conductance and negative differential resistance in atomic molecular wires," *Nanotechnology*, vol. 19, no. 45, p. 455203, 2008.
- [70] J. Taylor, H. Guo, and J. Wang, "Ab initio modeling of open systems: Charge transfer, electron conduction, and molecular switching of a C60 device," *Phys. Rev. B*, vol. 63, no. 12, p. 121104, 2001.
- [71] E. G. Emberly and G. Kirczenow, "The smallest molecular switch," *Phys. Rev. Lett.*, vol. 91, no. 18, p. 188301, 2003.
- [72] M. Paulsson and S. Datta, "Thermoelectric effect in molecular electronics," *Phys. Rev. B*, vol. 67, no. 24, p. 4, 2003.

- [73] S. V Aradhya and L. Venkataraman, "Single-molecule junctions beyond electronic transport," *Nat. Nanotechnol.*, vol. 8, no. 6, p. 399, 2013.
- [74] L. Rincón-García *et al.*, "Molecular design and control of fullerene-based bi-thermoelectric materials," *Nat. Mater.*, vol. 15, pp. 289–293, 2015.
- [75] C. Evangeli, K. Gillemot, E. Leary, M. T. Gonza, G. Rubio-bollinger, and C. J. Lambert, "Engineering the Thermopower of C60 Molecular Junctions," vol. 13, pp. 2141–2145, 2013.
- [76] J. C. Klöckner, R. Siebler, J. C. Cuevas, and F. Pauly, "Thermal conductance and thermoelectric figure of merit of C60-based single-molecule junctions: electrons, phonons, and photons," vol. 245404, pp. 1–11, 2017.
- [77] H. Karamitaheri, M. Pourfath, R. Faez, and H. Kosina, "Geometrical effects on the thermoelectric properties of ballistic graphene antidot lattices," *J. Appl. Phys.*, vol. 110, no. 5, 2011.
- [78] H. Sadeghi, S. Sangtarash, and C. J. Lambert, "Oligoyne Molecular Junctions for Efficient Room Temperature Thermoelectric Power Generation," *Nano Lett.*, vol. 15, no. 11, pp. 7467–7472, 2015.
- [79] V. M. Garcia-Suarez, R. Ferrads, and J. Ferrer, "Impact of Fano and Breit-Wigner resonances in the thermoelectric properties of nanoscale junctions," *Phys. Rev. B - Condens. Matter Mater. Phys.*, vol. 88, no. 23, p. 235417, 2013.

- [80] M. Famili, I. M. Grace, Q. Al-Galiby, H. Sadeghi, and C. J. Lambert, "Toward High Thermoelectric Performance of Thiophene and Ethylenedioxythiophene (EDOT) Molecular Wires," *Adv. Funct. Mater.*, vol. 28, p. 1703135, 2017.
- [81] Y. Kim, W. Jeong, K. Kim, W. Lee, and P. Reddy, "Electrostatic control of thermoelectricity in molecular junctions," *Nat. Nanotechnol.*, vol. 9, no. 11, pp. 881–5, 2014.
- [82] M. G. Reuter, M. C. Hersam, T. Seideman, and M. A. Ratner, "Signatures of Cooperative Effects and Transport Mechanisms in Conductance Histograms," *Nano Lett.*, vol. 12, no. 5, pp. 2243–2248, 2012.
- [83] J. M. Soler *et al.*, "SIESTA Method For Ab Initio Order-N Materials Simulation, The," *J. Phys. Condens. Matter*, vol. 14, no. 11, pp. 2745–2779, 2002.
- [84] I. G. J Ferrer, C J Lambert, V M García-Suárez, D Zs Manrique, D Visontai, L Oroszlany, R Rodríguez-Ferradás and H. S. and L. A. A. S W D Bailey, K Gillemot, "GOLLUM: A next-generation simulation tool for electron, thermal and spin transport," *New J. Phys.*, vol. 16, no. 93029, 2014.
- [85] V. M. Garcia-Suarez, R. Ferradas, D. Carrascal, and J. Ferrer, "Universality in the low-voltage transport response of molecular wires physisorbed onto graphene electrodes," *Phys. Rev. B - Condens. Matter Mater. Phys.*, vol. 87, no. 23, p. 235425, 2013.
- [86] W. W. Pai *et al.*, "Optimal electron doping of a C60 monolayer on Cu(111) via interface reconstruction," *Phys. Rev. Lett.*, vol. 104, no. 3, p. 36103, 2010.

- [87] G. Schull, T. Frederiksen, M. Brandbyge, and R. Berndt, "Passing current through touching molecules," *Phys. Rev. Lett.*, vol. 103, no. 20, pp. 11–14, 2009.
- [88] K. Aihara, M. Yamamoto, K. Iwadate, and T. Mizutani, "Temperature dependence of the phase coherence length of high-mobility algaas/gaas quantum-wire rings," *Jpn. J. Appl. Phys.*, vol. 30, no. 9, pp. L1627–L2730, 1991.
- [89] M. Lv *et al.*, "Long phase coherence length and anisotropic magnetoresistance in MgZnO thin film," *J. Appl. Phys.*, vol. 117, no. 15, 2015.
- [90] C. Huang *et al.*, "Controlling Electrical Conductance through a Pi-Conjugated Cruciform Molecule by Selective Anchoring to Gold Electrodes," *Angew. Chemie - Int. Ed.*, vol. 54, no. 48, pp. 14304–14307, 2015.
- [91] P. Moreno-García *et al.*, "Single-molecule conductance of functionalized oligoynes: Length dependence and junction evolution," *J. Am. Chem. Soc.*, vol. 135, no. 33, pp. 12228–12240, 2013.
- [92] K. Kim *et al.*, "Structural and Electrical Investigation of C 60 -Graphene Vertical Heterostructures," *ACS Nano*, p. 150608110504003, 2015.
- [93] H. Vazquez *et al.*, "Probing the conductance superposition law in single-molecule circuits with parallel paths," *Nat. Nanotechnol.*, vol. 7, no. 10, pp. 663–667, 2012.
- [94] A. Xiang *et al.*, "Electronic transport in benzodifuran single-molecule transistors," *Nanoscale*, vol. 7, no. March 2016, p. , 2015.

- [95] B. Radisavljevic, A. Radenovic, J. Brivio, V. Giacometti, and A. Kis, "Single-layer MoS₂ transistors," *Nat. Nanotechnol.*, vol. 6, no. 3, pp. 147–150, 2011.
- [96] K. Ullmann *et al.*, "Single-molecule junctions with epitaxial graphene nanoelectrodes," *Nano Lett.*, vol. 15, no. 5, pp. 3512–3518, 2015.
- [97] S. J. Heerema and C. Dekker, "Graphene nanodevices for DNA sequencing," *Nat. Nanotechnol.*, vol. 11, no. 2, pp. 127–136, 2016.
- [98] X.-F. Li, K.-Q. Chen, L. Wang, and Y. Luo, "Effects of Interface Roughness on Electronic Transport Properties of Nanotube–Molecule–Nanotube Junctions," *J. Phys. Chem. C*, vol. 114, no. 28, pp. 12335–12340, 2010.
- [99] A. Aviram and M. A. Ratner, "Molecular rectifiers," *Chem. Phys. Lett.*, vol. 29, no. 2, pp. 277–283, Nov. 1974.
- [100] L. Venkataraman, J. E. Klare, C. Nuckolls, M. S. Hybertsen, and M. L. Steigerwald, "Dependence of single-molecule junction conductance on molecular conformation," *Nature*, vol. 442, no. 7105, pp. 904–907, 2006.
- [101] E. H. Van Dijk, D. J. T. Myles, M. H. Van Der Veen, and J. C. Hummelen, "Synthesis and properties of an anthraquinone-based redox switch for molecular electronics," *Org. Lett.*, vol. 8, no. 11, pp. 2333–2336, 2006.
- [102] A. J. Kronemeijer *et al.*, "Reversible conductance switching in molecular devices," *Adv. Mater.*, vol. 20, no. 8, pp. 1467–1473, 2008.

- [103] R. Klajn, J. F. Stoddart, and B. A. Grzybowski, "Nanoparticles functionalised with reversible molecular and supramolecular switches," *Chem. Soc. Rev.*, vol. 39, no. 6, p. 2203, 2010.
- [104] N. Zhang, W.-Y. Lo, A. Jose, Z. Cai, L. Li, and L. Yu, "A Single-Molecular AND Gate Operated with Two Orthogonal Switching Mechanisms," *Adv. Mater.*, vol. 1701248, p. 1701248, 2017.
- [105] S. Seo, M. Min, S. M. Lee, and H. Lee, "Photo-switchable molecular monolayer anchored between highly transparent and flexible graphene electrodes," *Nat. Commun.*, vol. 4, p. 1920, 2013.
- [106] N. Xin *et al.*, "Stereo-electronic Effect-Induced Conductance Switching in Aromatic Chain Single-Molecule Junctions," *Nano Lett.*, vol. 17, no. 2, pp. 856–861, 2017.
- [107] H. Sadeghi, S. Sangtarash, and C. Lambert, "Robust Molecular Anchoring to Graphene Electrodes," *Nano Lett.*, vol. 17, no. 8, pp. 4611–4618, 2017.
- [108] H. Sadeghi, J. Mol, C. Lau, A. Briggs, J. Warner, and C. J. Lambert, "Conductance enlargement in pico-scale electro-burnt graphene nanojunctions," vol. 112, no. 9, pp. 2658–2663, 2015.
- [109] Y. Cao *et al.*, "Building high-throughput molecular junctions using indented graphene point contacts," *Angew. Chemie - Int. Ed.*, vol. 51, no. 49, pp. 12228–12232, 2012.

- [110] C. Nef *et al.*, “High-yield fabrication of nm-size gaps in monolayer CVD graphene,” *Nanoscale*, vol. 6, no. 13, pp. 7249–7254, 2014.
- [111] Z. Wu, Q. Zheng, X. Shi, X. Lan, J. Hao, H. Zeng, “Electron transport enhanced by electrode surface reconstruction: a case study of C₆₀-based molecular junctions,” *RSC Adv.*, vol. 4, no. 84, pp. 44718–44725, 2014.
- [112] J. A. Mol *et al.*, “Graphene-porphyrin single-molecule transistors,” *Nanoscale*, vol. 7, no. 31, pp. 13181–13185, 2015.
- [113] J. P. Perdew, K. Burke, and M. Ernzerhof, “Generalized Gradient Approximation Made Simple- ERRATA,” *Phys. Rev. Lett.*, vol. 77, no. 18, pp. 3865–3868, 1996.
- [114] H. Sadeghi, S. Sangtarash, Q. Al-Galiby, R. Sparks, S. Bailey, and C. J. Lambert, “Negative differential electrical resistance of a rotational organic nanomotor,” *Beilstein J. Nanotechnol.*, vol. 6, no. 1, pp. 2332–2337, 2015.
- [115] J. S. Seldenthuis, F. Prins, J. M. Thijssen, and H. S. J. Van Der Zant, “An all-electric single-molecule motor,” *ACS Nano*, vol. 4, no. 11, pp. 6681–6686, 2010.
- [116] C. M. Finch, S. Sirichantaropass, S. W. Bailey, I. M. Grace, V. M. García-Suárez, and C. J. Lambert, “Conformation dependence of molecular conductance: Chemistry versus geometry,” *J. Phys. Condens. Matter*, vol. 20, no. 2, p. 22203, 2008.

- [117] M. Bürkle *et al.*, “Conduction mechanisms in biphenyl dithiol single-molecule junctions,” *Phys. Rev. B - Condens. Matter Mater. Phys.*, vol. 85, no. 7, p. 75417, 2012.
- [118] A. Al-Backri, V. Zolyomi, and C. J. Lambert, “Electronic properties of linear carbon chains: Resolving the controversy,” *J. Chem. Phys.*, vol. 140, no. 10, 2014.
- [119] S. Lumetti *et al.*, “Single-molecule devices with graphene electrodes,” *Dalt. Trans.*, vol. 45, no. 42, pp. 16570–16574, 2016.
- [120] C. S. Lau, J. A. Mol, J. H. Warner, and G. A. D. Briggs, “Nanoscale control of graphene electrodes,” *Phys. Chem. Chem. Phys.*, vol. 16, no. 38, pp. 20398–20401, 2014.
- [121] S. Bailey, D. Visontai, C. J. Lambert, M. R. Bryce, H. Frampton, and D. Chappell, “A study of planar anchor groups for graphene-based single-molecule electronics,” *J. Chem. Phys.*, vol. 140, no. 5, p. 54708, 2014.
- [122] D. Gunlycke and C. T. White, “Graphene interferometer,” *Appl. Phys. Lett.*, vol. 93, no. 12, p. 122106, 2008.
- [123] M. Oksanen *et al.*, “Single-mode and multimode Fabry-Pérot interference in suspended graphene,” *Phys. Rev. B - Condens. Matter Mater. Phys.*, vol. 89, no. 12, p. 121414, 2014.
- [124] H. Sadeghi, J. a Mol, C. S. Lau, G. A. D. Briggs, J. Warner, and C. J. Lambert, “Conductance enlargement in picoscale electroburnt graphene nanojunctions,” *Proc. Natl. Acad. Sci. U. S. A.*, vol. 112, no. 9, pp. 2658–63, 2015.

- [125] P. Gehring *et al.*, “Quantum Interference in Graphene Nanoconstrictions,” *Nano Lett.*, vol. 16, no. 7, pp. 4210–4216, 2016.
- [126] C. C. Escott, F. A. Zwanenburg, and A. Morello, “Resonant tunnelling features in quantum dots,” *Nanotechnology*, vol. 21, p. 270418, 2010.
- [127] M. L. Perrin, E. Burzurí, and H. S. J. van der Zant, “Single-molecule transistors,” *Chem. Soc. Rev.*, vol. 44, no. 4, pp. 902–919, 2015.
- [128] R. Hanson, L. P. Kouwenhoven, J. R. Petta, S. Tarucha, and L. M. K. Vandersypen, “Spins in few-electron quantum dots,” *Rev. Mod. Phys.*, vol. 79, no. 4, pp. 1217–1265, 2007.
- [129] H. T. Man and A. F. Morpurgo, “Sample-specific and ensemble-averaged magnetoconductance of individual single-wall carbon nanotubes,” *Phys. Rev. Lett.*, vol. 95, no. 2, pp. 6–9, 2005.
- [130] I. A. Verzhbitskiy *et al.*, “Raman Fingerprints of Atomically Precise Graphene Nanoribbons,” *Nano Lett.*, vol. 16, no. 6, pp. 3442–3447, 2016.
- [131] G. Xu, Y. Zhang, X. Duan, A. A. Balandin, and K. L. Wang, “Variability effects in graphene: Challenges and opportunities for device engineering and applications,” *Proc. IEEE*, vol. 101, no. 7, pp. 1670–1688, 2013.
- [132] J. Guan *et al.*, “Direct single-molecule dynamic detection of chemical reactions,” *Sci. Adv.*, vol. 4, no. 2, p. 2177, 2018.
- [133] S. S. Yeh, W. Y. Chang, and J. J. Lin, “Probing nanocrystalline grain dynamics in nanodevices,” *Sci. Adv.*, vol. 3, no. e1700135, 2017.

- [134] S. Rumyantsev, G. Liu, M. S. Shur, R. A. Potyrailo, and A. A. Balandin, "Selective gas sensing with a single pristine graphene transistor," *Nano Lett.*, vol. 12, no. 5, pp. 2294–2298, 2012.
- [135] K. S. Novoselov *et al.*, "A roadmap for graphene," *Nature*, vol. 490, no. 7419, pp. 192–200, 2013.
- [136] G. Xu *et al.*, "Enhanced conductance fluctuation by quantum confinement effect in graphene nanoribbons," *Nano Lett.*, vol. 10, no. 11, pp. 4590–4594, 2010.
- [137] B. N. Costanzi and E. D. Dahlberg, "Emergent $1/f$ Noise in Ensembles of Random Telegraph Noise Oscillators," *Phys. Rev. Lett.*, vol. 119, no. 9, p. 97201, 2017.
- [138] K. S. Ralls *et al.*, "Discrete resistance switching in submicrometer silicon inversion layers: Individual interface traps and low-frequency ($1/f$) noise," *Phys. Rev. Lett.*, vol. 52, no. 3, pp. 228–231, 1984.
- [139] C. Rogers, R. Buhrman, W. Gallagher, S. Raider, A. Kleinsasser, and R. Sandstrom, "Electron trap states and low frequency noise in tunnel junctions," *IEEE Trans. Magn.*, vol. 23, no. 2, pp. 1658–1661, 1987.
- [140] C. Wen *et al.*, "Generalized Noise Study of Solid-State Nanopores at Low Frequencies," *ACS Sensors*, vol. 2, no. 2, pp. 300–307, 2017.
- [141] G. Liu, S. Rumyantsev, M. Shur, and A. A. Balandin, "Graphene thickness-graded transistors with reduced electronic noise," *Appl. Phys. Lett.*, vol. 100, no. 3, 2012.

- [142] S. J. Heerema, G. F. Schneider, M. Rozemuller, L. Vicarelli, H. W. Zandbergen, and C. Dekker, "1/F Noise in Graphene Nanopores," *Nanotechnology*, vol. 26, p. 74001, 2015.
- [143] X. Zhang *et al.*, "Spin conserved electron transport behaviors in fullerenes (C60 and C70) spin valves," *Carbon N. Y.*, vol. 106, pp. 202–207, 2016.
- [144] V. I. Fal'ko, C. J. Lambert, and A. F. Volkov, "Andreev reflections and magnetoresistance in ferromagnet-superconductor mesoscopic structures," *JETP Lett.*, vol. 69, no. 7, pp. 532–538, 1999.